ESTIMATION OF SPEED-SENSITIVE THERMAL MODEL FOR DC MACHINES USING TRANSFER FUNCTION



MASTER OF SCIENCE

UNIVERSITI MALAYSIA PAHANG AL-SULTAN ABDULLAH

UNIVERSITI MALAYSIA PAHANG AL-SULTAN ABDULLAH

DECLARATION OF THESIS AND COPYRIGHT Author's Full Name MUHAMMAD SYAWAL BIN MAT JAHAK Date of Birth 14 FEBRUARY 1996 Title ESTIMATION OF SPEED-SENSITIVE THERMAL MODEL FOR DC MACHINES USING TRANSFER **FUNCTION Academic Session** SEMESTER I 2024/2025 I declare that this thesis is classified as: CONFIDENTIAL (Contains confidential information under the Official Secret Act 1997)* RESTRICTED (Contains restricted information as specified by the organization where research was done)* I agree that my thesis to be published as online open access **OPEN ACCESS** X(Full Text) I acknowledge that Universiti Malaysia Pahang Al-Sultan Abdullah reserves the following rights: 1. The Thesis is the Property of Universiti Malaysia Pahang Al-Sultan Abdullah The Library of Universiti Malaysia Pahang Al-Sultan Abdullah has the right to 2. make copies of the thesis for the purpose of research only. The Library has the right to make copies of the thesis for academic exchange. 3. Certified by: (Student's Signature) (Supervisor's Signature) DR. MOHD AZRI HIZAMI BIN RASID New IC/Passport Number Name of Supervisor Date: 5 February 2025 Date: 5 February 2025

NOTE: * If the thesis is CONFIDENTIAL or RESTRICTED, please attach a thesis declaration letter.



SUPERVISOR'S DECLARATION

I hereby declare that I have checked this thesis and in my opinion, this thesis is adequate in terms of scope and quality for the award of the degree of Master of Science.

(Supervisor's Signature)

Full Name : DR. MOHD AZRI HIZAMI BIN RASID

Position : SENIOR LECTURER

Date : 5 FEBRUARY 2025

UMPSA

(Co-supervisor's Signature)

MALAYSIA PAHANG

Full Name : AL-S

Position :

Date :



STUDENT'S DECLARATION

I hereby declare that the work in this thesis is based on my original work except for quotations and citations which have been duly acknowledged. I also declare that it has not been previously or concurrently submitted for any other degree at Universiti Malaysia Pahang Al-Sultan Abdullah or any other institutions.

(Student's Signature)

Full Name : MUHAMMAD SYAWAL BIN MAT JAHAK

ID Number : MJM22003

Date : 5 FEBRUARY 2025

اونيؤرسيتي مليسيا فهغ السلطان عبدالله UNIVERSITI MALAYSIA PAHANG AL-SULTAN ABDULLAH

ESTIMATION OF SPEED-SENSITIVE THERMAL MODEL FOR DC MACHINES USING TRANSFER FUNCTION

MUHAMMAD SYAWAL BIN MAT JAHAK

UMPSA

Thesis submitted in fulfillment of the requirements

اوئیو for the award of the degree of UNIVERSITI Master of Science PAHANG AL-SULTAN ABDULLAH

Faculty of Manufacturing and Mechatronic Engineering Technology

UNIVERSITI MALAYSIA PAHANG AL-SULTAN ABDULLAH

FEBRUARY 2025

ACKNOWLEDGEMENTS

I wish to extend my profound gratitude to all who have facilitated the completion of this thesis. My advisor, Dr. Mohd Azri Hizami Rasid, deserves special recognition for his unwavering support throughout my M.Sc. studies and related research. His patience, motivation, and extensive knowledge have been invaluable. His guidance has been instrumental throughout this thesis's research and writing phases. Our informal discussions have been particularly enlightening, during which he demonstrated how to excel as an educator, how to provide students with opportunities for learning and intellectual growth, and how to approach academic and scientific work from a broader perspective. I could not have envisioned a more suitable advisor and mentor for my M.Sc. studies.

I would like to extend my heartfelt gratitude to the Faculty of Manufacturing and Mechatronic Engineering Technology for providing me with unrestricted access to the laboratory and research facilities. I would also like to express my special thanks to the laboratory technician, Suhaimi Puteh. Without their invaluable support, conducting this research would not have been possible.

Finally, the most important people to whom my backbone throughout the journey of this study, my precious parents who unwavering prayed and supported me both mentally and physically, siblings and friends.

UMPSA

اونيورسيتي مليسيا فهغ السلطان عبدالله UNIVERSITI MALAYSIA PAHANG AL-SULTAN ABDULLAH

ABSTRAK

Motor menyumbang kepada 40% daripada penggunaan elektrik global dan 13% daripada pelepasan karbon, serta sering mengalami kerosakan haba yang tidak dapat dipulihkan. Untuk mengelakkan sisa buangan elektrik yang berlebihan dan meningkatkan jangka hayat, adalah penting untuk memantau suhu motor dengan tepat dan menghentikan operasi pada tahap selamat. Kajian ini bertujuan untuk membangunkan model masasebenar untuk memantau suhu dalam motor arus terus MY1016, menggunakan transfer function. Antara objektif kajian ini adalah mengenal pasti transfer function yang paling tepat, membangunkan, dan mengesahkan model transfer function dengan pole dipuratakan dan pole boleh ubah, dan menilai keupayaan model ini untuk mengesan kerosakan. Data eksperimen telah direkodkan pada beberapa komponen seperti berus karbon, galas bebola, magnet, dan bingkai. Motor tersebut telah dioperasi pada kelajuan dari 20% ke 100% halaju nominalnya tanpa beban, sehingga mencapai kestabilan pemindahan haba. Toolbox identifikasi sistem oleh MATLAB telah digunakan untuk mengenal pasti transfer function dengan bilangan pole dari 1 hingga 4 dan tanpa zeroes. Kajian ini mendapati bahawa tindak balas suhu terhadap operasi motor telah menghasilkan suhu tertiggi sewaktu halajunya pada 60% daripada halaju nominal. Berus karbon dapat dimodel dengan baik oleh transfer function tahapan ketiga, manakala transfer function tahapan pertama sudah memadai untuk komponen-komponen lain. Pemerhatian kepada pole transfer function tindak balas suhu motor mendapati bahawa sistem ini bukan sebuah sistem LTI. Oleh itu, sebuah model menyeluruh menggunakan transfer function dengan pole boleh ubah untuk penggunaan pemantaun masa sebenar dibangunkan dan dinilai. Ia mampu menjangka suhu motor pada keadaan kelajuan berubah dan tetap, dengan ralat maksimum setinggi 10 °C. Kesimpulannya, transfer function dengan pole boleh ubah sesuai digunakan untuk pemantauan keadaan motor dengan menggunakan beberapa scenario pemeriksaan dan boleh diapplikasi pada motormotor yang lain pada masa akan datang. اونیورسیتی ملیسیا

UNIVERSITI MALAYSIA PAHANG AL-SULTAN ABDULLAH

ABSTRACT

Motors account for 40% of global electricity consumption and 13% of carbon emissions and often suffer irreversible thermal damage. To prevent excessive electrical waste and improve reliability, it's crucial to monitor motor temperature accurately and halt operation at safe levels. This study aims to develop a real-time model for monitoring motor temperature in MY1016 direct current machines, using a transfer function. The objectives include identifying the most precise transfer function to model the temperature response of each component at different speed, developing, and validating a generalized model using averaged-pole and variable-pole transfer function models, and finally evaluating their feasibility for fault detection. Experimental data was recorded for different motor components including the brush, bearing, permanent magnet and casing. The motor was operated at speeds from 20% to 100% of nominal speed with no load, until thermal equilibrium was reached. The MATLAB system identification toolbox was used to identify the transfer function, with a number of poles varying from 1 to 4 and with no zeros. The study found that the temperature response of the MY1016 motor at 60% of the nominal speed produces the highest temperature. The brush was best represented by a 3rd order transfer function, while a 1st order transfer function is sufficient to represent other components. The non-LTI characteristic of the temperature response observed from the pole analysis led to a choice of modeling using variable-pole transfer function to create the baseline temperature model. It can estimate temperature response during both steady and transient speed states, with a maximum temperature difference of 10 °C. The study concludes that the variable-pole transfer function can be used to monitor electric motors' condition using several testing scenarios. The same method can be suggested to be applied on other types of motors.



TABLE OF CONTENT

DEC	LARAT	TION	
TITL	E PAG	E	
ACK	NOWL	EDGEMENTS	ii
ABS	ΓRAK		iii
ABS	ΓRACT		iv
TAB	LE OF	CONTENT	v
LIST	OF TA	BLES	viii
LIST	OF FIG	GURES	ix
LIST	OF SY	MBOLS	xii
LIST	OF AB	BREVIATIONS	xiv
LIST	OF AP	PENDICES	xvi
ABSTRAK ABSTRACT TABLE OF CONTENT LIST OF TABLES LIST OF FIGURES LIST OF ABBREVIATIONS LIST OF APPENDICES CHAPTER 1 INTRODUCTION 1.1 Background of Study 1.2 Problem Statement ALAYSIA PAHANG 1.3 Objectives AL-SULTAN ABDULLAH 1.4 Scope CHAPTER 2 LITERATURE REVIEW 2.1 Introduction 2.2 Generalities on DC Machines 2.2.1 Utilization and Operating Principle 2.2.2 Losses in Electrical Machine 1.2.3.1 Cause of Degradation and Heat Transfer	1		
1.1	Backg	ground of Study	1
1.2	Proble	اونيۇرسىتى ملىسىيا قهغ السلطانm Statement	3
1.3	Objec	UNIVERSITI MALAYSIA PAHANG tives AL-SULTAN ABDULLAH	4
1.4	Scope		5
СНА	PTER 2	LITERATURE REVIEW	6
2.1	Introd	uction	6
2.2	Gener	alities on DC Machines	6
	2.2.1	Utilization and Operating Principle	8
	2.2.2	Losses in Electrical Machine	12
2.3	Temp	erature Rises in Electrical Machine	16
	2.3.1	Cause of Degradation and Heat Transfer	16
	2.3.2	Monitoring, Modelling Temperature Response and Diagnostic	26

2.4	Transfer Function as Model	35
	2.4.1 Generalities of Frequency Domain Model	37
	2.4.2 System Identification	42
	2.4.3 Evaluation of Model Precision	51
2.5	Highlights on the Research Gap	54
СНА	PTER 3 METHODOLOGY	57
3.1	Introduction	57
3.2	Objective 1 Part (A): Experimental Setup	58
	3.2.1 MY1016 DC Motors Specifications	61
	3.2.2 Motor No-Load Current	62
	3.2.3 Speed Controller	63
	3.2.4 Temperature Measurement	64
	3.2.5 Objective 3 : Fault Experiment	65
3.3	Objective 1 Part (B): Transfer Function Identification	68
	3.3.1 System Identification Toolbox	68
	3.3.2 Error Evaluations AN ABDULLAH	71
3.4	Objective 2 : Development of Generalized Transfer Function Model	72
	3.4.1 Analysis of System Linearity	72
	3.4.2 Averaged-Pole Transfer Function	76
	3.4.3 Variable-Pole Transfer Function	79
СНА	PTER 4 RESULTS AND DISCUSSION	85
4.1	Introduction	85
4.2	General Observation of The Temperature Response	85
4.3	Objective 1 : Transfer Function of Each Component at Different Speed	
	Input	88

4.4	Objective 2 Part (A): Analysis of System Linearity 92		
4.5	Object	tive 2 Part (B): Analysis of Generalized Transfer Function	96
	4.5.1	Averaged-Pole Transfer Function	97
	4.5.2	Variable-pole Transfer Function	104
	4.5.3	Test Validation for Model Robustness at Different Speed Points	111
4.6	Object	tive 3: Usage of Generalized Transfer Function in Fault Detection	113
СНА	PTER 5	CONCLUSION	119
5.1	Introd	uction	119
5.2	Perspe	ectives	121
REFI	ERENC	ES	123
APPI	ENDICI	UMPSA	139
		اونيؤرسيتي مليسيا فهغ السلطان عبدالله	
		AL SIII TAN ARDIII LAH	

LIST OF TABLES

Table 2.1	Summary of current electric machines applications.		
Table 2.2	Summary of losses.		
Table 2.3	Comparison of permanent magnet properties.		
Table 2.4	Summary causes of degradation and heat transfer.		
Table 2.5	Summary of monitoring and modelling temperature response and diagnostic.	34	
Table 2.6	Summary of generalities of the frequency domain model.	42	
Table 2.7	Summary of the model type using system identification.	43	
Table 2.8	Summary of system identification.	50	
Table 2.9	Summary of evaluation of model precision.	53	
Table 2.10	Summary of research gaps of real time fault detection.	55	
Table 3.1	Specification of small brushed DC machines.	61	
Table 4.1	The steady-state temperature °C of all components at different speeds.	86	
Table 4.2	Identified transfer function for brush.	89	
Table 4.3	The identified transfer function at each component and each speed.		
Table 4.4	Pole position, average and variance of each component.		
Table 4.5	Averaged-pole transfer function of each component.		
Table 4.6 Table 4.7	The temperature difference °C of averaged-pole transfer function at steady state of all component at different speed. Steady-state temperature estimation error from Figure 4.5 in		
14010 1.7	percentage.		
Table 4.8	The temperature difference °C of the averaged-pole transfer function at the transient state of all components at different speeds.	102	
Table 4.9	Percentage error between experimental data and averaged-pole transfer function model at transient state for all components from Figure 4.7.		
Table 4.10	Function for variable-pole position for each component.		
Table 4.11	The temperature difference °C of the variable-pole transfer function at steady state for all components at different speeds.		
Table 4.12	Similarity percentage between experimental and variable-pole transfer function model for all components at steady state.		
Table 4.13	The temperature difference °C of variable-pole transfer function at transient state of all component at different speed.		
Table 4.14	Similarity percentage between experimental data and variable-pole transfer function model at transient state for all components.	111	

LIST OF FIGURES

Figure 1.1	Motor failure.	2	
Figure 2.1	Classification of electric machines.	7	
Figure 2.2	BLDC motor installed in a car.	8	
Figure 2.3	Structure and components of brushed DC machines.		
Figure 2.4	Force on a one-turn coil.	11	
Figure 2.5	Losses in DC machines.	12	
Figure 2.6	Graph losses vs speed.	14	
Figure 2.7	Temperature vs. life curves for insulation systems for different class of machines of the same type.	18	
Figure 2.8	Interturn fault occurrence in a single phase.	19	
Figure 2.9	Heat transfer flow diagram of PMSM.	22	
Figure 2.10	Temperature distribution in stator induction motor.	29	
Figure 2.11	Lumped Parameter model of the Syncrel motor.	30	
Figure 2.12	Temperature estimation under 100% load condition.	36	
Figure 2.13	(a) Amplifier saturation. (b) Motor dead zone. (c) Backlash in gears.	38	
Figure 2.14	(a) Block diagram of a first-order system. (b) Simplified block diagram.	39	
Figure 2.15	Exponential response curve.	41	
Figure 3.1	اونیورسیتی ملیسیا فهغ السلطان عبدالله Research flow chart. MALAYSIA PAHANG	57	
Figure 3.2	Flow chart of the experimental data generation.	59	
Figure 3.3	Instrumentation of DC machines.	59	
Figure 3.4	The complete experimental setup.	60	
Figure 3.5	Rated current at no load speed.	62	
Figure 3.6	Motor controller block diagram.	64	
Figure 3.7	Temperature measurement block diagram.	65	
Figure 3.8	MY1016 DC machines with degrease bearing fault.	66	
Figure 3.9	MY1016 DC machines with broken brush fault.	67	
Figure 3.10	Flow chart of the development of transfer function for temperature response of the MY1016 DC machine from the experimental data.	68	
Figure 3.11	Import data step input and temperature response.	69	
Figure 3.12	Result estimation transfer function in system identification.	70	
Figure 3.13	Flow chart of the developemnet of generalized transfer function model.	72	
Figure 3.14	S-plane graph of pole brush.	74	

Figure 3.15	S-plane graph of pole bearing.		
Figure 3.16	Construction of averaged-pole transfer function model.		
Figure 3.17	Averaged-pole transfer function block diagram.		
Figure 3.18	Curve-fitting of the component bearing.		
Figure 3.19	Pole function implemented in Simulink.	82	
Figure 3.20	Variable-pole transfer function block diagram.	83	
Figure 4.1	Temperature response data gathered at 60% of the nominal speed of 2650rpm.		
Figure 4.2	Steady state temperature of the MY1016 component at different speeds.	87	
Figure 4.3	Temperature response of identified transfer function model for 60% of nominal speed for the component brush.	91	
Figure 4.4	Comparison between averaged-pole transfer function vs. experimental temperature response at steady state temperature (brush).	98	
Figure 4.5	Temperature difference between experimental and averaged-pole transfer function model at steady state for all components.	100	
Figure 4.6	Comparison between averaged-pole transfer function vs. experimental temperature response at transient temperature (brush).	101	
Figure 4.7	Temperature difference between experimental data and averaged-pole transfer function model at transient state for all components.	102	
Figure 4.8	Comparison between variable-pole transfer function vs. experimental temperature response at steady state temperature (brush).	105	
Figure 4.9	Temperature different between experimental and variable-pole transfer function model for all components at steady state.	107	
Figure 4.10	Comparison between variable-pole transfer function vs. experimental temperature response at transient temperature (brush).	109	
Figure 4.11	Temperature difference between experimental data and variable- pole transfer function model at transient state for all components.	110	
Figure 4.12	Comparison between equivalent model vs. experimental data at different speed point (brush).	112	
Figure 4.13	Comparison between healthy and faulty DC machines (brush).	114	
Figure 4.14	Comparison between variable-pole transfer function model vs. healthy and faulty DC machines (brush).	115	
Figure 4.15	Temperature differessnce between variable-pole transfer function vs. faulty and healthy DC machines (brush).	116	

Figure 4.16	Comparison between variable-pole transfer function model vs. healthy and faulty DC machines (casing).	117
Figure 4.17	Temperature difference between variable-pole transfer function vs. aulty and healthy DC machines (casing).	



LIST OF SYMBOLS

ΔP_{Fe}	Iron Losses
ΔP_{Cu1}	Losses in Stator Winding
ΔP_{ad}	Additional Losses
P_{e1}	Electrical Power
ΔP_{Cu2}	Losses in Rotor Winding
R_s	Winding Resistance
I_{RMS}^2	Winding RMS Current
\boldsymbol{A}	Current
Ω	Ohm
P_h	Hysteresis Loss
P_e	Eddy Current Loss
P_a	Anomalous Loss
k_h	Coefficient of Hysteresis Loss
k_e	Coefficient of Eddy Current Loss
k_a	Coefficient of Anomalous Loss
f	Frequency
B_m	Magnetic Induction Intensity of Core Material
\dot{Q}_{cond}	Quantity of Heat
∇T	Temperature Gradient ABDULLAH
λ	Material Conductivity
\overrightarrow{dA}	Oriented Surface Area Infinitesimal
R_{th}	Thermal Resistance
R_{cond}	Resistance of Conduction Heat
ΔT	Difference of Temperature
\boldsymbol{A}	Surface Area
$\dot{Q}_{rad}(J)$	Rate of Heat Transferred by Radiation
ε	Emissivity of Surface
F_{1-2}	View Factor of Surface
$^{\circ}\mathcal{C}$	Celsius
N	Nominal Speed

k	Components		
$T_k(t)$	Temperature Response of Component k		
Z_n	Number of Zero		
P_n	Number of Pole		
$T_{kN}(t)$	Temperature Response of Component k at speed N		
$G_{kN}(s)$	Transfer Function for Temperature Response $T_{kN}(t)$		
$G_k(s)$	General Transfer Function for Temperature Response of Component		
	k at all speed		
$\sigma_{k \; N}$	Pole of Transfer Function for Component k at Speed N		
$\sigma_k(N)$	Function of Pole of Component k in Relation to Speed N		
$K_{k N}$	Gain of Transfer Function for Component k at Speed N		
$K_k(N)$	Function of Gain of Component k in Relation to Speed N		
$arepsilon_n$	Estimation Error		
n	Order of System		
$Z_{k N}$	Zero of Transfer Function for Component k at Speed N		
$ar{\sigma}$	Averaged Pole		
\overline{K}	Averaged Gain UMPSA		
b_n	Number of Gain in Varying Transfer Function Block		
a_n	Number of Pole in Varying Transfer Function Block		
	AL-SULTAN ABDULLAH		

LIST OF ABBREVIATIONS

DC Direct Current

AC Alternative Current
AI Artificial Intelligent

LPTN Lumped Parameter Thermal Network

FPE Final Prediction Error

MSE Mean Square Error

PMDC Permanent Magnet Direct Current

EPS Electric Power System

VAC Voltage Alternative Current

BLDC Brushless Direct Current

Hz Hertz

MMF Magneto Motive Force

EMF Electromotive Force

FE Finite Element

IRT Infrared Thermography

FEM Finite Element Model

VASA Vibration and Acoustic Signature Analysis

TSA Thermal Signature Analysis

LTI Linear Time Invariant AYSIA PAHANG

RC Resistor-Capacitor

DAQ Data Acquisition

PC Personal Computer

PPR Pulses Per Revolution

RPM Revolution Per Minutes

PWM Pulses Width Modulation

SSE Sum of Squares Error

MDD Motor Driver Dual

MCSA Motor Current Signature Analysis

FFT Fast Fourier Transform

FDD Fault Detection and Diagnostic

ISF Interturn Short Fault

PMSM Permanent Magnet Synchronous Motor

IPMSM Interior-type Permanent Magnet Synchronous Motor

IEEE Institute of Electrical and Electronic Engineers

AIEE American Institute of Electrical Engineers

NRMSE Normalize Root Mean Square Error

ARX Autoregressive Exogenous

FSPM Flux Switching Permanent Magnet

IM Induction Motor

CNN Convolution Neural Network



LIST OF APPENDICES

Appendix A:	IEC Electric machines Duty Cycle		
Appendix B:	Simulink Block Diagram.		
Appendix C:	System Identification Toolbox.	145	
Appendix D:	System Linearity.	146	
Appendix E:	Calculation for Averaged-pole Transfer Function.	147	
Appendix F:	Calculation for Variable-pole Transfer Function.	151	
Appendix G:	Pole Function Code.	154	
Appendix H:	Temperature Response Data.	156	
Appendix I:	Identified Transfer Function.	157	
Appendix J:	Validation Identified Transfer Function As Model.		
Appendix K:	Result of Steady State Temperature Response for Averaged-pole Transfer Function Model.	164	
Appendix L:	Result of Transient State Temperature Response for Averaged-pole Transfer Function Model.		
Appendix M:	Result of Steady State Temperature Response for Variable-pole Transfer Function.	166	
Appendix N:	Result of Transient State Temperature Response for Variable-pole Transfer Function.	167	
Appendix O:	Result of Generalized Transfer Function in Fault Detections او نيوْرسيتي مليسيا ڤهڠُ السلطان عبدالله UNIVERSITI MALAYSIA PAHANG	168	
	AL-SULTAN ABDULLAH		

CHAPTER 1

INTRODUCTION

1.1 Background of Study

Motors consume approximately 40% of the world's electricity and contribute to around 13% of global carbon emissions(Ferreira & de Almeida, 2008). The electric machines market is expected to grow to USD 169 billion by 2026, at an annual growth rate of 6.9% from an estimated USD 113 billion in 2020(New Market Reports, 2020). The increase in market size for electric machines presents challenges for end-of-life management of electric machines and a requirement for appropriate strategies for high-value materials. A report by the European Commission published in 2020(Critical Raw Materials Resilience: Charting a Path towards Greater Security and Sustainability, 2020) predicted that by the end of 2050, the European Union would require 15 times more cobalt and 10 times more rare earth materials as compared to current consumption.

To avoid the catastrophe of having too much electrical waste, the utilization of these motors needs to be optimized. Avoiding premature damage and prolonging the life cycle of the motors is essential. This can be done by having a full understanding of the root cause of the irreversible damage that brought the motor to the landfill. The leading cause of motor failure is overloading. As shown in Figure 1, overloading counts for 30% of motor failure (Gonzalez-Cordoba et al., 2017).

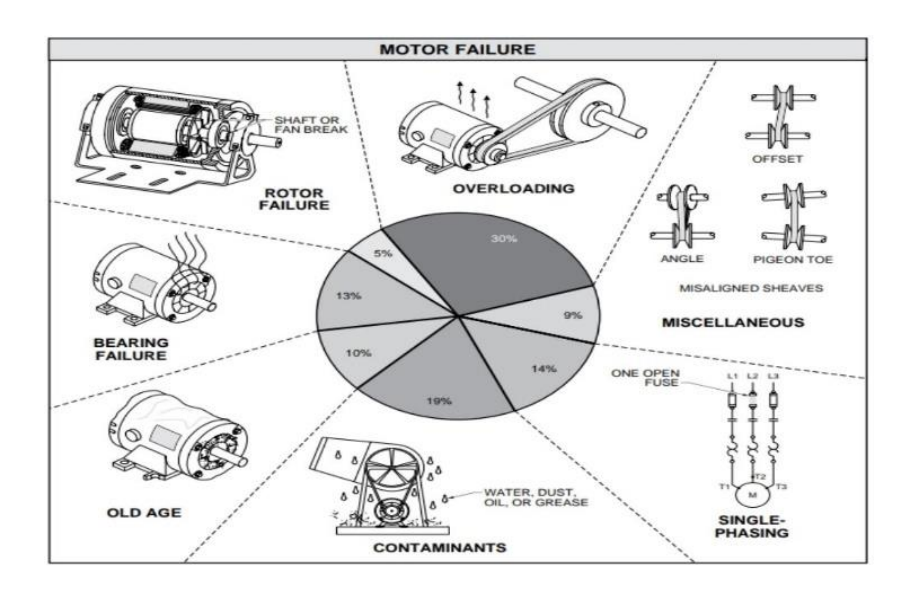


Figure 1.1 Motor failure.

Source: Electric Motor Failure Causes (2017)

Mechanical overload generated by high torque values (X. Liang et al., 2020) is an undesirable and typical operating condition in industrial processes. This condition causes negative consequences such as premature aging of motor bearings, locked rotor, poor lubrication, and windings overheating (Sheikh et al., 2022). Mechanical overload generates an excessive temperature on induction motors since a proportional increment in the demand of the stator current is also generated(X. Liang et al., 2020), which accelerates the degradation of motor components including the stator/rotor conductors, core, insulation, permanent magnet, and bearings (Tallam et al., 2007; P. Zhang et al., 2011). Continuous elevated temperature induces demagnetization of permanent magnet and melting of the insulation which creates winding short circuits. Monitoring the temperature inside the motor and setting a maximum operating temperature are therefore essentials in making sure that the motor is always in a good condition.

1.2 Problem Statement

Due to low cost and ease of production of DC machines (C. Liu, 2018), manufacturer and user tend to not optimize the design of the motor specifically for an application. They regularly discard and change the motor once they are damaged. The most common irreversible damage that can be done to a motor is thermal damage: melting or burning the winding insulation. This leads to short-circuit and demagnetization of permanent magnet (Hattori et al., 2023). The lifespan of a DC machine is known to be ranging from 30,000 to 40,000 hours (Rusu-Zagar et al., 2013). Despite its low cost, increasing its lifespan would mean budget and cost saving in an economy of scale. It is not just for the benefit of the industries for their cost reduction, but also for the reduction of electric machines waste in the landfill. For a large fleet of applications and a larger motor, potential reliability improvement can be obtained by properly monitoring the temperature and stop the operation of the motor at a proper temperature level as a preventive measure to avoid damage. In general, the monitoring system need to be precise, consume little computing power, can be implemented in real time, and if possible short development time to allow it to be replicated onto a fleet of different motor offerings.

To build a proper temperature monitoring system for the components of the motor, the classic solution is to equip the motor with temperature measurement instrumentation. However, this leads to additional costs and cable management issues. It could be too much for a system equipped with many motors (Wu & Dobson, 2012). The less instrumented option is to have a real-time model that estimates the temperature of the components inside the motor using a single input like speed or current of the motor (Sundararajan et al., 2022). There is also another possibility of using a neural network predictive modeling that can warn against potential damage. However, like any other AI approach, a large amount of training and test data is necessary to create the model, which means instrumenting the motors with temperature measurement equipment and running plenty of tests beforehand. All these three methods have their merits of advantages as well as inconveniences that will be discussed in the literature review. In this study, the real-time model is going to be adopted.

To develop the real-time model, there are many options for temperature response modeling. The usual options include the LPTN model (Pescetto et al., 2020) and full analytical model (Pawlus et al., 2017). However, developing and validating them takes a certain development time. In the case where the direct relation between the physical parameters (dimensions and material) of the motor and the temperature is not essential to be known, a transfer function can be used to describe the temperature response. Transfer functions are light to be implemented in real-time and can be quickly developed through transfer function identification using several experimental data only. However, the Linear Time-Invariant (LTI) condition of a transfer function needs to be analyzed so that the model developed is valid for all speeds and load points.

This study will explore the best form of transfer function (order) to describe the temperature response of components in a DC machine, develop a generalized model that is speed-dependent, and evaluate the model precision. Obtaining a high-precision transfer function model of the temperature response will allow a low-cost and efficient temperature monitoring of DC machines in application.

1.3 Objectives

The objectives of this project are as follows:

- 1. To model the most precise transfer function of temperature response in the MY1016 DC machines at different speeds.
- 2. To validate an averaged-pole transfer function model and a variable-pole transfer function model.
- 3. To evaluate the feasibility of real-time fault anomaly detection using the transfer function model.

1.4 Scope

The scope of this study are as follows:

- 1. The motor used to obtain the temperature response data is a 250W brushed DC machine, MY1016.
- 2. The temperature responses were obtained from a step speed input at different speeds, up to the steady state temperature. The experiment is conducted with no load. The definition of steady state temperature being no temperature variation observed after 10 minutes.
- 3. The ambient temperature during the data acquisition is controlled at a room temperature of 30 °C.
- 4. The transfer function describing the temperature response were obtained using the system identification toolbox in MATLAB.
- 5. The measure of the precision of the system identification was done using the indicator of Fit to estimation data (in %), FPE (final prediction error), and MSE (mean-square error).

UMPSA

اونيؤرسيتي مليسيا قهڠ السلطان عبدالله UNIVERSITI MALAYSIA PAHANG AL-SULTAN ABDULLAH

CHAPTER 2

LITERATURE REVIEW

2.1 Introduction

The literature review chapter is divided into three subsections. The first subsection discusses generalities on DC machines, including their utilization and operating principles. It also covers common losses that occur in DC machines. The second subsection focuses on temperature rises in electrical motors, explaining the causes of degradation and irreversible damage that can occur in electrical machines due to temperature, also heat transfer in electrical machines. Additionally, it covers the monitoring and modeling of temperature response, as well as diagnostic methods commonly used in electrical machines. The final subsection discusses transfer functions as a model in modeling the temperature response of DC machines, including generalities of transfer functions, the system identification MATLAB toolbox, and the evaluation of model precision for transfer functions. Finally, following the literature reviews, the research gap where a baseline temperature model of a motor using transfer function for condition monitoring will be highlighted.

2.2 Generalities on DC Machines

Nearly every mechanical movement is driven by an electric machine. These machines primarily serve as energy converters, transforming electrical energy into mechanical energy, with heat being a by-product of this process. Motors come in diverse sizes; large motors capable of managing thousands of horsepower are extensively used in industries for applications such as elevators, electric trains, hoists, and metal rolling mills. Conversely, small motors are utilized in automobiles, robots, handheld power tools, and household appliances.

AL-SULTAN ABDULLAH

Electric machines can be broadly classified into two categories: AC and DC machines. Each category encompasses machines with distinct characteristics and capabilities, making them suitable for specific applications. An electric machine consists of a stator the stationary part and a rotor the rotating part. The interaction between the stator and the rotor's magnetic fields generates rotational speed and torque. DC machines are particularly noted for their operation on direct current.

The force within an electric machine is generated by the interaction between winding currents and the machine's magnetic field. Both AC and DC sources can power these machines. The output power of an electric machine can vary from a few watts to several hundred kilowatts. Figure 2.1 depicts an electric machine categorization.

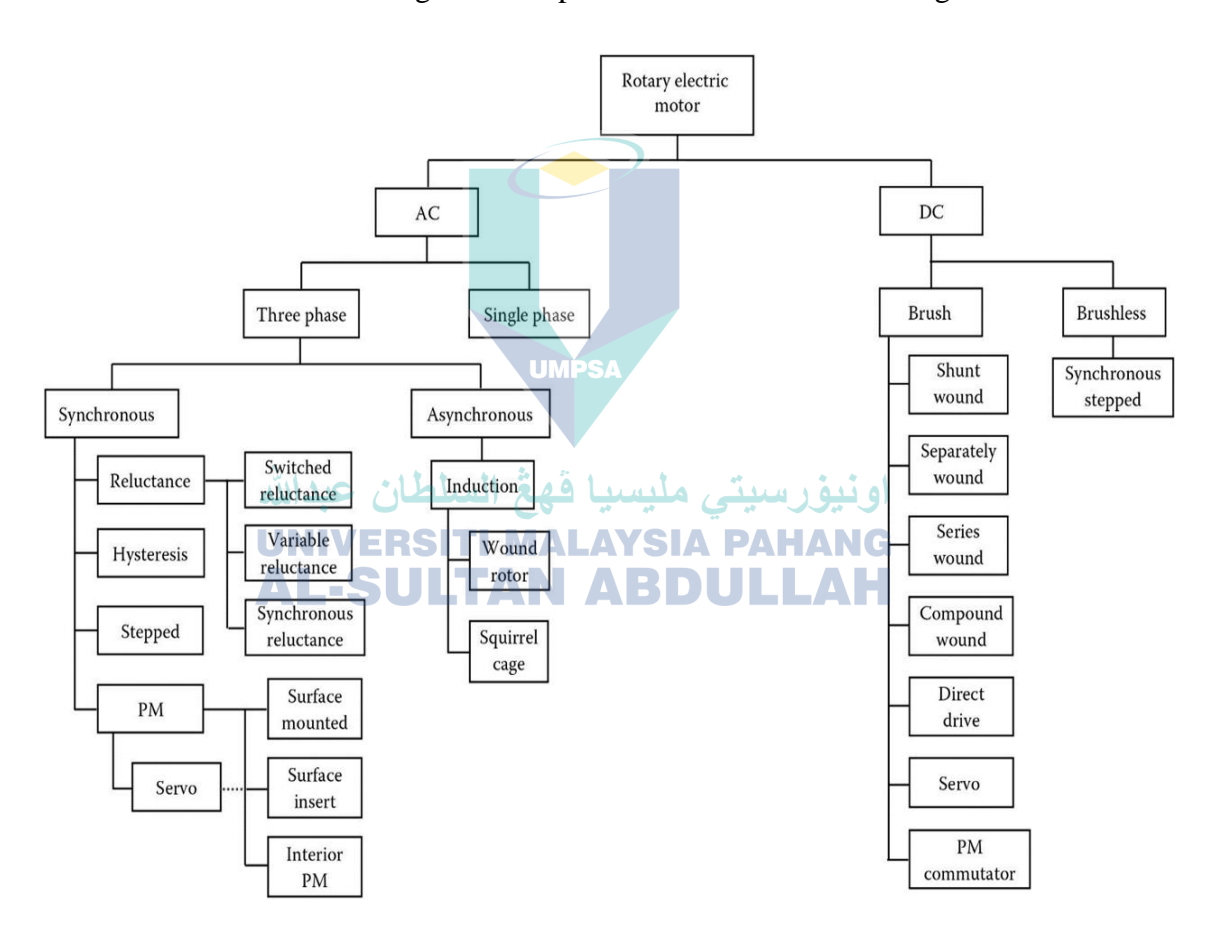


Figure 2.1 Classification of electric machines.

Source: Mechanical Design of Electric Motors (2014)

2.2.1 Utilization and Operating Principle

This subsection discusses the importance of DC machines through the many applications that it fulfils. Additionally, it explains the basic operating principle of DC machines, detailing how the electrical input is being converted into mechanical output. The losses generated from operating these machines that produce the heat will also be explained. This is important to understand the origin of the heat that wanted to monitor through the study in this thesis.

2.2.1.1 Utilization of DC Machines

Brushed DC machines are commonly used in low-voltage applications ranging from 12 to 24 volts, offering cost-effective solutions for auxiliary motors in the automotive industry. These motors are so prevalent that today's premium automobiles may contain up to 80 individual motors as shown in Figure 2.2. DC machines provide significant advantages in systems such as steering, braking, fuel injection, starter/generator, active suspension, and cruise control. Since 1999, DC machines have been utilized in electric power steering systems (J. Li, 2020).

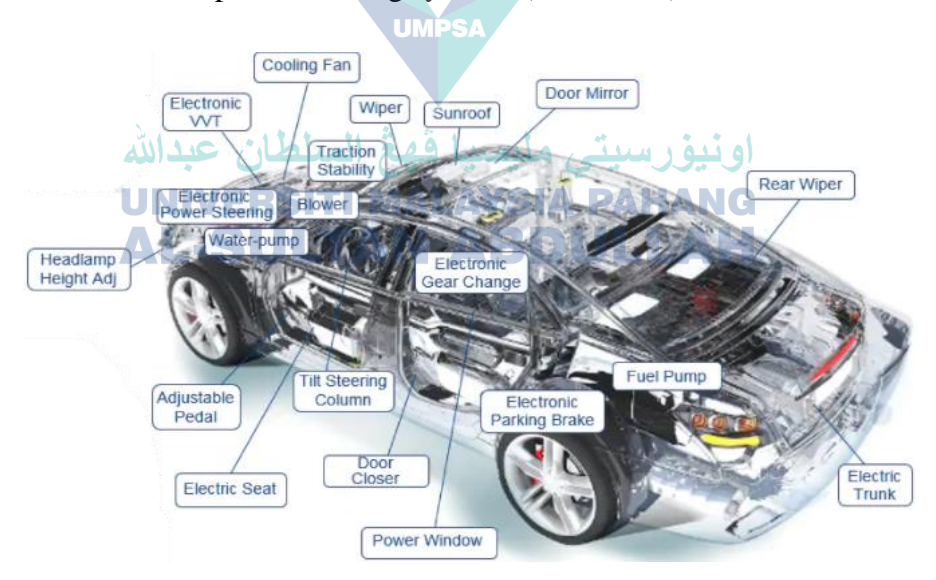


Figure 2.2 BLDC motor installed in a car.

Source: Automotive Brushless DC (BLDC) Motor Application – Diodes Inc (2019)

While most automobiles currently use rotary valve hydraulic power steering systems, a growing number are transitioning to electric power steering systems, which have a noticeable impact on energy conservation. It offers numerous benefits, including energy savings, environmental protection, and enhanced assist features (Cioboată et al., 2020). Next generation steering systems such as steer by wire, necessitate motors that are fault tolerant, have a high-power density, and are more controllable. The controllability of the motor is crucial in such active steering systems, where the vehicle can override driver inputs to ensure safe operation.

Table 2.1 lists a partial summary of current electric machine applications in automotive. It includes starter motor (Midya et al., 2023), alternator (El-Hasan, 2018), air conditioning compressor drive (Patel & Patel, 2019), engine throttle control (Acho et al., 2020), transmission shifter, engine coolant pump motor (Kiesenhofer, 2021), EGR actuator(Gutfrind et al., 2015), windshield wipers (Sharveswaran & Nirmal, 2020), window lifts(Idalgo et al., 2019), seat adjuster, sunroof actuators(Ai et al., 2018), sliding door closers (J. Yu et al., 2019) and steering column adjuster (Cioboată et al., 2020).

Table 2.1 Summary of current electric machines applications.

Author	Title	Type of motor	Applications
Kiesenhofer	Assessment of an Electrical Coolant	Dc machines	Engine coolant pump
2021	Pump on Heavy-Duty Diesel Engine	le ingelinies	motor
	Energy Consumption Comparison	A PAHANG	
Gutfrind et al.	between Two Optimized Limited	Durand DC	
2015	Motion Actuator Topologies for an	Brushed DC machines	EGR actuator
2013	EGR System used in Automotive		
	Applications		
Sharveswaran	Research Development on Wiper		
and Nirmal	Mechanism in Automotive	PMDC machines	Windshield wipers
2020	Application: A Critical Review		
Idalgo et al.	Dc Motor Model for Windows Pinch	Brushed DC	Window lifts
2019	Protection Applications	machines	WINDOW IIIIS
	Smart Pinch Detection for Car's		
Ai et al. 2018	Electric Sunroof Based on Estimation	Dc machines	Common of a street and
Ai et al. 2018	and Compensation of System		Sunroof actuators
	Disturbance		

Table 2.1 Continued.

Author	Title	Type of motor	Applications
	Development of a hardware-in-the-		
I. W 1 2010	loop simulation system for power seat	Dc machines	Cl. 1 1 1
J. Yu et al. 2019	and power trunk electronic control		Sliding door closers
	unit validation		
Patel and Patel	Experimental Investigation and		A :
1 4001 4110 1 4001	Performance Analysis of an	BLDC machines	Air conditioning
2019	Automobile Air Conditioning System		system
Vossos et al.	Dc Appliances and DC Power	Damashinas	Refrigerator, ceiling
2017	Distribution	Dc machines	fan, air conditioner

2.2.1.2 Operating Principles of DC machines

Brushed DC machines typically consist of four key components: the armature winding, commutator, brushes, and a permanent magnet, as illustrated in Figure 2.3. As the motor rotates, carbon brushes slide over the commutator, contacting its different segments. These segments are connected to the armature windings, creating a distributed magnetic field inside the rotor when voltage is applied across the brushes.

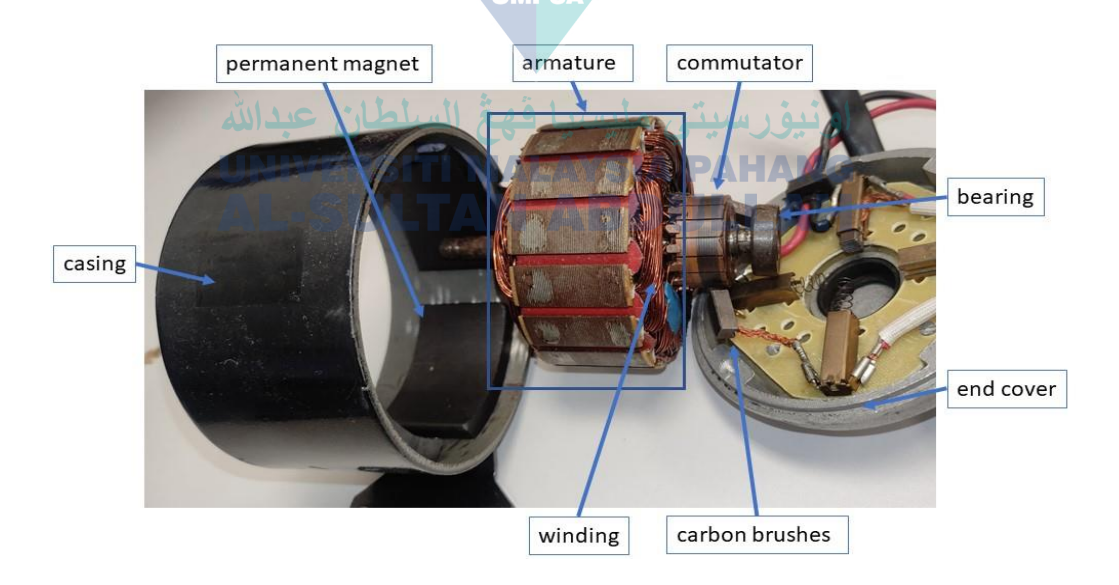


Figure 2.3 Structure and components of brushed DC machines.

The brushes and commutator play crucial roles in ensuring the continuous rotation of DC machines. Figure 2.4 depicts a one-turn coil in a rotor winding. When this coil is connected to a DC power supply, current flows through it. Initially, the flux distribution and the current flowing in the coil resemble. Under these conditions, the force exerted on the conductors on both sides causes the coil to rotate clockwise, as dictated by the Lorentz Force law in Equation 2.1. With F_{ν} the force density, B the flux density, and J the current density.

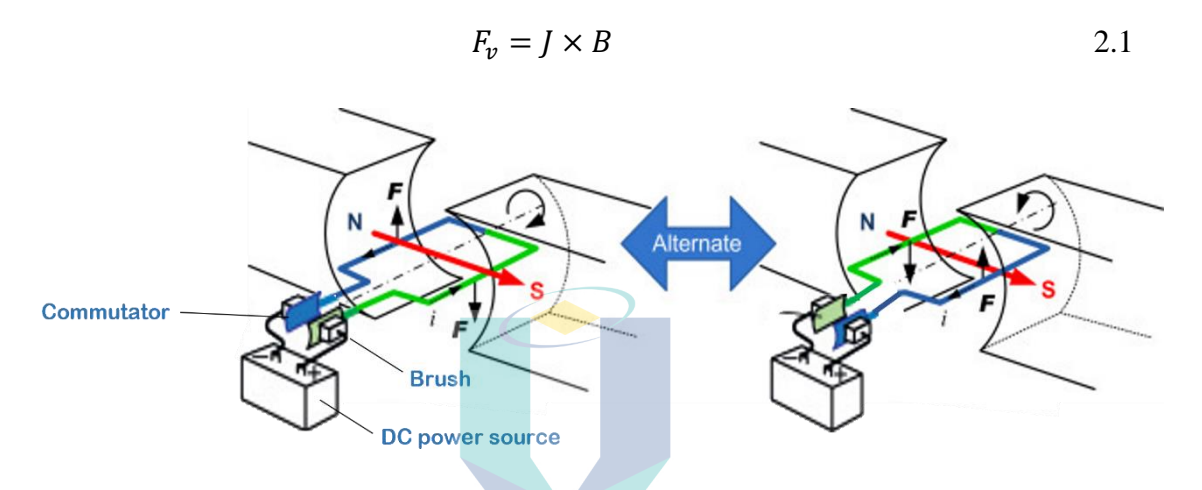
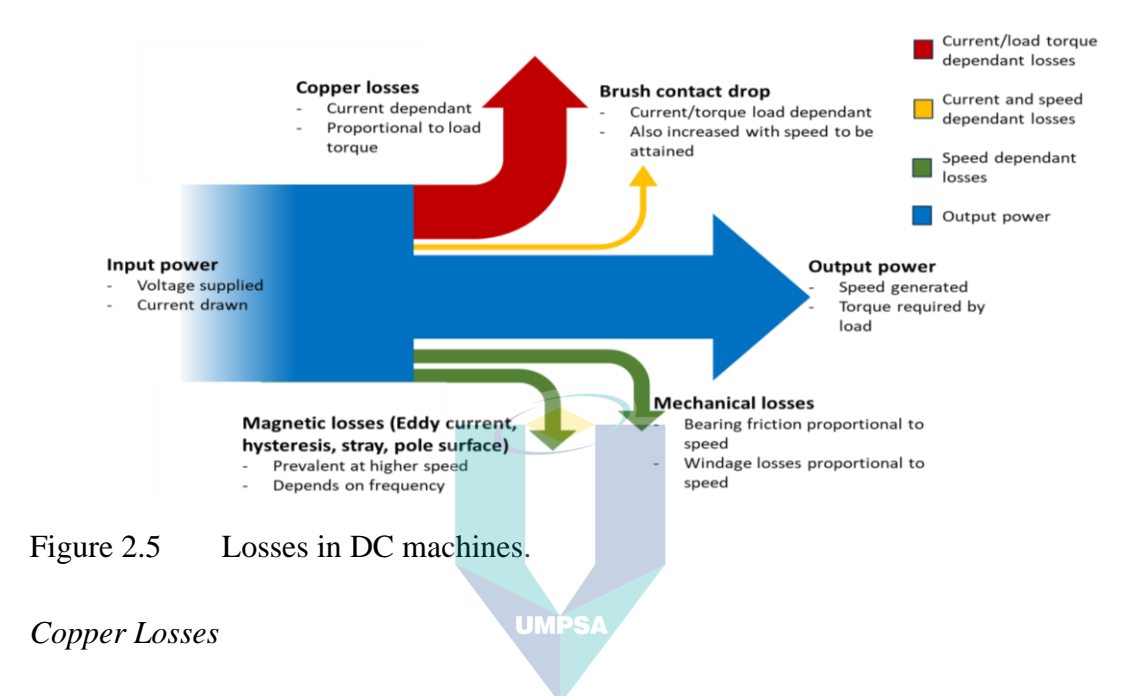


Figure 2.4 Force on a one-turn coil MPSA Source: Electric Motor Control (2017)

As the coil rotates due to the Lorentz force to the position shown in the figure on the right, the force produced on the conductors on both sides would naturally return the coil to its initial position, as depicted on the left side of Figure 2.4. Since the force on the coil is not continuously produced in one direction, the coil cannot rotate in the same direction indefinitely. However, if the current's direction is reversed when the coil reaches the position shown on the right thanks to the commutator sections and brush, the force on the conductors on both sides will also reverse, maintaining the clockwise force on the coil. Consequently, the coil will continue to rotate in the clockwise direction.

2.2.2 Losses in Electrical Machine

The losses in DC machines manifest as heat, which consequently increases the machine's temperature. These losses also diminish the electric machine's efficiency (Pecinka et al., 2017). The types of losses in electrical machines include copper losses, magnetic losses, and mechanical losses, as depicted in Figure 2.5.



Copper loss in a motor refers to the energy loss that occurs due to the resistance of the copper windings in the stator and rotor of the motor. This loss is caused by the flow of electrical current through the copper windings, which generates heat and reduces the overall efficiency of the motor (Q. Zhang et al., 2019). In brushed DC machines, it can be quantified by experimentally measuring the current going through the armature winding and calculate using Equation 2.2. Where $P_{armature}$ is the armature copper loss, I_a is the armature current (A), R_a the armature resistance (Ω).

$$P_{armature} = I_a^2. R_a 2.2$$

Therefore, this loss of energy is converted into heat, which can lead to thermal stress and damage to the motor winding insulation if not effectively managed. (Q. Zhang et al., 2019) study on variation of load and speed cause excess copper loss also reduce performance of electrical machines. The reason is, with the load increasing the EMF in

the stator winding is decreasing due to the rising voltage, consumed by the winding resistance and leakage reactance. Other factor of copper losses was affected by winding wire diameter. The smaller the wire diameter, the more copper losses will be generated (W. Yu et al., 2022). In summary, copper losses in a motor is reduces the overall efficiency and increase in heat generated and need to be evacuated (Y. Liang et al., 2021).

Magnetic Losses

Magnetic losses constitute the second category of losses that lead to excessive temperatures in electric machines (Ma et al., 2022). The term 'magnetic losses' in a motor refers to the loss of magnetic energy due to eddy currents generated within the motor's iron core. The iron loss separation theory suggests that core losses, caused by any magnetic flux density waveform in each stator core unit, consist of hysteresis loss, eddy current loss (C. W. Kim et al., 2017) and excess loss (Cuiping et al., 2014). In brushed DC machines, P_h hysteresis loss and P_e eddy current loss can be calculated using Equation 2.3 and Equation 2.4 respectively. Where k_h hysteresis coefficient, f frequency of magnetization, B_m maximum flux density and v volume of magnetic material.

$$Ph=kh.f.Bm1.6.v$$
 2.3

$$P_e = k_e \cdot f^2 \cdot B_m^2 \cdot t^2 \cdot v$$

$$VSIA PAHANG$$

Where k_e eddy current coefficient, f frequency of magnetization, B_m maximum flux density, t thickness of each lamination and v volume of magnetic material. Despite the continuous current supply, the rotation of the armature core inside the constant stator field produces small amount of harmonic of induced emf and generate iron losses in it.

Magnetic loss in a DC motor significantly affects the motor's performance and efficiency (Ma et al., 2022). Consequently, researchers like (P. Kumar et al., 2022) have investigated how the performance of DC motor is affected when the model incorporates the impact of iron loss. In the case of brushless DC permanent magnet motors, (X. Wang et al., 2019) have employed soft magnetic composite stators to reduce iron loss and temperature, offering an advantage over traditional laminated materials.

Mechanical Losses

Mechanical losses contribute to the degradation of motor performance and efficiency (Gao et al., 2023), while simultaneously causing excessive temperature increases. Mechanical losses are defined as the energy produced by the motor that is not converted into mechanical work. The primary sources of mechanical losses include friction, windage, and bearing losses, which also significantly contribute to the rise in motor temperature. As the motor's required torque and speed increase, the supplied current rises accordingly, leading to greater mechanical losses and, as a result, higher temperatures. In Figure 2.6, mechanical losses affected electric machines where increasing loss caused decreased speed, as confirmed by (Gao et al., 2023). The relation between the speed and losses is non-linear and complex. Furthermore, studies by (Wrobel et al., 2015) have examined the components of mechanical loss in conjunction with rotor heat transfer effects. Additionally, research by (S. H. Park et al., 2021) has focused on predicting mechanical losses by considering the eddy current losses of permanent magnets and conductors under no-load conditions.

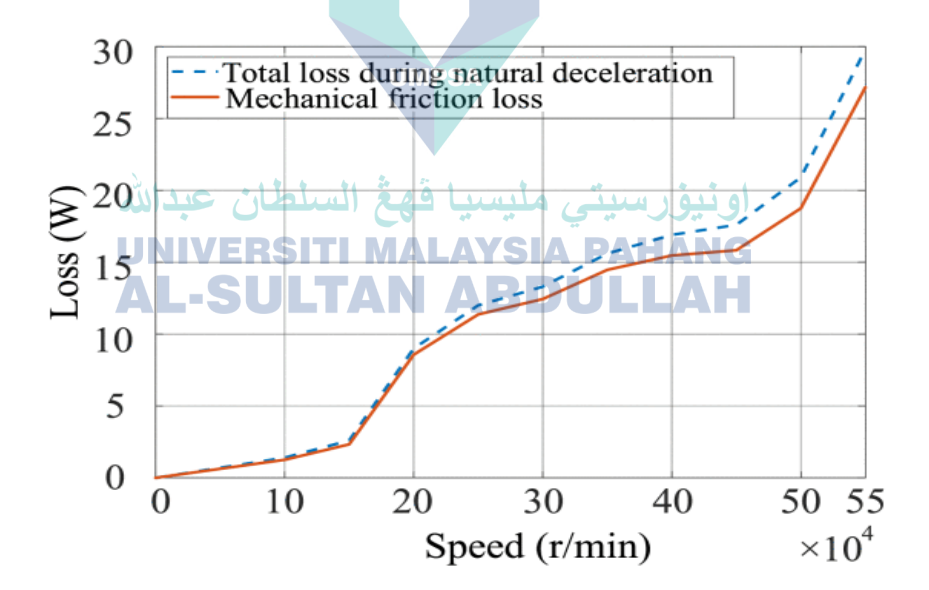


Figure 2.6 Graph losses vs speed.

Source: Gao et al. (2023)

The prediction of the mechanical losses is more complex with the involvement of windage losses. Windage losses are caused by the mutual friction between the rotor and the surrounding air. Air friction loss is related to the rotor surface structure, surface roughness, motor speed, air density, air velocity, air radial pressure, and other factors(Ji et al., 2021). Many researchers, including (Abdelli et al., 2020; Gao et al., 2023) developed experiments, models, and simulations to diagnose and analyse the characteristic of mechanical losses in electric machines. The rise of mechanical loss depending on the variation of speed electrical machines (Y. He et al., 2021).

Table 2.2 provides a summary of research papers focusing on the losses in electrical machines. The studies reveal that as losses increase, the efficiency and performance of these machines decrease, and not necessarily linearly and predictably. These losses also cause a rise in the machine's operating temperature, as not all electrical energy is successfully converted into mechanical energy. Excessive temperatures can lead to considerable damage to the electrical motors. Therefore, it is crucial to model the temperature response for effective condition monitoring of these machines.

Table 2.2 Summary of losses.

UMPSA					
Author	Title	Type of Losses	Summary		
W. Yu et al. 2022	Comparative Analysis of AC Copper Loss with Round Copper Wire and Flat Copper Wire of High-Speed Stator-PM Flux- Switching Machine	Copper Losses	AC copper losses in FSPM are influenced by wire diameter, phase current variation, and motor speed		
Q. Zhang et al. 2019	Minimum Copper Loss Direct Torque Control of Brushless DC Motor Drive in Electric and Hybr Electric Vehicles	Copper id Losses	Copper losses in electric machines reduce motor efficiency and lifespan due to coil temperature rise.		
Ma et al. 2022	Studies on Loss of a Motor Stator Iron Core with High Silicon Electrical Steel Considering Temperature and Compressive Stress Factors	Magnetic Losses	Temperature and stress significantly impact the iron loss and performance of a PMSM.		

Table 2.2 Continued.

Author	Title	Type of Losses	Summary
	Disturbance Observer Based		Saturation and peak flux density
P. Kumar et	Sensorless Predictive Control for	Magnetic	variations in the flux path are
al. 2022	High Performance PMBLDCM	Losses	
	Drive Considering Iron Loss		influenced by temperature changes.
	Loss Calculation, Analysis, and		Mechanical friction in the rotor
Gao et al.	Separation Method of 550 000	Friction	causes significant loss, reducing
2023	r/min Ultrahigh-Speed Permanen	t Losses	motor efficiency and increasing rotor
	Magnet Motor		temperature.
	Prediction of Mechanical Loss fo	r	Windage loss, caused by friction
Park et al.	High-Power-Density PMSM	Windage	between air gap fluids and the rotor,
2021	Considering Eddy Current Loss of	of Losses	makes mechanical loss dependent on
	PMs and Conductors		rotor speed.

2.3 Temperature Rises in Electrical Machine

Following the operating principle and the origin of losses, this subsection will deal with the consequent of it and the potential way to closely monitor it. It is divided into two parts: the first addresses the causes of degradation and heat transfer in electric machines. It discusses the impact of excessive temperature on electric machines and the mechanisms of heat flow within them. The second part focuses on monitoring, modelling temperature responses, and diagnostics from a thermal perspective. It explains the tools used to monitor the condition of electrical machines, the methods employed for design, detection, and analysis, and the techniques used to detect and diagnose faults in electrical machines.

2.3.1 Cause of Degradation and Heat Transfer

This subsection details the degradation causes in electrical machines from excessive temperatures, leading to partial discharge, inter-turn short circuit, demagnetization of permanent magnets, and mechanical faults. It also examines heat transfer within electrical machines, focusing on heat flow through conduction, convection, and radiation.

2.3.1.1 Cause of Degradation

Elevated temperatures can damage electric machines, critically affecting and damaging the winding insulation and the permanent magnets.

Partial Discharge

In electric machines, winding insulation is susceptible to thermal damage, primarily in the form of partial discharge. This phenomenon is a complex interplay of electrical, thermal, and physical forces acting simultaneously within flawed insulation, as detailed by (Q. Khan et al., 2020). The IEC 60270:2000 standard characterizes partial discharges as localized, low-magnitude electrical discharges that occur within insulation gaps caused by uneven electrical stress and charge distribution, potentially away from conductors.

Elevated winding temperatures, contingent upon the insulation's thermal classification, trigger chemical reactions mostly oxidationthat progressively deteriorate the epoxy bonding material's electrical and mechanical integrity. As temperatures rise, the epoxy may vaporize, weakening its bond with the mica paper tape layers (or other winding insulation paper), leading to increased vibration of copper strands and turns under 120 Hz magnetic forces (Stone et al., 2007). This vibration causes abrasion of the insulation and, as (Stone et al., 2007) observed, eventually results in electrical shorts.

Recognizing the harmful impact of partial discharge, (Abadie et al., 2019) have developed a system to identify its presence within winding insulation. Complementing this (Q. Khan et al., 2020) utilized finite element modelling to investigate the behaviours within the insulation. Various techniques, such as CNN model (Akram et al., 2023) to monitor the health of electric motor insulation and Paschen's law by (Mathurin et al., 2020) have been employed to predict partial discharge at the design phase.

Additionally, thermal stress in electrical machines arises during prolonged operation under overload conditions, necessitating high currents to match speed with load demands. According to (Bonnett & Soukup, 1992) insulation life expectancy halves with every 10°C increase in temperature. Figure 2.7 show of four classes of insulation are A,

B, F and H. Class F is the most widely used, with each class's specifications determined by testing procedures on rotating machines, following standards from IEEE 275 and AIEE 510. Operating a motor beyond the designated temperature for its class significantly shortens its lifespan, contrary to its expected operational capacity.

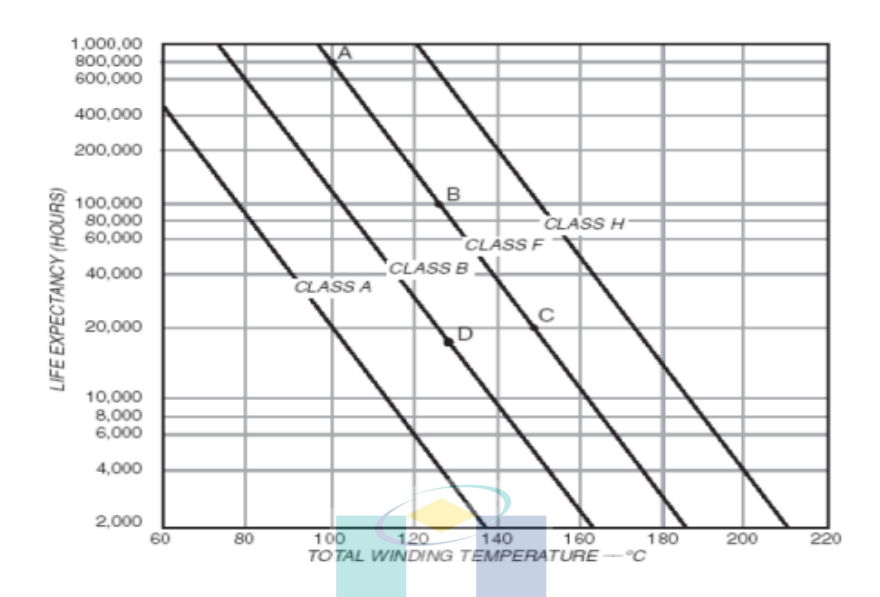


Figure 2.7 Temperature vs. life curves for insulation systems for different class of machines of the same type.

Source: Vaseghi et al. (2011) UMPSA

Inter-turn Short Circuit

اونيؤر سيتي مليسيا فهغ السلطان عيدالله

Additionally, thermal effects can induce a variety of faults in electrical machines, including short-circuit faults, which account for 21% of all faults (X. Liang, 2019). It is reported that most short-circuit faults originate as interturn faults, which are caused by the elevated level of circulating current heating the insulation of the coil adjacent to the shorted turns. This heating increases the severity of the fault (Vaseghi et al., 2011). and leads to an asymmetry in the stator winding temperature distribution due to localized heating in the faulty coil (P. S. Kumar et al., 2021). Furthermore, the short-circuit loop current opposes the normal stator current, resulting in a reduction in the magneto-motive force of the faulty coil. This, in turn, leads to an asymmetry in the air-gap magnetic field distribution along the stator periphery. Although there is no experimental data indicating the time delay between inter-turn and ground wall insulation failure, it is likely that the transition between these two states is not instantaneous (Lee et al., 2005).

Faults in the winding are considered a critical type of fault in motors. Initially, they may not show any external signs of warning. However, over time, they can become the root cause of excessive heat, imbalanced line currents, reduction in torque, unusual vibration, and overheating (Cao et al., 2023). In some cases, a minor insulation break in the winding can lead to a complete breakdown of the motor's operation. In industrial applications, this can result in catastrophic damage to property and pose serious risks to human safety (Shifat & Hur, 2020).

An inter-turn short circuit fault, as shown in Figure 2.8, signifies insulation failure between two coils in the same phase, creating extremely low resistance between turn R_f and increase the current i_f drastically. The heat generated in the short circuit is proportional to the square of the circulating current, which can cause insulation breakdown in the adjacent coil (J. K. Park et al., 2015).

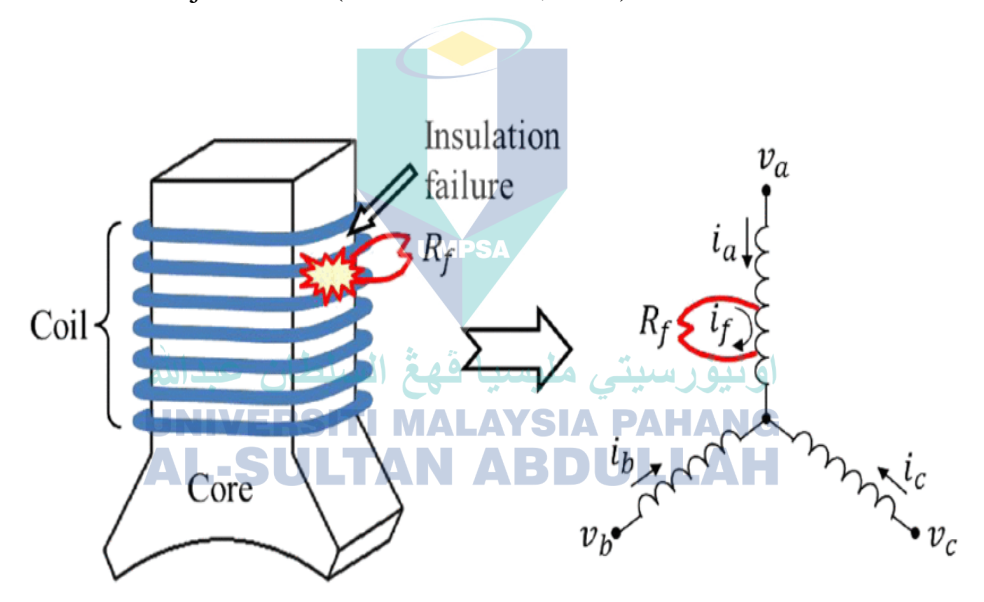


Figure 2.8 Interturn fault occurrence in a single phase.

Source: Park et al. (2015)

Demagnetization of Permanent Magnet

In addition to the damage that occurs in winding insulation, thermal effects can also be detrimental to the second most critical component in electric machines, the permanent magnet. This may happen due to excessive heat generated from copper losses, interturn faults and mechanical faults. Each permanent magnet has a different Curie temperature, as shown in Table 2.3. The Curie temperature is critical because it is the point at which a permanent magnet can be irreversibly demagnetized. Below the Curie temperature, the material has a high and constant permeability and remanent, an associated magnetic field that is difficult to change. However, when the temperature exceeds the Curie temperature, the material becomes a paramagnet, and its magnetic field can easily change with variations in the surrounding magnetic field.

Table 2.3 Comparison of permanent magnet properties.

Magnet typ	be $\frac{BH_{max,}}{[MGOe]}$		lux Densi [G]	ty, Working Temp. [°C]	Curie Temp. T _c , [°C]
Ferrite	3.3		1000	250	460
Alnico	5.2	UM	PS1300	550	860
SmCo	26		3500	300	750
NdFeB	ما 38 رم عبد الله	قمغ الس	4500	120	320

Source: Seol et al. (2017) ULTAN ABDULLAH

Demagnetization can be classified into two types: reversible and irreversible. Reversible demagnetization is induced by field-weakening control, while irreversible demagnetization results in permanently weakened magnets. A major cause of irreversible demagnetization is an improper operating point of the rotating electrical machine, which can occur due to the combined effect of temperature and a shift in the permeance curve (M. S. Khan et al., 2018). Demagnetization reduces the torque of the electrical machine because the electromagnetic torque is proportional to the cross-product of the current vector and the permanent magnet flux linkage vector (Seol et al., 2017). As demagnetization reduces the output torque of the machine, it severely worsens the motor's characteristics and efficiency (D. H. Kim et al., 2020).

Mechanical Bearing Fault

In addition to faults caused by temperature, other faults generate heat in rotating electrical machines. These faults fall into the category of mechanical faults, one of which is the bearing fault. Furthermore, improper operation, such as misalignment or overloading, can accelerate the degradation of the bearing (De Jesus Rangel-Magdaleno, 2021). Another study by (Brusamarello et al., 2023) demonstrated its importance by developing a classification of bearing fault severity levels using a support vector machine classifier. Using Dynamic Convolutional Neural Network, (Jung et al., 2023) has demonstrated that bearing motor dataset may be useful for fault diagnosis.

Brush fault

Brush friction also contributes to heat generation when worn, as evidenced by studies from (Huang et al., 2023) and (Rasid et al., 2022). Brushes in electrical machines mostly experience two types of wear: mechanical wear caused by friction and electrical wear due to current passing through the contact interface. The primary mechanism of mechanical wear in carbon brushes involves the formation of micro-cracks, their growth due to mechanical and thermal stresses, and the eventual detachment of wear particles as the cracks expand and multiply. This has been long eluded from studies such as (Braunovic et al., 2006) and (Hu et al., 2008). Ensuring low mechanical wear requires a stable friction layer on the contact surface, which increases the contact area and reduces friction, temperature, and arcing (Groth et al., 2001). This implies that a degrading brush will increase the friction and temperature. Various recent methods have been employed to model and monitor the brush wear. These include current signal analysis using different techniques such as discrete wavelet transforms (Ray et al., 2020), empirical modeling using regression approaches (Benedik et al., 2015), and exploiting neural networks on exhaustive historical data (Silva et al., 2023). The three examples mentioned were applied for brush and armature for train traction machines, vacuum cleaners, and general-purpose universal motors respectively. The temperature generated from brush degrading condition however have not been exploited for condition monitoring and diagnostic.

2.3.1.2 Heat Transfer in Electrical Motor

The three main mechanisms of heat transfer that can occur in a motor are conduction, convection, and radiation. Figure 2.9 shows heat transfer direction that takes place in an electric machine, where the heat flows to lower temperature points which is the ambient air (Demetriades et al., 2010).

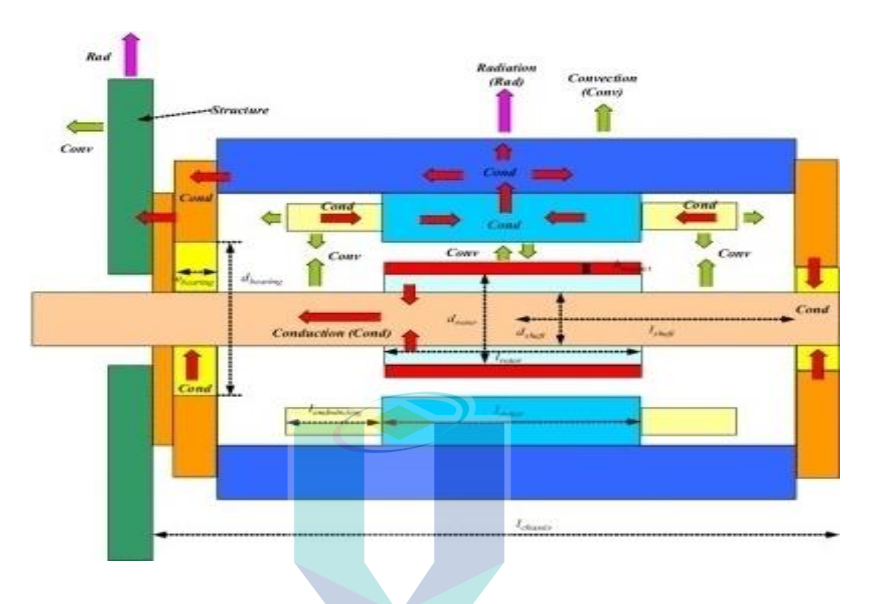


Figure 2.9 Heat transfer flow diagram of PMSM.

Source: Demetriades et al. (2010)

اونيؤرسيتي مليسيا قهڠ السلطان عبدالله UNIVERSITI MALAYSIA PAHANG

Conduction is the transfer of heat in a solid by means of molecular agitation within a material without any motion of the material. In general, conduction can be written in its integral form as in Equation 2.5 according to Fourier law.

$$\dot{Q}_{cond} = \frac{\partial Q_{cond}}{\partial t} = -\lambda \oint_{S} \nabla T. \, \overrightarrow{dA}$$
 2.5

 \dot{Q}_{cond} is the quantity of heat (J) and $\dot{Q}_{cond} = \frac{\partial Q_{cond}}{\partial t}$ is the rate of heat transfer (in W), λ the material's conductivity $(W \cdot m^{-1} \cdot {}^{\circ}C^{-1})$, ∇T is the temperature gradient (${}^{\circ}C \cdot m^{-1}$) and \overrightarrow{dA} is an oriented surface area infinitesimal (m^2) .

In one dimensional form (in \vec{x} direction) where homogeneity and isotropy are considered, the heat flow rate can be written as in Equation 2.6 and the conduction thermal resistance R_{th} (W/m^2 . K) can be written as Equation 2.7

$$\dot{Q}_{cond} = \frac{dQ_{cond}}{dt} = -\lambda A \frac{dT}{dx}$$
 2.6

$$R_{cond} = \frac{\Delta x}{\lambda}$$
 2.7

 R_{cond} calculation is strongly dependent on the thermal conductivity of the material. Most of motor construction material have a very well-known thermal conductivity with minimal uncertainty which means a simple analytical calculation of R_{cond} for conduction is sufficient.

Convection

Convection is the heat transfer through fluids movements. The heat rate transfer can be written using Newton's cooling law as in Equation 2.8.

$$\dot{Q}_{cond} = \frac{dQ_{conv}}{|dt|} = h.A.\Delta T(t)$$
UNIVERSITI MALAYSIA PAHANG

 ΔT is the difference of temperature between the object's surface and the fluid and h is the convection heat transfer coefficient (W/m^2 . K). h depends on various physical properties of the fluid and the physical situation in which convection occurs such as the temperature, the geometrical form, and external air flow influence. Different values were proposed for different conditions (Staton & Cavagnino, 2006). They are nonetheless empirical, thus may not completely suitable for a given system. It is therefore exceedingly difficult to calculate and must be derived or found by experimental identification.

Radiation

Finally, radiation is the heat transfer process through electromagnetic waves from a surface (Blundell S.; Blundell K., 2014). The Stefan-Boltzmann's correlation in Equation 2.9 defines the rate of heat transferred by radiation $\dot{Q}_{rad}(J)$, where is the Stefan-Boltzmann constant (5.67 × 10⁻⁸ $W/m^2/^{\circ}C^4$), A is the area emitting the radiation (m^2) and T the surface temperature (${}^{\circ}C$).

$$\dot{Q}_{rad} = \sigma. A. T^4$$
 2.9

Radiation is difficult to compute as there are not just radiation emitted from the surface, but also radiation received by the surface from other exterior surface in its surroundings. The net radiation heat loss rate can be computed using Equation 2.10.

$$\dot{Q}_{rad} = \sigma.A. \varepsilon. F_{1-2}. (T_1^4 - T_2^4)$$
 2.10

Where ε is the emissivity of the surface, a dimensionless quantity: 0 for absolute reflector such as a mirror, and 1 for absolute absorber such as a black body. F_{1-2} is the view factor of surface 2 with respect to surface 1 which means the proportion of the radiation which leaves surface 1 that strikes surface 2. In a setup where only two entities considered (the machine and its surrounding as a set), the view factor equal to one as result of energy conservation. T_1 is the temperature (°C) of the hot body and T_2 is the cold surrounding temperature (°C). Like convections coefficient h, ε is also difficult to be found and must be derived or found by experimental identification.

Conduction is the process of heat transfer that occurs across all solid parts of the motor. On the other hand, convection and radiation are the processes that occur in the air gap, the interior cavity, and on the exterior surface of the motor that is in contact with the ambient air. In the context of a small air gap and cavity, the convection process can be considered negligible compared to conduction. This is particularly true when the Nusselt number, which represents the ratio of convective to conductive heat transfer across a surface, is very small (Bouafia et al., 1998).

Table 2.4 provides a summary of references that focus on the causes of degradation and heat transfer. It is evident from numerous studies on partial discharge, inter-turn short circuit, demagnetization of permanent magnets, bearing faults, and brush friction that thermal monitoring condition is necessary to detect the occurrence of this faults. It will play a significant role in preventing such faults from occurring or identifying existing faults in rotating electrical machines.

Table 2.4 Summary causes of degradation and heat transfer.

1 D' 1 M 1 11'		
al Discharge Modelling	Partial	Partial discharge is a complex
ernal Discharge in	Discharge	process where electrical, thermal,
rical Machine Stator		and physical interactions occur in
ling		defective insulation.
r End-Winding Thermal	Interturn Fault	An inter-turn short circuit causes
Magnetic Sensor Arrays		high current and uneven heat in the
nline Stator Inter-Turn		stator winding due to a faulty coil.
Detection		
Detection Technique	Interturn Fault	Interturn faults occur when coil
		insulation breaks down under
LDC Motor using	JMPSA	thermal, electrical, and mechanical
dance		stress, leading to continuous
مُ الساطات عبدالله	4 	degradation
Element Modeling of	Demagnetization	The magnet's operating point on the
agnetization Fault in	Permanent	B-H curve drops due to
anent Magnet DC	Magnet	demagnetization, caused by the
ines		stator's magneto-motive force.
Flux-Based Rotation	Bearing Fault	Repeated loads on motor bearings
e Measurement for		cause stress, leading to initial issues
ng Fault Diagnosis in		like cracks that can worsen into
ble-Speed BLDC		broken cages and worn raceways.
ines		
		Motor construction materials have
nal Network Modeling		known thermal conductivity,
book	Conduction	allowing for simple calculations of
		resistance conduction.
	rernal Discharge in rical Machine Stator ling rend-Winding Thermal Magnetic Sensor Arrays reline Stator Inter-Turn Detection Detection Technique tator Winding Inter-turn LDC Motor using dance de Element Modeling of agnetization Fault in anent Magnet DC lines Flux-Based Rotation de Measurement for the Measurement for the Measurement for the Speed BLDC lines mal Network Modeling book	rical Machine Stator ling r End-Winding Thermal Magnetic Sensor Arrays nline Stator Inter-Turn Detection Detection Technique tator Winding Inter-turn LDC Motor using dance e Element Modeling of agnetization Fault in anent Magnet DC ines Permanent Magnet Bearing Fault e Measurement for ng Fault Diagnosis in able-Speed BLDC ines Conduction Interturn Fault Magnet Interturn Fault Interturn F

Table 2.4 Continued.

Author	Title	Type of Fault	Summary
	Convection heat transfer and		The convection heat transfer
Staton et	flow calculations suitable for	Convection	coefficient depends on the fluid's
al. 2006	analytical modelling of		properties, temperature, geometry,
	electric machines		and external airflow.
			Calculating radiation is complex due
Blundell 2014	Concepts in Modern Physics	Dadiation	to both emission from the surface
		Radiation	and reception from surrounding
			surfaces.

2.3.2 Monitoring, Modelling Temperature Response and Diagnostic

Following the review of potential causes of temperature rise, it is necessary to monitor the machine temperature to not damage it. Consequently, this subsection overviews different instrumentations used in monitoring the temperature of an electrical machine, types of models used to predict temperature response in electrical machines, and fault diagnostic methods. It highlights the advantages and inconveniences of each solution, which later allow us to choose a suitable method in our research.

2.3.2.1 Monitoring Temperature Response

In the presence of potential excessive temperature, there is a need for instrumentations for temperature monitoring on electric machines. Among the methods used for this purpose are thermocouples, thermal imaging, and infrared thermometers.

Thermocouple Instrumentation

A thermocouple instrument measures temperature by utilizing the thermoelectric effect. It consists of two dissimilar metal wires, joined at one end to form a junction. Diverse types of thermocouples, such as the J or K type, use different mixtures of metals in the cable. The millivolt value provided by the thermocouple at the cold junction compensation end represents the difference in temperature of the sensing end compared to the cold junction compensation end.

Thermocouples are the most used temperature-measuring instruments in the industry, enabling the measurement of a wide temperature range with a relative error of 1-2% (Fedosov, 2020). In the context of monitoring motor conditions, a thermocouple can measure the temperature of motor components such as the winding, permanent magnet, rotor (C. Liu et al., 2021), casing, and bearing. This data can provide insight into the motor's condition and performance issues such as overheating or mechanical faults. It can be used to optimize the motor's performance and ensure that it is operating within its recommended temperature range. Thermocouples are valuable tools for monitoring motor condition(Upadhyay et al., 2019), providing accurate and precise data for proactive maintenance(N. Khan et al., 2019). They are widely used in harsh conditions due to their low cost, robustness, and reliability(Seung et al., 2022).

However, thermocouples may deteriorate during operation (Dong et al., 2020) and their error dramatically increases. In 90% of cases, deterioration is related to chemical and metallurgical changes in the wires, progressing thermoelectric inhomogeneity, and reduction of insulation material resistance (Rogel'berg, n.d.). This deterioration is an irreversible but predictable process. Furthermore, its cost is very low and can be easily replaceable with the condition that the components to be measured are accessible.

اونیورسیتی ملیسیا قهعٔ السلطان عبدالله Thermal Image Instrumentation

Another method used in monitoring motor conditions is thermal imaging. A thermal image instrument, also known as a thermal camera or infrared camera, captures and displays the infrared radiation emitted by objects, allowing the user to see heat patterns. In the context of monitoring motor condition(Badoni & Jarial, 2021), a thermal image instrument can be used to identify hot spots or areas of increased temperature on the motor and its components (Khamisan et al., 2018). The instrument captures an image of the motor and displays it in a color-coded format, where different temperatures are represented by assorted colours. This allows for easy identification of areas of the motor that are running at higher temperatures than normal. For example, an armature winding that is running hot may be displayed as red or orange, while a cooler area of the motor may be displayed as blue or green.

The advantage of a thermal image instrument in monitoring motor conditions is that it is a non-invasive (Z. Xu et al., 2022) and efficient way of assessing the temperature variations on the motor's components (Badoni & Jarial, 2021) and its surrounding environment (Khamisan et al., 2018). However, thermal imaging has some limitations in monitoring conditions. According to a study (Chou & Yao, 2009) it is unable to detect the inside temperature if the inspected object is separated by a non-transparent medium for IRT radiation, such as glass or other covers. Like thermal imaging but measuring localized points is an infrared thermometer. This tool uses infrared laser technology to measure surface temperature but only at a single point (Zeng et al., 2014). It shares the same inconvenience as the thermal image, where the imprecision temperature of the thermal image only measures a single point and is non-exhaustive like a thermal image. This method is not widely used, and if it is, it is typically only for preliminary results.

2.3.2.2 Modelling Temperature Response

Instead of monitoring the temperature response of electric machines using instrumentation, modelling is another method that can be used to estimate the temperature of an electrical machine. Several methods can be used for modelling temperature response, such as Finite Element Modelling (FEM) and Lumped Parameter Thermal Network (LPTN).

اونيورسيتي مليسيا فهغ السلطان عبدالله Finite Element Model VERSITI MALAYSIA PAHANG AL-SULTAN ABDULLAH

FEM can accurately simulate the temperature distribution within the motor and predict the temperature rise during operation. It is a numerical method for solving a differential or integral equation, used to solve several physical problems with the help of governing differential equations (Anoop et al., 2020). FEM divides a large geometry into small elements that can be solved in relation to each other. It is useful for problems where analytical solutions cannot be obtained (Z. Liu et al., 2021) and is used in complicated geometries, loadings, and material properties (Yang et al., 2019). This allows for a detailed analysis of the temperature response of the motor.

FEM has several advantages for simulating the temperature response of electric machines. One advantage is its accuracy (Z. Liu et al., 2021). The method can provide detailed information about the temperature distribution within the motor. Another advantage is its flexibility. FEM can be used to simulate a wide range of scenarios, including different operating conditions and analysis designs. However, it can be computationally intensive, as solving the equations for many elements can require significant computing power and time resources (Craiu et al., 2010).

Many researchers use finite element models to monitor and analyze temperature rise in electric machines. For example, (Zhao et al., 2022) used a 3-D finite element model to analyze temperature estimation for induction motors at stator winding and rotor under different conditions, including under load and overload conditions. Meanwhile, (Shen et al., 2021) combine the FEM and Fourier models to provide a balance between computational efficiency and accuracy, especially useful for analyzing PMSMs with different numbers of poles or slots and suitable for diverse types of machines. Figure 2.10 shows the temperature distribution in the stator of an induction motor which is obtained from thermal analysis in ANSYS Mechanical platform done by (Anoop et al., 2020). From this figure, it is concluded that the stator slot has the highest temperature as 143 °C and end covers have the lowest temperature as 109 °C in stator geometry.

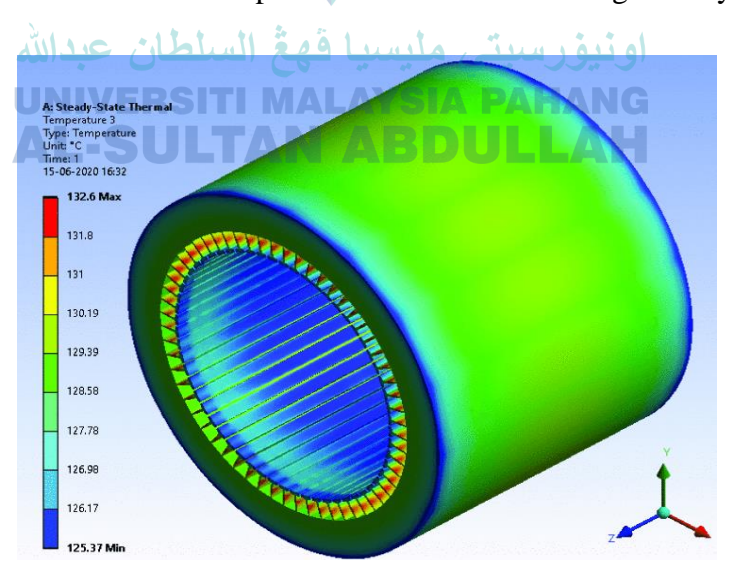


Figure 2.10 Temperature distribution in stator induction motor.

Source: Anoop et al. (2020)

Lumped Parameter Thermal Network

Other than finite element modeling, researchers have also extensively utilized another method known as the Lumped-Parameter Thermal Network (LPTN) model. Among the researchers who used LPTN as a thermal model for their study, (D. Liang et al., 2022; Phuc et al., 2021) conducted research on detecting temperature at the rotor and stator windings in real-time using the LPTN model for permanent magnet synchronous motor. Meanwhile, low-order LPTN, which offers more robustness and low computational cost, was implemented by (Gedlu et al., 2021; E. Wang et al., 2022) for estimation and analysis of temperature on synchronous motor.

The LPTN model is a mathematical representation of a physical system of the machine. It consists of interconnected thermal resistances, capacitances, and heat sources (Wockinger et al., 2023). This model posits that the system consists of discrete thermal nodes, each with specific temperature and thermal capacity, connected via thermal resistances representing heat transfer. The LPTN model abstracts the system's temperature and heat flow distribution into these discrete nodes. For instance, Figure 2.11 shows the complete LPTN model of the synchronous reluctance motor (Azri et al., 2016), with only copper losses shown. The model was reduced to one single pole radially and to half of the axial dimension.

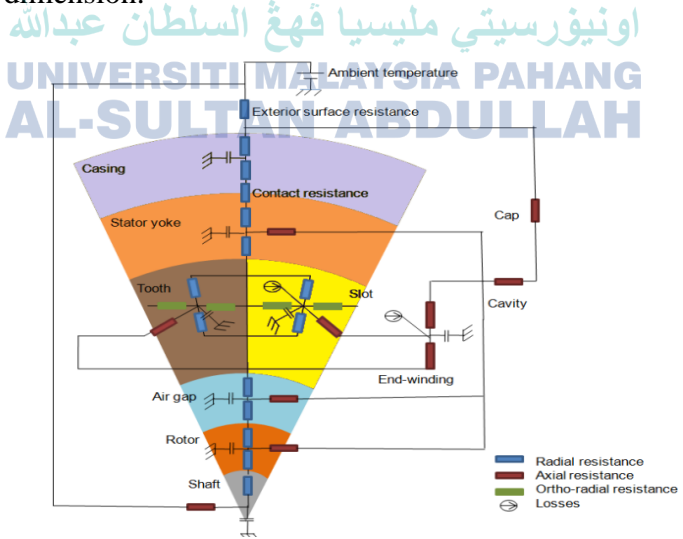


Figure 2.11 Lumped Parameter model of the Syncrel motor.

Source: Azri et al. (2016)

One of the primary advantages of the LPTN model is its simplicity. Its mathematical representation is simple, and it requires minimal computational resources (H. Xu et al., 2020), making it easy to implement in various applications(D. Liang et al., 2022). The precision is high where the lumps are being discretized in high resolution, where more temperature distribution information is needed. The model's simplicity also makes it easy to modify and adapt to different thermal systems and conditions. Additionally, the model provides a good approximation of the temperature distribution across the system and the response to various thermal inputs.

However, there are also some limitations to using LPTNs to model the temperature response of electric machines. These models rely on several assumptions and simplifications, which can limit their accuracy in certain situations (Phuc et al., 2021). Additionally, LPTNs may not be able to capture all the complex heat transfer processes(E. Wang et al., 2022) that occur within an electric machine due to the selective and variable lumps resolution. Another disadvantage is that it requires expertise in both LPTN and electric machine design(Gedlu et al., 2021). A deep understanding of both fields is necessary to accurately simulate the temperature response of electric machines using it.

2.3.2.3 Diagnostic Method اونیورسیتی ملیسیا قهعٔ السلطان عبدالله

Temperature monitoring and modeling will be useful if its data is employed for diagnostic purposes in identifying the machine potential fault. Various diagnostic methods have been proposed for diverse types of motor faults, such as bearing faults, stator winding faults, rotor faults, and air gap eccentricity. These methods include MCSA, VASA, and TSA which vary in terms of their complexity of implementation.

Motor Current Signature Analysis (MCSA)

MCSA is a widely used technique that analyses motor current waveforms using signal processing algorithms like FFT and wavelet. Different currents, such as sequence components, stator currents, shaft currents, and radio frequency components of neutral current, are used for MCSA(Niu et al., 2023). (Ray et al., 2021) and (Avina-Corral et al., 2021) proposed feature extraction of stator current analysis for stator winding fault and

bearing fault in induction motors. Meanwhile, (Shifat & Hur, 2020) proposed the FDD method of brushless DC motor by feature extraction for failure classification from line current. MCSA can be useful in industries where electric machines are used, enabling non-intrusive online (even remote) analysis of motor supply current and identifying faults while the motor is still operational and without disturbing its operation. However, the MCSA approach is mathematically complex, expensive to realize, and requires a significant amount of historical data (Niu et al., 2023).

Vibration Signature Analysis (VSA)

VSA has been practiced for the fault detection and diagnosis (FDD) of electric machines for decades. Theoretically, all faults in electric machines generate vibrations with distinctive characteristics. Therefore, sampled vibration signals can be applied to be compared with reference patterns to perform FDD. In practice, vibration analysis has been used for the detection of various mechanical faults, and some unbalanced electrical faults(Bilgin et al., 2019). Study from (Langarica et al., 2020) and (Mitra & Koley, 2023), focused and developing methods for fault detection of bearing in induction machine using fusion vibration signal and CNN. However, vibration analysis with CNN has the disadvantages of requiring a large amount of data and excessive sensors, being costly, and susceptible to errors (X. Wang et al., 2020). This has affected recent research of FDD using vibration, making it less popular.

Acoustic signature analysis is another technique used to monitor the condition of electric machines. It measures noise signals which is the vibration propagated through air near the motor's surface. It may provide information about internal processes and the motor's current condition. When a motor is working well, its noise frequency spectrum has unique base patterns. If faults develop, the frequency spectrum changes. Each part of the frequency spectrum is associated with a specific source within the motor. This technique can provide valuable information about the motor's condition.

(C. He et al., 2023) and (Shubita et al., 2023) proposed non-contact approach using acoustic signal analysis to detect bearing fault with improved cyclostationary analysis algorithm and fusion machine learning respectively. However, acoustic signal analysis is not a popular method for recent researchers due to many errors and waste noise because of the sensitivity of the microphone sensor(Glowacz et al., 2018).

Thermal Signature Analysis

Thermal signature analysis is a technique that has been frequently used as a predictive tool for electrical installations maintenance since many of the failures or installation defects lead to temperature increments in specific points or areas. However, its application to fault detection in electric machines is far less usual but several methods was developed to diagnose electric machines with thermal analysis (Glowacz & Glowacz, 2017). In this method, temperature profile data may provide extremely useful information for the detection of some faults which are not easy to be detected with currents or vibrations (Mohammed et al., 2019). In addition, this can be done in a non-invasive way, i.e., without interfering with the machine's operation(Alfredo Osornio-Rios et al., 2019). In thermal analysis, much research has been done with various techniques on diverse types of faults including rotor broken bar, bearing fault and misalignment on the effect of the induction motor parts presented by (Jeffali et al., 2019). (P. S. Kumar et al., 2021) proposed FDD of induction motor through online detection using sensor arrays in sensing schemes for detecting stator inter-turn faults. Combined with machine learning method, the few-shot lightweight SqueezeNet architecture using thermal image is designed for real-time fault detection on lightweight devices was proposed by (Siraj et al., 2024).

Table 2.5 shows a summary of methods for monitoring and modelling temperature response and diagnostic. Based on the literature review on monitoring temperature response, it can be concluded that the right tool can provide precise measurement data depending on the field of study conducted. However, there are limitations when using LPTN and FEM for more complex electric machine designs, as they require high computational usage and expertise in heat transfer and electric machine design. In the diagnostic section, common methods for detecting faults in electrical machines are discussed, but there are limitations to these methods.

Table 2.5 Summary of monitoring and modelling temperature response and diagnostic.

Author	Title	Method	Summary
	Cold Junction Compensation		
	Technique of Thermocouple		Thermocouples are widely used in
Seung et	Thermometer Using Radiation-	Monitoring	the harsh conditions due to their
al. 2022	Hardened-by-Design Voltage	(Thermocouple)	low cost, robustness, and
	Reference for Harsh Radiation		reliability.
	Environment		
	An Infrared Thermal Image Few-		The system provides non-contact,
Xu et al.	Shot Learning Method Based on	Monitoring	non-destructive inspection,
2022	•	(Thermal	offering fast and reliable
2022	CAPNet and Its Application to Induction Motor Fault Diagnosis	Image)	monitoring of induction motors
	UNIVERSITI MA	AI AVSIA DA	without interference.
Zong of	Key factors on the accuracy of	Monitoring (IR	Infrared thermometer's accuracy is
Zeng et al. 2014	measurement temperature by	Thermometer)	affected by factors like surface
	using infrared thermometer		emissivity, reflectivity.
			FEM is useful for problems
Anoop et	Thermal analysis of squirrel cage	Modelling	lacking analytical solutions,
al 2020	Induction Motor	(FEM)	especially in complex geometries,
			loadings, and materials.
	Tracking of Winding and Magnet		
Liang et al. 2022	Hotspots in SPMSMs Based on	Madallina	LPTN's offer a simplified approach
	Synergized Lumped-Parameter	Modelling	to model the thermal behaviour of
	and Sub-Domain Thermal	(LPTN)	complex system.
	Models		

Table 2.5 Continued.

Author	Title	Method	Summary
Shifat	An Effective Stator Fault		MCSA carries significant
and Hur	Diagnosis Framework of BLDC	Diagnostic	information about the precision of
2020	Motor Based on Vibration and	(MCSA)	stator winding operation, allowing
2020	Current Signals		for early detection of faults.
	Rotating angle estimation for		VASA allows for condition
Wang et	hybrid stepper motors with	Diagnostic	monitoring by non-invasive
al., 2020	application to bearing fault	(VASA)	diagnosis, early fault detection and
	diagnosis		speed variation adaptability.
Shubita	Fault Detection in Rotating		The method allows for real-time
	Machinery Based on Sound	Diagnostic	fault detection and classification in
et al.,	Signal Using Edge Machine	(ASA)	rotating machines by utilizing
2023	Learning		machine learning techniques.
	Few-Shot Lightweight		Thermal analysis allows for the
Siraj et al., 2024	SqueezeNet Architecture for	Diagnostia	detection of subtle temperature
	Induction Motor Fault Diagnosis	Diagnostic	variations indicative of faults,
	Using Limited Thermal Image	(TSA)	enabling early identification of
	Dataset		issues.

2.4 Transfer Function as Model UMPS

This subsection explains the use of transfer functions as a modelling approach in recent research papers. Following subsection covers the generalities of frequency domain models, the system identification MATLAB toolbox, and the evaluation of model precision used in choosing transfer functions as a model.

Several studies have used transfer functions as thermal models for electric machines for high accuracy, low calculation computational resource (Guo & Cai, 2023) and easy implementation(Miloudi et al., 2017). (Straka et al., 2021) have established thermal error compensation using transfer function to model the relationship between heat sources and the resulting thermal errors in machine tools, which can affect machining accuracy. Additionally, (H. Zhang, 2015) present online thermal monitoring of induction machine using transfer function, focusing on accurately calculating both average and hotspot temperature.

While (P. Zhang et al., 2010) simplified first-order transfer function to model the stator winding temperature using only three parameters as Equation 2.11. The parameters considered were T_s temperature rise, k_1 and k_2 are $Loss_1$ and $Loss_2$ which were considered constant and independent of any load change after certain amount of operating time, τ_1 is time constant and I_s^2 is the current drawn by motor.

$$T_s(t) = k_1 I_s^2 \left(1 - e^{-\frac{t}{\tau_1}} \right) + k_2$$
 2.11

The stator temperature estimation results, together with the measured average stator temperature, under the 100% load conditions are shown in Figure 2.12, respectively. The proposed thermal model is more accurate than the first-order thermal model in estimating temperature. The maximum error using the proposed model is within $3^{\circ}C$, while the first-order model can have errors as large as $25^{\circ}C$.

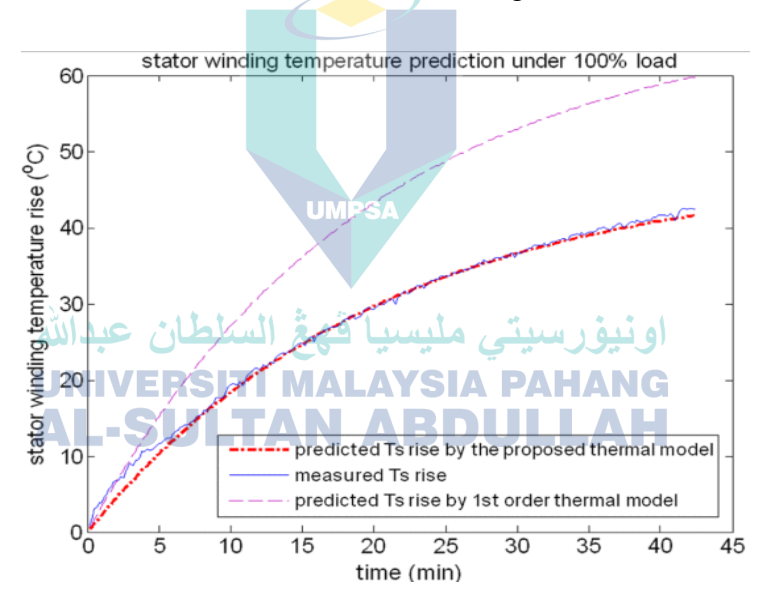


Figure 2.12 Temperature estimation under 100% load condition.

Source: Zhang et al. (2010)

2.4.1 Generalities of Frequency Domain Model

This subsection is divided into two topics: the generalities of the frequency domain model and the step response of the first-order system. A frequency-domain transfer function (Ellis, 2012) is limited to describing elements that are linear and time-invariant (LTI). However, these are severe restrictions, and no real-world system fully meets them. The criteria for linearity and time invariance are defined by the three following attributes.

Homogeneity: Assume that an input to a system r(t) generates an output c(t). For an element to be homogeneous, an input $k \times r(t)$ would have to generate an output $k \times c(t)$, for any value of k. An example of nonhomogeneous behavior is saturation, where twice as much input delivers less than twice as much output.

Superposition: Assume that an element subjected to an input $r_1(t)$ will generates the output $c_1(t)$. Further, assume that the same element subjected to input $r_2(t)$ will generate an output $c_2(t)$. Superposition requires that if the element is subjected to the input $r_1(t) + r_2(t)$, it will produce the output $c_1(t) + c_2(t)$.

Time invariance: Assume that an element has an input r(t) that generates an output c(t). Time invariance requires that $r(t-\tau)$ will generate $c(t-\tau)$ for all $\tau > 0$.

Transfer functions, which form the foundation of classical control theory, necessitate the use of LTI systems (Ellis, 2012). However, no real-world system is LTI. As an immediate solution, most control systems are designed with components that are close enough to being LTI, such that any non-LTI behaviour can be ignored or avoided. In practice, control systems are designed to minimize non-LTI behaviour, which is why components used in control systems are often more expensive than their non-control counterparts.

2.4.1.1 Nonlinear Time Invariant

Nonlinear control theory (Nise, 2014) encompasses a broader range of systems that do not adhere to the superposition principle. It is more applicable to real-world systems since all real control systems are nonlinear. These systems are frequently governed by nonlinear differential equations. The mathematical methods developed to handle them are more rigorous but less general, often only applying to specific types of systems. These methods include limit cycle theory(García-Saldaña et al., 2020), Poincaré maps (Goodman & Colombo, 2020), Lyapunov stability theory (Nguyen, 2018), and describing functions.

Figure 2.13 illustrates several examples of physical nonlinearities. Figure 2.13 (a) an electronic amplifier, for instance, is linear within a specific range but exhibits a nonlinearity known as saturation at high input voltages. A motor that does not respond to incredibly low input voltages due to frictional forces exhibits a nonlinearity known as a dead zone in Figure 2.13 (b). Gears that do not fit tightly exhibit a nonlinearity known as a backlash, where the input moves over a small range without the output responding as in Figure 2.13(c). It should be noted that the curves depicted in Figure 2.14 do not conform to the definitions of linearity over their entire range. A phase detector, used in a phase-locked loop in an FM radio receiver, is another example of a nonlinear subsystem, with an output response that is the sine of the input.

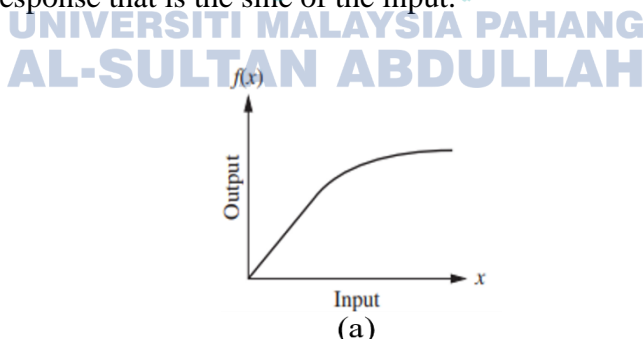


Figure 2.13 (a) Amplifier saturation. (b) Motor dead zone. (c) Backlash in gears. Source: Control Systems Engineering (2014)

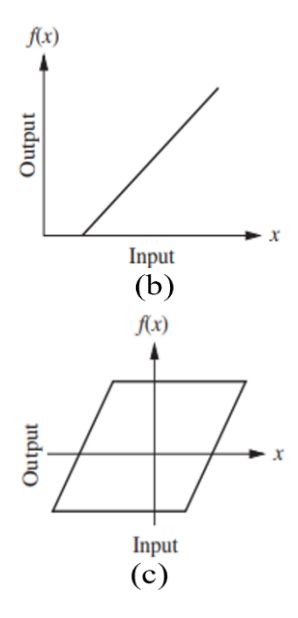


Figure 2.13 Continued.

2.4.1.2 Step Response of First Order System

Consider the first-order system shown in Figure 2.14(a). Physically, this system may represent an RC circuit, thermal system, or the like. A simplified block diagram is shown in Figure 2.14(b). The input-output relationship is given by Equation 2.12.

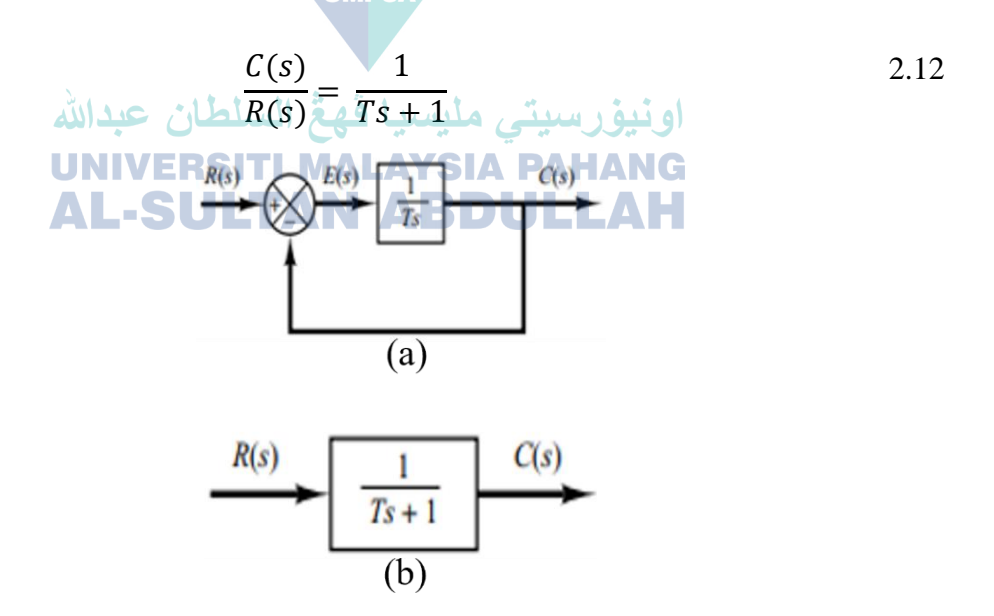


Figure 2.14 (a) Block diagram of a first-order system. (b) Simplified block diagram. Source: Modern Control Engineering (2010)

In the forthcoming analysis, system responses to unit-step, unit-ramp, and unitimpulse inputs are examined, assuming zero initial conditions. Identical transfer functions yield identical outputs for identical inputs. The mathematical response can be physically interpreted for any given system.

2.4.1.3 Unit-Step Response of First-Order Systems

Since the Laplace transform of the unit-step function is 1/s, substituting R(s) = 1/s into Equation 2.13, obtain.

$$C(s) = \frac{1}{Ts+1} \frac{1}{s}$$
 2.13

Expanding C(s) into partial fractions gives Equation 2.14:

$$C(s) = \frac{1}{s} - \frac{1}{Ts+1} = \frac{1}{s} \frac{1}{s + (\frac{1}{T})}$$
 2.14

Taking the inverse Laplace transform of Equation 2.15, obtain.

$$C(s) = 1 + e^{\frac{t}{T}}$$
 ونيور س t $t \ge 0$ يا $t \ge 0$

Equation 2.16 states that initially the output c(t) is zero and finally it becomes unity. One important characteristic of such an exponential response curve c(t) is that at t = T the value of c(t) is 0.632, or the response c(t) has reached 63.2% of its total change. This may be easily seen by substituting t = T in c(t). That is,

$$c(T) = 1 - e^{-1} = 0.632$$
 2.16

Note that the smaller the time constant T, the faster the system response as shown in Figure 2.15. Another important characteristic of the exponential response curve is that the slope of the tangent line at t = 0 is 1/T, since

$$\frac{dc}{dt}\Big|_{t=0} = \frac{1}{T}e^{-\frac{t}{T}}\Big|_{t=0} = \frac{1}{T}$$
 2.17

The output would reach the final value at t = T if it maintained its initial speed of response. From Equation 2.17, the slope of the response curve c(t) decreases monotonically from 1/T at t = 0 to zero at $t = \infty$.

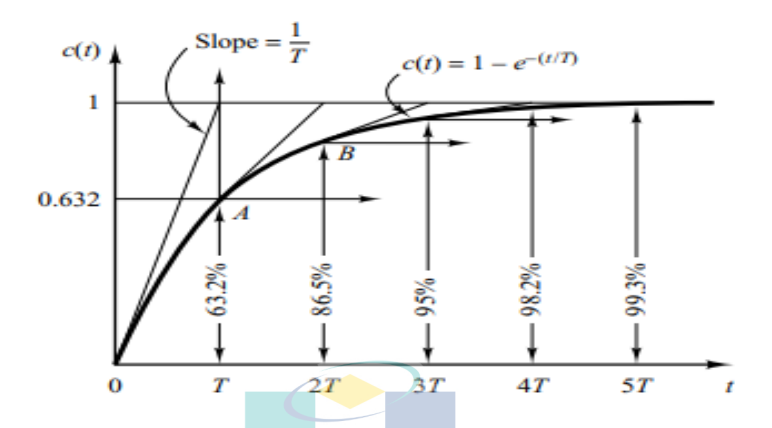


Figure 2.15 Exponential response curve.

Source: Modern Control Engineering (2010)

The exponential response curve c(t) given by Equation 2.16 is shown in Figure 2.15. In one time constant, the exponential response curve has gone from 0 to 63.2% of the final value. In two-time constants, the response reaches 86.5% of the final value. At t = 3T, 4T, and 5T, $t \ge 4T$, the response remains within 2% of the final value. As seen from Equation 2.17, the steady state is reached mathematically only after an infinite time. In practice, however, a reasonable estimate of the response time is the time the response curve needs to reach and stay within the 2% line of the final value, or four-time constants.

Many physical system responses can be approximate to this first order or higher order response. This time response is best represented by a transfer function which is easier to solve than its differential equation equivalent. Table 2.6 shows a list of references explaining system responses modelled using the transfer function and its utility in more depth. Generalities of the frequency domain model(Ellis, 2012), nonlinear time-invariant (Nise, 2014), step response first order and the unit-step response of first-order system(Ogata, 2010). To develop a transfer function, the experimental response needs to be identified first which will be explained in the next subsections.

Table 2.6 Summary of generalities of the frequency domain model.

Author	Title	Summary
Ellis 2012	The Frequency Domain	Discussing enhancing control systems using
		frequency domain analysis, illustrated by
		Bode plots and transfer functions.
Nise 2014	Nonlinearities	Nonlinear control theory is useful for real
		systems due to their inherent nonlinearity
		and specific equation requirements.
Ogata 2010	First Order System	The system's equation outlines the input-
		output relation, studying responses to inputs
		like unit-step, ramp, and impulse.
Kaloust et al.	Robust control design for nonlinear	The paper suggests a robust control method
1997	uncertain systems with an unknown	for first-order nonlinear systems with
	time-varying control direction	uncertain dynamics and varying control
		direction.

2.4.2 System Identification

This subsection provides a detailed explanation of system identification (Balakrishnan, 2002) using MATLAB's toolbox. The discussion is divided into two parts: the first part focuses on the identification of the transfer function model, while the second part provides an overview of the system identification toolbox in MATLAB. System Identification toolbox enables the estimation of mathematical models for linear and nonlinear time-invariant systems without requiring physical insights into the system. By producing equations that describe the temperature response, it allows for predicting the system's behavior in relation to new inputs. However, if the nature of the system changes, the mathematical model may no longer be valid.

For LTI model, several types of models can be estimated using the toolbox such as the transfer function model (Donjaroennon et al., 2021) which represent the relationship between the inputs and the outputs of a system using a ratio polynomial. The state space model (S. Li et al., 2022) which represent a system by a set of input, output and state variables related by first-order differential equations is also another possible model. Finally, the polynomial model (Colombo et al., 2019) which used polynomial to represent the dynamics of the system is another model option.

Meanwhile, for non LTI model, several types of models can be estimated such as the nonlinear ARX model (Bermudez et al., 2021) which represent nonlinearities in systems using dynamic nonlinear mapping objects such as wavelet networks, tree-partitioning, and sigmoid networks. Another one is the Hammerstein-Weiner model (Kwad et al., 2020) which represents an estimated static nonlinearity in an otherwise linear system. The nonlinear grey box model (Zanelli et al., 2022) which represent nonlinear system using ordinary differential or difference equations (ODEs) with unknown parameters is also an option. Lastly, the neural state space model (Kirchgässner et al., 2023) which use neural network to represent the functions that define the nonlinear state space realization of the system can also be opted.

Regarding to the listed estimation model above, and summarized in Table 2.7, the transfer function is seen as the most suitable for implementation in this study due to the relationship between input and output of speed and temperature response. Transfer functions are light to be implemented in real-time and can be quickly developed through system identification using several experimental data only. The best form of transfer function can be searched using the Identification toolbox Using system identification giving deep knowledge in explore the best form of transfer function (order) to describe the temperature response of component in a DC machine and evaluates the model precision.

Table 2.7 Summary of the model type using system identification.

Author	Title	Method	Summary
	Mathematical model		
Daniaraannan	construction of DC Motor by	Tuanafan	Transfer function used to design
Donjaroennon et al., 2021	closed-loop system	Transfer	PID controller for DC motor at
	Identification technique Using	Function	several speed response.
	Matlab/Simulink		
Li et al., 2022	An Online VSI Error		State space model utilized for
	Parameter Identification		online compensation method of
	Method for Multiphase IM	State Space	VSI nonlinearity in multiphase
	With Non-Sinusoidal Power		IM with non-sinusoidal power
	Supply		supply.

Table 2.7 Continued.

Author	Title	Method	Summary
Colombo et al., 2019	An Embedded Strategy for Online Identification of PMSM Parameters and Sensorless Control	Polynomial	Polynomial models are integral to sensorless control for PMSM by uses electrical signals to estimate the rotor position.
Bermudez et al., 2021	Model Predictive Control of Six-Phase Electric Drives including ARX Disturbance Estimator	Nonlinear ARX	An autoregressive with exogenous variable (ARX) model is introduced to estimate disturbances and improve the predictive control's accuracy
Kwad et al., 2020	A Real-Time Nonlinear Hammerstein Model for Bidirectional DC Motor Based on Multi-Layer Neural Networks	Hammerstein- Weiner	Real-time method for modelling a DC motor using the Hammerstein model and neural networks. This approach is designed for systems with one input and one output.
Zanelli et al., 2022	Continuous Control Set Nonlinear Model Predictive Control of Reluctance Synchronous Machines	Nonlinear Grey Box	Nonlinear model predictive control approach for controlling reluctance synchronous machine.
Kirchgässner et al., 2023	Thermal neural networks: Lumped-parameter thermal modeling with state-space machine learning	Neural State Space	Thermal neural networks for LPTM in electric power systems, combining heat transfer based LPTN and machine learning.

2.4.2.1 Identification of Transfer Function

Transfer function models describe the relationship between the inputs and outputs of a system using a ratio of polynomials. The model order is equal to the order of the polynomial's denominator. The roots of the denominator are referred to as the model poles, while the roots of the numerator are referred to as the model's zero. The parameters of a transfer function model are its pole, zero, and transport delays.

For a continuous response, a transfer function model can be described as Equation 2.18. Where, Y(s), U(s) and E(s) represent the Laplace transforms of the output, input, and noise, respectively. num(s) and den(s) represent the numerator and denominator of the polynomial that define the relationship between the input and the output.

$$Y(s) = \frac{num(s)}{den(s)}U(s) + E(s)$$
2.18

In continuous-time, input and transport delays are presented with an exponent term as in Equation 2.19, where τ represents the delay.

$$Y(s) = \frac{num(s)}{den(s)} e^{-S\tau} U(s) + E(s)$$
2.19

A single-input single-output (SISO) continuous transfer function has the form $G(s) = \frac{num(s)}{den(s)}$. The corresponding transfer function model can be represented as Equation 2.20.

$$Y(s) = G(s)U(s) + E(s)$$
 2.20

A multi-input multi-output transfer function contains a single-input single-output transfer function corresponding to each input-output pair in the system. For example, a continuous-transfer function model with two inputs and two output has the form as Equation 2.21 and Equation 2.22. Where, $G_{ij(s)}$ is the single-input single-output transfer function between the i^{th} output and the j^{th} input. $E_{1(s)}$ and $E_{2(s)}$ are the Laplace transforms of the noise corresponding to the two outputs.

AL-SULTAN ABDULLAH

$$Y_{1(s)} = G_{11(s)}U_{1(s)} + G_{12(s)}U_{2(s)} + E_{1(s)}$$
2.21

$$Y_{2(s)} = G_{21(s)}U_{1(s)} + G_{22(s)}U_{2(s)} + E_{2(s)}$$
2.22

2.4.2.2 MATLAB Identification Tools

System identification(Balakrishnan, 2002) is a methodology for building mathematical models of dynamic systems using measurements of the input and output signals of the system. The process of system identification requires to measure the input and output signals from the system in time or frequency domain. The selection of model structure applies an estimation method to estimate values for adjustable parameters in the candidate model structure. The model structures available are presented earlier in Table

2.7. Lastly, the toolbox evaluates the estimated model by comparing the model results with the experimental data input and provides errors of the estimated model. The subsections that follow are the steps.

Measured Data as Input in System Identification

By measuring the input and output signals from a system, system identification can estimate the values of the movable parameters in each model structure using these measured data. Time-domain input-output signals, frequency response information, time-series signals, and time-series spectra can all be used to develop the models. It is necessary to have measured data that accurately captures the dynamic behaviors of the system to create an adequate model of it. The quality of the measurement data, which in turn depends on the design of the experiment, affects how accurate the model is.

Time-domain data consists of the input and output variables of the system that are recorded at a uniform sampling interval over a period. To build a continuous time model, one need to know the intrasample behaviour of the input signals during the experiment. The input can be piecewise constant or piecewise linear between samples. Frequency-domain (Pintelon & Schoukens, 2012) data represents measurements of the system input and output variables that are recorded in the frequency domain. The frequency-domain signals are Fourier transforms of the corresponding time-domain signals. Frequency-domain data can also represent the frequency response of the system, represented by the set of complex response values over a given frequency range. The frequency response describes the outputs to sinusoidal inputs. If the input is a sine wave with frequency ω , then the output will also have the same frequency, whose amplitude is $A(\omega)$ times the input signal amplitude and a phase shift of $\Phi(\omega)$ with respect to the input signal. The frequencies response can be written as $A(\omega)e^{(i\Phi(\omega))}$.

In term of data quality requirements, data must accurately reflect the crucial system dynamics to identify the system. A good experimental plan makes sure that the correct variables are measured accurately and for long enough to capture the dynamics that are being modelled. In general, inputs for experiments need to sufficiently excite the system dynamics. One step, for instance, rarely provides sufficient excitement. Set up a data acquisition system with a good signal-to-noise ratio, measure data at the proper

sampling intervals or frequency resolution, and measure data for a long enough period to capture the significant temporal constants.

Build Models from Data

A model structure is a mathematical relationship between input and output variables that contains unknown parameters. Examples of model structures are transfer functions with adjustable pole and zero, state-space equations with unknown system matrices, and nonlinear parameterized functions. The following difference Equation 2.23 represents a simple model structure. Where a and b are adjustable parameters.

$$y(k) + ay(k-1) = bu(k)$$
 2.23

The system identification process requires choosing a model structure and applying the estimation methods to determine the numerical values of the model parameters. The following approaches can be used to choose the model structure. For a model that can reproduce measured data and is as simple as possible, various mathematical structures available in the toolbox. This modelling approach is called black-box modelling. While, for a model with specific structure, which might have derived from first principles, but do not know numerical values of its parameters. The model structure can represent as a set of equations or as a state-space system in MATLAB and estimate the values of its parameters from data. This approach is known as grey-box modelling.

$$y_{model}(t) = Gu(t) 2.24$$

The system identification toolbox software estimates model parameters by minimizing the error between the model output and the measured response. The output y_{model} of the linear model as Equation 2.24. Where G is the transfer function. To determine G, the toolbox minimizes the difference between the model output $y_{model}(t)$ and the measured output $y_{meas}(t)$. The minimization criterion is a weighted norm of the error, v(t), as Equation 2.25

$$v(t) = y_{meas}(t) - y_{model}(t)$$
 2.25

 $y_{model}(t)$ is one of the simulated response (Gu(t) of the model for a given input u(t) and predicted response of the model for a given input u(t) and past measurements of the output ($y_{meas}(t-1)$, $y_{meas}(t-2)$,...). Accordingly, the error v(t) is called the simulation error or prediction error. The estimation algorithms adjust parameters in the model structure G such that the norm of this error is as small as possible.

The configuration of the estimation algorithm configures the minimization criterion to focus the estimation on a desired frequency range, for example, to put more emphasis at lower frequencies and deemphasize higher frequency noise contributions. Also, can configure the criterion to target the intended application needs for the model, such as simulation or prediction. Specifying optimization options for iterative estimation algorithms. Most estimation algorithms in this toolbox are iterative. Configure can be an iterative estimation algorithm by specifying options, such as the optimization method and the maximum number of iterations.

Black-box Modelling

Regardless of the mathematical complexity of the model, black-box modeling (Juditsky et al., 1995) is effective for fitting the data. The toolbox offers several black-box model structures, both linear and nonlinear, that have historically helped describe dynamic systems. Depending on the flexibility, requirement to consider the dynamics, and noise in the system, these model structures range in complexity. One of these structures can be chosen, and its parameters can be computed to fit the measured response data.

Black box modeling often involves predicting the parameters of different architectures and comparing the outcomes. Start with a simple linear model structure and work your way up to more sophisticated ones. The simplest input-output polynomial model is the linear ARX model, and the state-space model can be estimated by providing the number of model states. The simplest linear black-box structures require the fewest

options to set the transfer function with a given number of poles and zero. Noniterative estimate algorithms are also used in the estimation of certain of these structures, further reducing complexity. The model order can be used to configure the model structure. Depending on the type of model chosen, different definitions of model order exist. For instance, if a transfer function representation is used, the number of poles and zero affects the model order. The model order for state-space representation matches the number of states. It may be possible to infer the model order from the data in some circumstances, such as for linear ARX and state-space model architectures.

Grey-box Modelling

In the grey box(Q. Zhang, 1997) approach, the data is used to estimate the values of the unknown parameters of the model structure. The model structure is specified by a set of differential or difference equations in MATLAB and provides some initial guess for the unknown parameters specified. In general, building grey-box models need to be creating a template model structure, configuring the model parameters with initial values and constraints (if any), and applying an estimation method to the model structure and computing the model parameter values.

Evaluation of Model Quality

اه نية رسيتي ملسيا فه أسلطان عبدالله

After estimating a model (Dennis & Schnabel, 1996), its quality can be evaluated by comparing the model response to the measured response, analyzing residuals, and analyzing the model uncertainty. The quality of a model is determined by how well it satisfies the needs of the application. Comparing the model response to the measured response involves evaluating the quality of a model by comparing its response to the measured output for the same input signal. Residual analysis is performed using system identification toolbox software to assess model quality. Residuals represent the portion of the output data not explained by the estimated model, and a good model has residuals uncorrelated with past inputs. Analyzing model uncertainty involves estimating the accuracy of nominal values within a confidence region, determined by the values of parameter uncertainties computed during estimation. The magnitude of these uncertainties provides a measure of the reliability of the model. Large uncertainties in parameters can result from unnecessarily high model orders, inadequate excitation levels

in input data, and poor signal-to-noise ratios in measured data. Which can compute and visualize the effect of parameter uncertainties on the model response in the time and frequency domains using pole-zero maps, Bode response plots, and step response plots.

Table 2.8 shows a summary of the system identification, with Lennart Ljung's book (Ljung, 1999) providing a deep theoretical and practical understanding using MATLAB. (Q. Zhang, 1997) proposed a wavelet network algorithm for nonparametric regression. The model's quality is assessed by comparing its response to actual data, examining residuals, and evaluating uncertainty, as explained by (Dennis & Schnabel, 1996). Meanwhile, (Pintelon & Schoukens, 2012) and (Juditsky et al., 1995) discussed modeling in system identification using frequency domain techniques and the mathematical foundation of nonlinear black-box models respectively.

Table 2.8 Summary of system identification.

Author	Title	Method	Summary
Lennart Ljung. 1999 Dennis et al. 1996 Pintelon et al. 2012	System identification: theory for the user (second edition) Numerical Methods for Unconstrained Optimization and Nonlinear Equations System Identification: A Frequency Domain Approach,	System Identification Model Quality LAYSIA P Frequency Domain	Building mathematical models of dynamic systems by observing input/output data. Optimization and nonlinear equation solving techniques to improve model accuracy and performance. Discuss system identification, dynamic model creation from data, focusing on frequency domain
Juditsky et al. 1995	Nonlinear black-box models in system identification: Mathematical foundations	Black-box Model	techniques versus time domain methods. Examines the math of non-parametric methods for identifying nonlinear systems, focusing on the trade-off between model adaptability and estimation error.

2.4.3 Evaluation of Model Precision

The transfer function obtained by estimating data using the MATLAB system identification toolbox can later be evaluated using the fit to estimation data, MSE, and FPE, all of which are explained in detail in this subsection.

2.4.3.1 Fit to Estimation Data

Fit to estimation data refers to how well a model fits the data used to estimate it. In MATLAB's system identification toolbox, when a model is estimated, it is done so to minimize the 1-step ahead prediction error. The fit value between the 1-step ahead predicted response of this model to measured data is then calculated. The Model Output plot shows by default the fit between the simulated response of the model and the measured data. NRMSE measure of how well the response of the model fits the estimation data and expressed as the percentage, defined as Equation 2.26. Where $y_{measured}$ is the measured output data, $y_{measured}$ is the channel-wise mean, y_{model} is simulated or predicted response of the model, governed by the focus and $\|.\|$ indicates the 2-norm of a vector.

$$FitPercent = 100 \left(1 - \frac{\parallel y_{measured} - y_{model} \parallel}{\parallel y_{measured} - y_{measured} \parallel}\right)$$
UNIVERSITI MALAYSIA PAHANG

The fit percent varies between –*Inf* (bad fit) to 100 (perfect fit). If the value is equal to zero, then the model is no better at fitting the measured data than a straight line equal to the mean of the data. Some researchers used fit estimation data for model validation such as (Anshory et al., 2020) and (Majdoubi et al., 2021) where they compare the accuracy of model with the actual data in identification parameter system of a BLDC motor. (Donjaroennon et al., 2021) on the other hand, analyze the accuracy of input-output signal and derive a mathematical equation for DC motor in a closed loop system.

2.4.3.2 Mean Square Error

The MSE tells how close a regression line is to a set of points. It does this by taking the distances from the points to the regression line and squaring them. The squaring is necessary to remove any negative signs. It also gives more weight to larger differences. It is called the MSE for finding the average of a set of errors. The lower the MSE, the better the forecast. MSE measure defined as Equation 2.27, where e(t) was the signal, whose norm is minimized for estimation, N is the number of data samples in the estimation dataset.

$$MSE = \frac{1}{N} \sum_{t=1}^{N} e^{T} (t) e(t)$$
 2.27

MSE in regression analysis is used to assess the quality of a predictor or an estimator and serves as a criterion for selecting the best possible model or estimator considering the trade-off between bias and variance. Study by (Kirchgassner et al., 2021) and (Dawood et al., 2024) use MSE as a metric for evaluating the performance of the neural network models developed for temperature prediction. While (Jing et al., 2023) validation performance of Gradient Boosting Tree model for motor rotor temperature using MSE.

2.4.3.3 Final Prediction Error AN ABDULLAH

Akaike's Final Prediction Error (Akaike, 1971) criterion provides a measure of model quality by simulating the situation where the model is tested on a different dataset. According to Akaike's theory (Akaike, 1974), the most accurate model has the smallest FPE. The fit always gets better when the model order and, consequently, the adaptability of the model structure, are increased when the same dataset is utilized for both model estimation and validation.

FPE is defined by the following Equation 2.28. Where N is the number of values in the estimation dataset, e(t) is a n-by-1 vector of prediction errors, θ_N represents the estimated parameters and d is the number of estimated parameters.

$$FPE = det\left(\frac{1}{N}\sum_{1}^{N} e(t, \hat{\theta}_{N}) \left(e(t, \hat{\theta}_{N})\right)^{T}\right) \left[\frac{1 + \frac{d}{N}}{1 - \frac{d}{N}}\right]$$
2.28

There are several studies in electric motors that employed FPE in evaluation of model for their study, such as (Mokhlis et al., 2019) and (Naung et al., 2018) who assess the quality of the identified model, ensuring it accurately represents the DC machine's dynamics.

Table 2.9 shows a summary of the evaluation of model precision. Various study used MSE and FPE to evaluate model of their research. This shows these error estimation methods were valid and reasonable to use to evaluate model precision for transfer function model.

Table 2.9 Summary of evaluation of model precision.

Author	Title	Method	Summary
Majdoubi et al., 2021	Parameters estimation of BLDC motor based on physical approach and weighted recursive least square algorithm	Fit to Estimation Data	Validation using relative error calculation between physical approach values and estimated values for estimation of parameter for BLDC.
Donjaroennon et al. 2021	Mathematical model construction of DC Motor by closed-loop system Identification technique Using Matlab/Simulink	Fit to Estimation Data	Assess the best fit value for closed- loop transfer function of mathematical model of DC motor that indicates closely matches the experimental data.
Jing et al., 2023	Gradient Boosting Decision Tree for Rotor Temperature Estimation in Permanent Magnet Synchronous Motors	MSE	Assess the prediction performance and optimize key hyperparameters of the GBDT model using MSE.

Table 2.9 Continued.

Author	Title	Method	Summary
Dawood et al. 2024	An Efficient Protection Scheme Against Single- Phasing Fault for Three- Phase Induction Motor	MSE	The MSE gauges ANN performance. It measures how well the model's predictions match the real values.
Mokhlis et al., 2019	System Identification of a DC Servo Motor Using ARX and ARMAX Models	FPE	FPE is used to assess the quality of the estimated models, specifically the ARX and ARMAX models.
Naung et al., 2018	Implementation of data driven control system of DC motor by using system identification process	FPE	FPE is a measure of how well the model predicts new data that was not used during the model estimation process.

2.5 Highlights on the Research Gap

As a summary to the literature review chapter, this paragraph emphasizes the research gaps in real-time temperature response modeling of electrical machines. As shown in Table 2.5 and discussed in the subsection monitoring, modeling temperature response and diagnostics, numerous well-known methods are commonly employed in the electrical machines field, an observation on the latest trend can be made. Recent researchers use machine learning with a fusion of other analysis methods. These methods have their benefits and drawbacks, especially in terms of existing historical data availability. Their development and validation require a certain amount of time.

In situations where it's not crucial to know the direct relationship between the motor's physical parameters (such as dimensions and materials) and the temperature, a transfer function can be utilized to depict the temperature response. Transfer functions are easy to implement in real-time and can be swiftly developed through the identification of transfer functions using only a few experimental data points.

Table 2.10 shows a summary of researchers who used these methods in real-time fault detection of electrical machines. Most of the study discuss about the fault detection of inter-turn fault and bearing fault. The MCSA method was utilized by (Ray et al., 2021) and (Avina-Corral et al., 2021), while the VSA method employed by (Langarica et al., 2020) and (Mitra & Koley, 2023). The ASA method used by (Shubita et al., 2023) and (C. He et al., 2023), whereas TSA method applied by (P. S. Kumar et al., 2021) and (Siraj et al., 2024). Lastly, machine learning method adopted by (Shih et al., 2022) and (Yatsugi et al., 2023).

Table 2.10 Summary of research gaps of real time fault detection.

Author	Title	Method	Summary
Ray et al. 2021	Skewness Scanning for Diagnosis of a Small Inter-Turn Fault in Quadcopter's Motor Based on Motor Current Signature Analysis	Motor Current Signature Analysis	Use the skewness scanning algorithm to detect the number of shorted turns in the motor by analysing the skewness of wavelet coefficients at different decomposition levels.
Avina- Corral et al. 2021	Bearing Fault Detection in Adjustable Speed Drive- Powered Induction Machine by Using Motor Current Signature Analysis and Goodness-of-Fit Tests	Motor Current Signature Analysis	The Kuiper test using MCSA demonstrated the potential for real-time operation due to their low computational complexity and quick execution time.
Langarica et al. 2020	An Industrial Internet Application for Real-Time Fault Diagnosis in Industrial Motors	Vibration Signature Analysis	Employing RBC for identifying faulty variables and using CNN for detailed vibration-related fault identification.
Mitra et al. 2023	Early and Intelligent Bearing Fault Detection Using Adaptive Superlets	Vibration Signature Analysis	The method uses ASLT for high time-frequency resolution of vibration signals and inputs the data into a 2-D-CNN to classify bearing faults.
Shubita et al. 2023	Fault Detection in Rotating Machinery Based on Sound Signal Using Edge Machine Learning	Acoustic Signature Analysis	The trained model is deployed on an edge device for local processing and real-time fault detection, eliminating the need for cloud connectivity.

Table 2.10 Continued.

Author	Title	Method	Summary		
He et al. 2023	Real-Time Fault Diagnosis of		By analyzing sound signal's spectral		
	Motor Bearing via Improved	Acoustic	correlation density and using an		
	Cyclostationary Analysis	Signature	improved cyclostationary feature		
	Implemented onto Edge	Analysis	extraction algorithm, the system can		
	Computing System		diagnose faults in real-time.		
	Stator End-Winding Thermal	Thermal	The online condition monitoring		
Kumar et	and Magnetic Sensor Arrays for		system based on HESA, which		
al. 2021	Online Stator Inter-Turn Fault	Signature	allows for real-time fault detection		
	Detection	Analysis	and localization.		
	Few-Shot Lightweight		The SqueezeNet architecture is		
C:: -4 -1	SqueezeNet Architecture for	Thermal	designed to be ultra-lightweight,		
Siraj et al.	Induction Motor Fault	Signature	making it suitable for real-time fault		
2024	Diagnosis Using Limited	Analysis	diagnosis applications on lightweight		
	Thermal Image Dataset		devices.		
	Common Diagnosis Approach				
Water at	to Three-Class Induction Motor	Maritima	The SVM algorithm was used to		
Yatsugi et	Faults Using Stator Current	Machine	classify motor faults based on the		
al. 2023	Feature and Support Vector	Learning	load current spectra and motor speed.		
	Machine	PSA			
	Machine Learning for Inter-		The CNN learned to diagnose faults		
Shih et al.	Turn Short-Circuit Fault	Machine	directly from 2-D images of data,		
2022	Diagnosis in Permanent Magnet	Learning	eliminating the need for initial		
	Synchronous Motors	ABDL	feature extraction.		

There is a gap for a new method that uses a transfer function as a baseline temperature model in real-time fault detection of electrical machines. This method is cost-effective, accurate, and doesn't necessitate a motor thermal specialist to develop. The new method, which uses the transfer function to model the temperature response of electrical machines, can be developed and studied. The baseline temperature model by transfer function will represent several critical components of electrical machines, including the brush, bearing, permanent magnet, and casing. To be developed, the input data of speed step, and the output data of temperature responses of the components will be required, which will be measured through experimental works. Further evaluation and validation of this method will be discussed in the results and discussion chapter.

CHAPTER 3

METHODOLOGY

3.1 Introduction

This chapter explains the processes for achieving the objectives outlined in the Introduction. It covers motor details, instrumentation, test setup, method development, transfer function modeling, and model validation. The entire process is summarized in Figure 3.1.

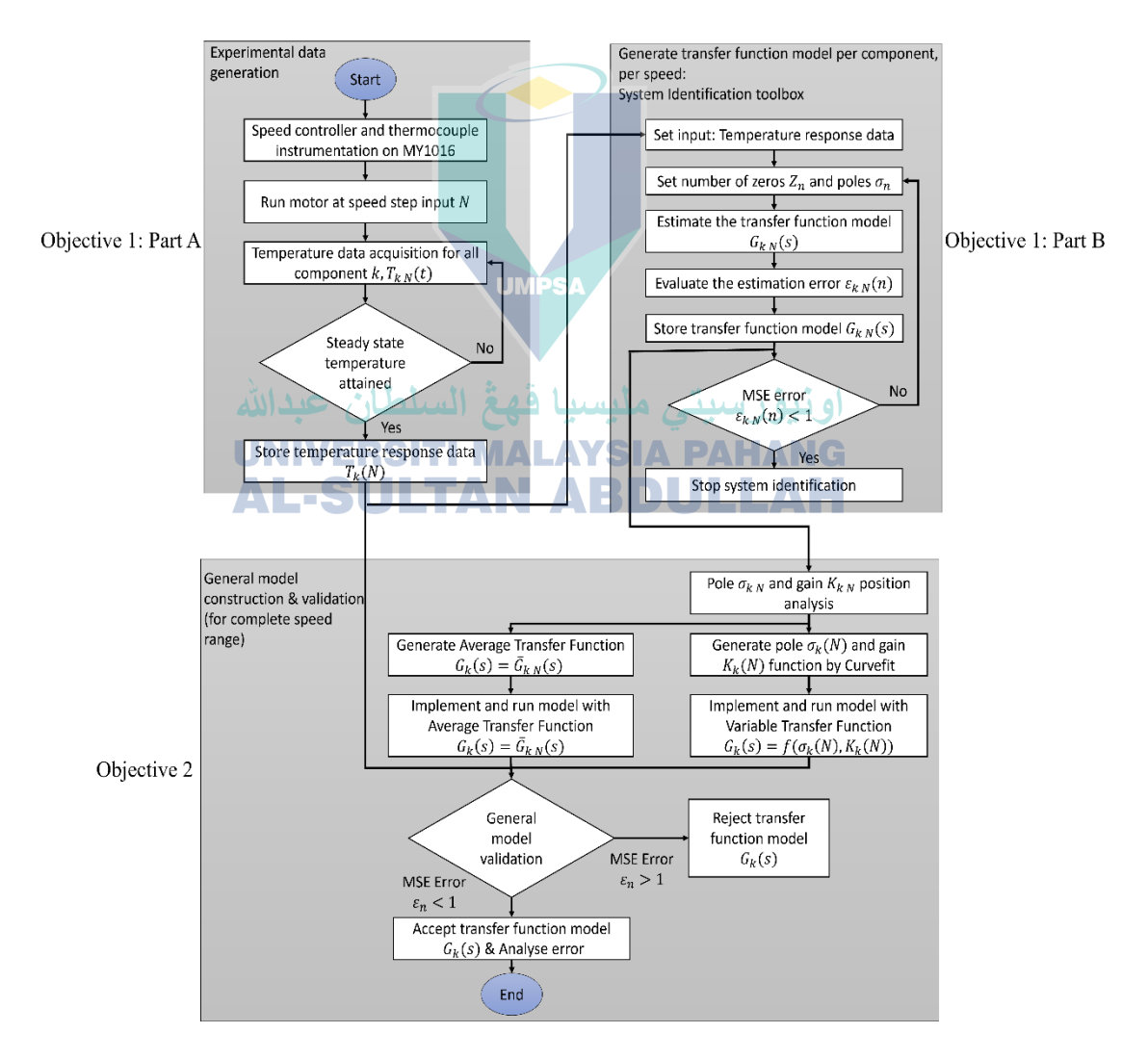


Figure 3.1 Research flow chart.

There are three (3) main stages in this research. To develop a generalized speed-dependent temperature response model, will be using the transfer function. Therefore, the research starts with temperature response data collection that will serve as input to develop our model. The temperature data at selected components were collected while the motor was running at several sample speeds. The next step is the transfer function model generation for each component at different speeds. Here the experimental data previously collected were used along with the System Identification toolbox to generate transfer functions that model the temperature response of the motor components. These speed-dependent transfer functions will be then analysed to develop a generalized transfer function model that can model the components' temperature response at any speed. Finally, the generalized model will be validated and tested for robustness by evaluating its temperature estimation errors in comparison to experimental data. The validated model will be used to demonstrate its ability to identify anomalies in faulty DC motors at the end of the study. Each step mentioned here will be detailed in the following sections of the methodology.

3.2 Objective 1 Part (A): Experimental Setup

The temperature response of MY1016 DC machines was collected with the motor operated using a programmed block diagram in Simulink for speed control and data acquisition. The DC motor was run in a continuous cycle at no load until they reached temperature equilibrium, as specified in the IEC-60034 standard for motor testing. This process was repeated at different motor speeds, starting at 20% and increasing in increments of 20% up to 100%. These speeds were calculated relative to the rated speed of the MY1016, which is 2650 rpm. The experimental data generation was conducted as shown in Figure 3.2.

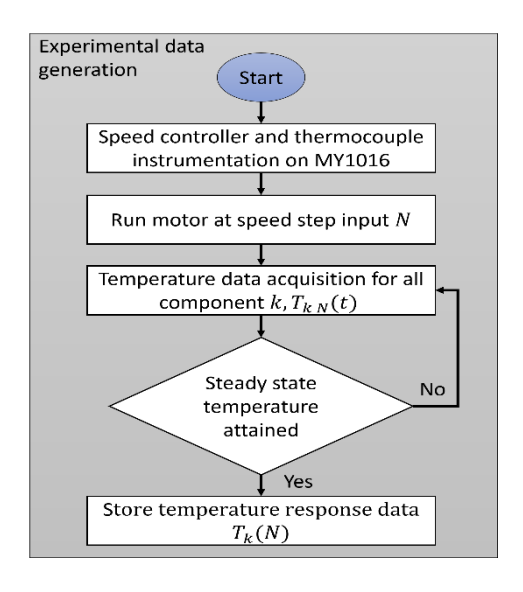


Figure 3.2 Flow chart of the experimental data generation.

Thermocouples were used to measure the temperature response at various parts of the DC machines, including the brush, bearing, permanent magnet, and casing as shown in Figure 3.3. This data was then used to identify the transfer function of the temperature response.

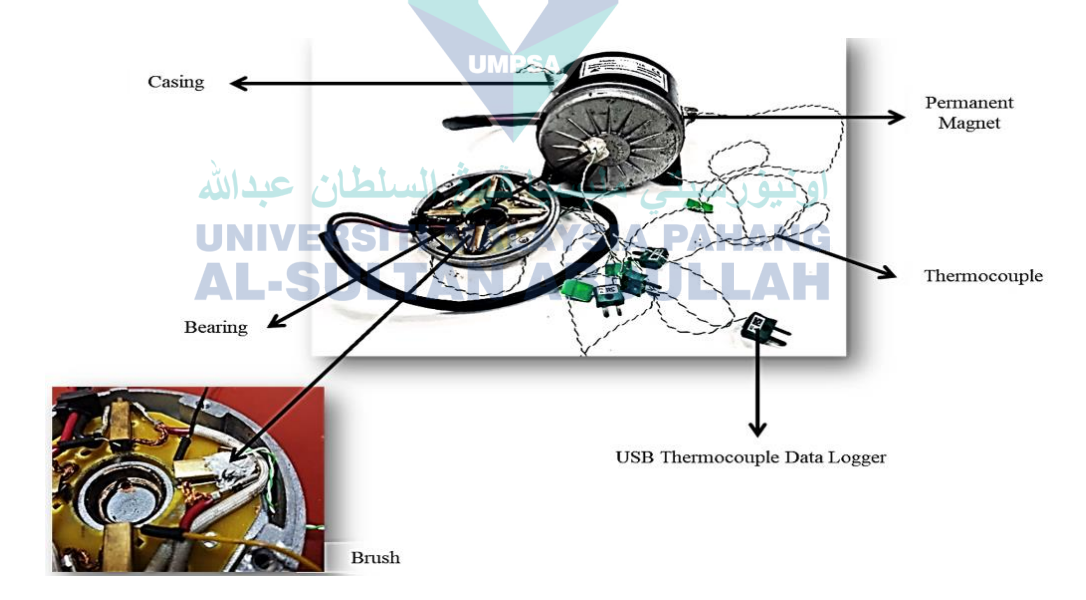


Figure 3.3 Instrumentation of DC machines.

The outputs from the thermocouples are monitored and converted to their corresponding temperatures using a Type-K thermocouple unit with an error of +/- 1.1 °C. The thermocouple measurements are taken automatically every 0.25 seconds and the data is transmitted to a host PC for storage. The current is monitored using the TP-CC80

current clamp, which allows the oscilloscope to measure electrical currents up to 80A ac/dc, with a frequency response up to 20kHz. The speed is measured using a rotary encoder with 500 pulses per revolution, which is programmed to be monitored along with the temperature. Once the DC motor is completely instrumented the motor is mounted on the top of the test bench. The temperature response is collected while the motor running in continuous running duty, following the standard duty from IEC-60034 see Appendix A.

For data acquisition in DC machine components, the readings of temperature rise, and speed constant are recorded simultaneously using the thermocouple DAQ and encoder. These values can also be monitored at the PC host. The temperature of the motor must achieve a steady state before ending the duty cycle. If the temperature continues to rise and changes, the process of data acquisition is continued until it reaches a steady state. Once all the data has been collected, it is plotted and analysed. The complete experiment setup can be seen in Figure 3.4 below. The following subsections will give more details on each component of the test setup (motor specification and characteristics, speed controller and temperature measurement program, and the faulty motor experiment)

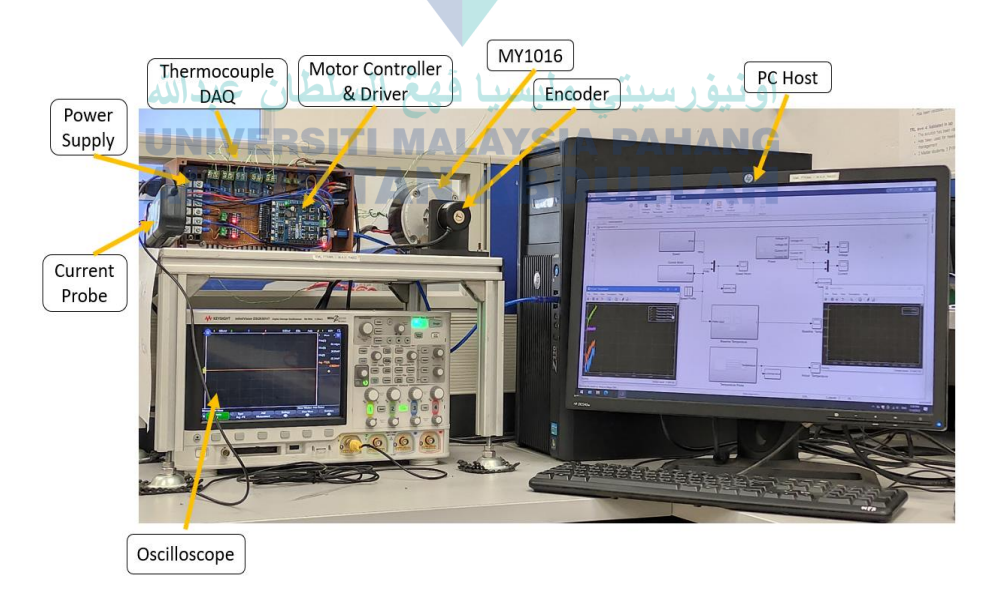


Figure 3.4 The complete experimental setup.

3.2.1 MY1016 DC Motors Specifications

The object or system in which the temperature response is going to be observed and modeled in this study is a DC motor. A small, brushed DC motor, commonly named MY1016 was chosen as a sample motor. This choice was made due to the ease of disassembly and installing the machine, as well as the accessibility to implement thermocouples on components such as the brush, bearing, permanent magnet, and casing. In addition, the structure of the machine is quite complex with irregular surface and cavity in the airgap, leading to unpredictable temperature behaviour which is interesting to observe. This complexity arises from the intricate components, the closed and rough surface on the inside, and the turbulent effect of air circulation. The specifications of the DC motor can be found in Table 3.1 below.

Table 3.1 Specification of small brushed DC machines.

Parameters		Values
Model		MY1016
Operating Voltage		24VDC
Rated Current		13.5A
Rated Speed	UMPSA	2650 Rpm
Operating Power/Output		250 W
Rated Torque No Load Current	سيا قهڠ ال	100 N-cm 2.2 A
Shaft Diameter Cable length	TAN A	SIA PAHA 12.2 mm BDULLA 25 cm
Weight		2.0 Kg
Dimension		(20*15*10) cm

This motor can be commonly found in small actuator application for light mobility such as electric bicycle and scooter. Small scale semi-industrial applications such as conveyors, extruders, fan and ventilators for food processing, and agro-industrial machinery are also frequent users of this inexpensive motor.

3.2.2 Motor No-Load Current

As previously explored in the literature review, the temperature response may come from different sources of losses and these losses can be load-dependent or speed-dependent. This study concentrates only on the second part which is the temperature that is due to speed-dependant causes. Therefore, the experimental temperature response data that is going to be collected needs to be independent of any losses due to current increases caused by a load. The experiments are then going to be at different speeds with no load. To ensure the no-load condition, the no-load current of the motor when it is running at different speed need to be characterized and verified to be at a negligible level at all speeds.

The no-load current verification is also important to ensure that the losses due to friction are minimal and negligible for the model construction. This is to demonstrate that the speed variation across the voltage range does not generate significant losses that would need to be considered. It is important to note that the model was building will serve as a baseline model, which is supposed to show the estimated temperature of a new and healthy machine without any fault or wear and tear. To verify the no-load current and losses, an experiment was conducted at different speeds by manipulating the armature voltage at various levels (which is an image of the speed of the motor). The results are plotted as shown in Figure 3.5. At the maximum voltage range, the current variation is negligible because the no-load current is less than 0.7 amp, as indicated by the orange line on the right vertical axis. This is minimal in comparison to the nominal current of 13.7 amps, as specified by the motor specification previously.



Figure 3.5 Rated current at no load speed.

When compared to the 250W nominal power, the losses at maximum speed account for only 0.1% of the nominal power of the motor. Therefore, it would not generate a significant temperature difference. Since the torque T can be computed from the equation $T = k_T \times I_0$, it can be concluded that the no-load torque of the DC motor can be considered constant across the speed range up to maximum voltage. In summary, the relationship between losses and current is proportional, and the losses of the DC machines are less than 1% of the nominal power at no-load condition. The motor is therefore without fault and suitable to be used for temperature response data generation for the development of the baseline transfer function model.

3.2.3 Speed Controller

According to the motor specifications, the MY1016 brushed DC motor is designed to be used with a power supply of 24V supply voltage and capable of delivering 20A of current. The speed of the motor is regulated using a motor driver MDD10, which is stacked on the Arduino Mega 2560 microcontroller. The switched mode power supply allows for lower losses driver while capable of delivering the criteria outlined in Table 3.1. In the meantime, a bellow coupling is used to connect a rotary encoder with 500 pulses per revolution, to the motor's shaft giving the speed feedback to the microcontroller. This setup enables the real speed of the motor to be measured and recorded. The encoder is calibrated using the motor's rated speed, which corresponds to a value of 255 pwm, allowing a reading of a maximum speed of 2650 rpm.

The microcontroller is connected in real time to MATLAB-Simulink where the speed control block diagram is implemented and monitored on a host PC. The block diagrams in Figure 3.6 shows the PWM speed control setup in Simulink. The PWM value corresponding to the supply voltage value is the input the user gives to the system. Operating in 8 bits, the maximum value of 256 would correspond to the maximum voltage supply, which corresponds also to the maximum rated speed of the motor. Any value between 0 and 256 corresponds therefore to a percentage of the nominal rated speed of the motor. The positive and negative PWM values define the rotation of the motor, clockwise and anticlockwise respectively. This process is carried out by PWM output, and pin 4 and pin 5 on the Arduino board is used for each rotation clockwise and

counterclockwise. The s-function block, Speed Acquisition is used to create the data acquisition program of the motor's actual speed for speed monitoring. The code for the microcontroller running in real-time with Simulink in detail can be referred to in Appendix B. Simulink runs in MATLAB version R2022b, and additional support packages, namely the Simulink support package for Arduino hardware and the MATLAB support package for Arduino hardware are installed to run Arduino code from Simulink.

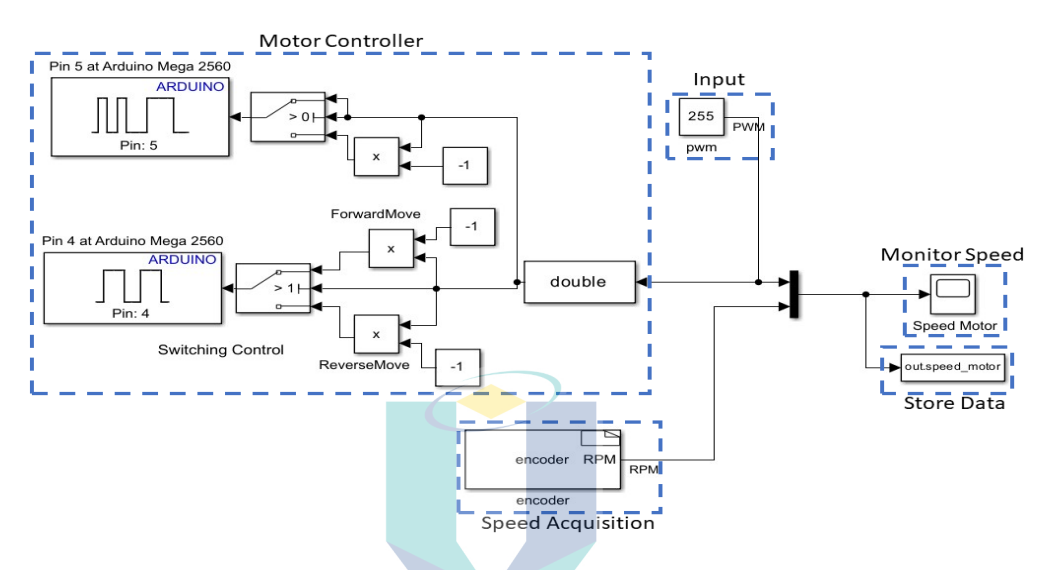


Figure 3.6 Motor controller block diagram.

3.2.4 Temperature Measurement

اونيؤر سيتي مليسيا قهة السلطان عيدالله

The type K thermocouple is used, which is composed of Chromel and Alumel conductors, and operates within a temperature range of -210 °C to 1200 °C. It features a thermocouple wire with a diameter of 0.128 mm and exhibits superior oxidation resistance compared to other types. The compact size of the thermocouple facilitates its implementation on motor components such as the brush, bearing, permanent magnet, and casing, as depicted in Figure 3.3. Despite the complex structure of the electrical machine, the installation of the thermocouple does not interrupt its normal operation. Given that the signal level of a type K thermocouple can range from 6.4 to 54.9 mV, it is essential to collect and amplify the signals using an amplifier model MAX6675. To enable detection by an Arduino Mega 2560 microcontroller, the extremely low voltage of the reference junction is increased. These attributes make the thermocouple an ideal choice for data acquisition of the temperature response of the MY1016 brushed DC machines.

To execute thermocouple data reading code within Simulink, it is necessary to develop an s-function block diagram, called Temperature Acquisition (Figure 3.6) (see Appendix B). This requirement arose from the discovery that the MAX6675 module requires a calibration delay of 0.25s before to provide an accurate temperature reading of the motor component. The thermocouple's temperature data, which is transmitted to Simulink every 0.25 seconds, is sufficiently frequent considering the inertia of temperature response. The block diagram for the temperature data acquisition is presented in Figure 3.7.

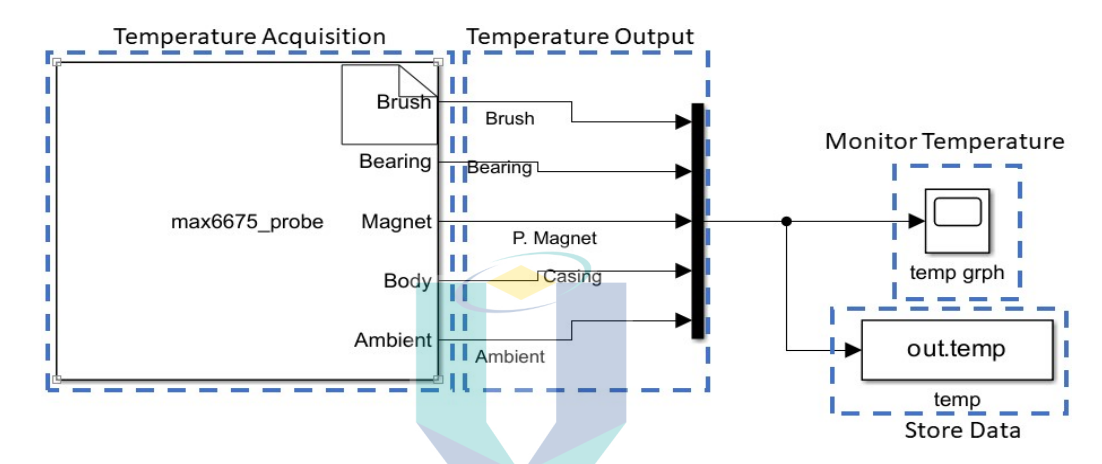


Figure 3.7 Temperature measurement block diagram.

The temperature responses were recorded until the DC machine reached a steady state. This was done at speeds speed intervals of 20%, 40%, 60%, 80%, and 100% of nominal speed. The variation in speed was achieved by adjusting the input voltage. The steady-state temperature was reached after 10,800 seconds for all components. The temperature responses for each component will be comprehensively presented and discussed in the results and discussion chapter 4.

3.2.5 Objective 3 : Fault Experiment

Once a generalized transfer function model is developed and validated, the generalized transfer function model will be tested in real conditions to evaluate its feasibility in detecting motor faults. To replicate this condition of fault, several fault conditions will be created. The faults that were chosen to be replicated are the faults that is the most frequently occurred based on our literature review previously presented in subchapter 2.3.1.

The faults replicated are degreased bearing and broken or used brush. Along with these two faults, a healthy machine will be tested along with them for comparison. This was done to validate the reliability of the equivalent model in real-world scenarios. The experiment will be conducted at varying speeds, ranging from 10% to 100% of the nominal speed, with an increment of 10% at each speed level. The temperature response was recorded until the DC machines reached a state of thermal equilibrium, which occurred approximately after 10800 seconds. The placement of the thermocouple was consistent with the setup described in the experimental setup subsection.

Figure 3.8 illustrates a DC machine bearing that has been degreased to replicate a mechanical fault due to bearing failure. The DC machines contain two bearings, located at the front and back. The bearing at the back, near the brush placement, was completely degreased. This bearing was soaked in salt water to induce corrosion due to rust and degreasing. This simulation of a degreased bearing represents a scenario where the bearing has not been adequately maintained. It is crucial to assess the extent of temperature increase in the DC machines due to the excessive friction caused by the degreased bearing.



Figure 3.8 MY1016 DC machines with degrease bearing fault.

On the other hand, Figure 3.9 illustrates the motor replicating the scenario where one of the four brushes has experienced chipping in the middle surface. This simulation is representative of a situation where the armature experiences vibrations during rotation, which subsequently impacts the brush. The chipping effect on the brush is indicative of the potential damage that can occur due to these mechanical shocks. Furthermore, it is important to evaluate the extent of temperature increase in the DC machines due to a broken brush. A broken brush can create high resistance, impeding the flow of current into the armature. This resistance can generate significant heat within the motor, leading to an excessive rise in temperature.



MY1016 DC machines with broken brush fault. Figure 3.9

The demonstration of the usage of the generalized transfer function will be done by comparing the experimental temperature responses of the faulty machines replicated above to the simulated baseline temperature response using the developed generalized model. The difference between the simulated baseline temperature and the experimental temperature and its trend will be highlighted in the results. This difference can be used as an anomaly detection tool that may signify the occurrence of a fault and should trigger a further detailed diagnostic process.

3.3 Objective 1 Part (B): Transfer Function Identification

Following data collection and generation from experimental setups explained in the previous section, the next step is to use that temperature response data to identify the transfer function that can model the thermal behavior of each component of the motor as shown in Figure 3.10. Recall that the temperature responses to a speed step input were collected at 5 different speeds, with each a ratio of the nominal speed (20% up to 100%). The temperature was recorded up to steady state temperature, for all the following components: brush, bearing, permanent magnet, and casing.

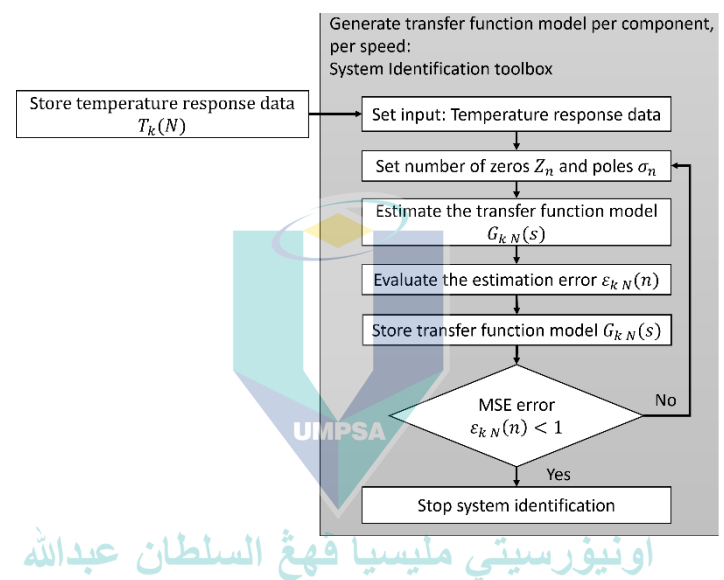


Figure 3.10 Flow chart of the development of transfer function for temperature response of the MY1016 DC machine from the experimental data.

3.3.1 System Identification Toolbox

The system identification toolbox of MATLAB is here deployed. The temperature response data was set as the output response while the pwm step speed input value was set as input and imported to the system identification Import Data section as shown in Figure 3.11. The toolbox enabled us to find the corresponding transfer function. By selecting transfer function as the model of choice, two parameters need to be set which the toolbox will try to find and fit to the experimental data. The parameters of transfer function needed are the number of zeros and poles of the transfer function. Their chosen values need to be set in the toolbox (see Appendix C for the detail).

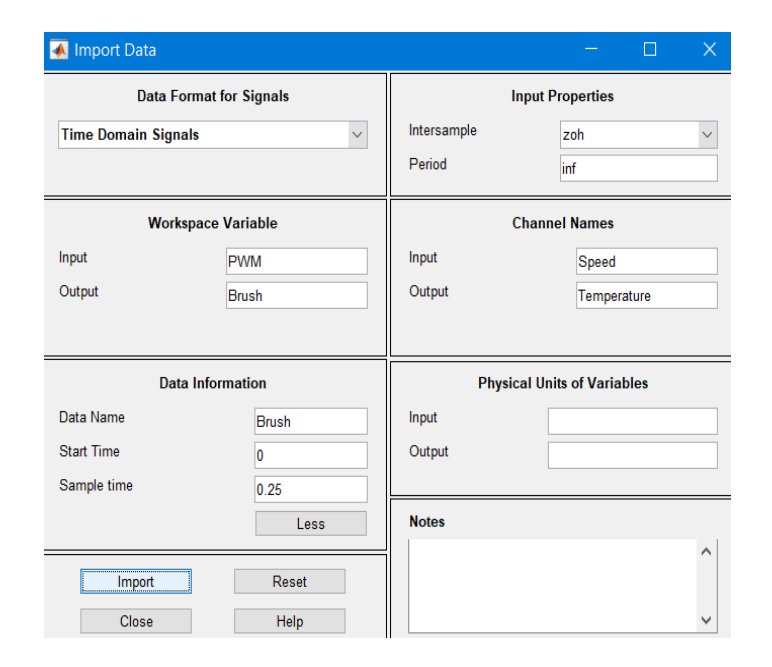


Figure 3.11 Import data step input and temperature response.

The generic form of a transfer function, considering its poles, is shown in Equation 3.1 with n the order of the system, a a real number, and the values of s solving the polynomials in the denominator are the pole.

$$G(s) = \frac{1}{a_n s^n + a_{(n-1)} s^{(n-1)} + \dots + a_0}$$

$$(a_n s^n + a_{(n-1)} s^{(n-1)} + \dots + a_0)$$

No zeros were chosen for the transfer function as a physical system can usually be modelled with no zeroes. Only gain will take place on the numerator. For the poles, different values were tested, ranging from a single pole to four poles, representing systems of the first to fourth order. The reason of limiting the pole value up to 4 is that choosing a high pole value can lead to an unstable system. The requirement that all poles need to be in the left half of the complex plane as mentioned by (Choupanzadeh & Zadehgol, 2020) and (Golnaraghi & Benjamin C.Kuo, 2017) (chapter basic control system and effects adding poles and zeros to transfer functions) will become too constraining. This can also be known as overfitting where prediction and estimation will lead to higher error as the order increases.

In theory, a temperature response resembles a first-order response. It could not be physically considered a second-order system, as there is no possibility of temperature oscillations like in mechanical or electrical systems. However, the purpose of considering higher order (2-4) is to evaluate the possibility of having a higher precision model which is purely a mathematical model that is not necessarily attached to a physical reality. Physically, it could be considered as higher-order system with a high damping value (an overdamped system). This is particularly useful for a model that is going to be used solely to monitor the baseline temperature with high precision, without considering its potential use in optimization model purposes.

Figure 3.12 illustrates the estimated transfer function result in system identification for all components and choices of poles number. The estimation transfer function was done without preprocessing and splitting experimental data. Some researchers (Al Khafaji et al., 2019; Donjaroennon et al., 2021; Naung et al., 2018; Sadeq & Wai, 2019) utilize this method in the estimation of transfer function using system identification.

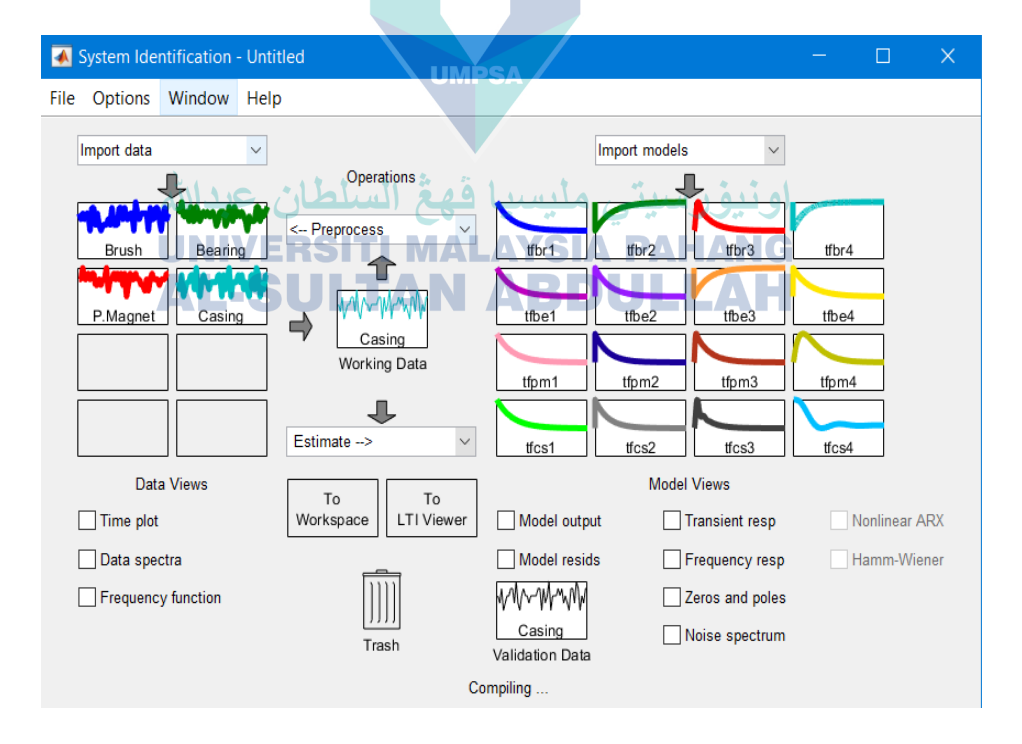


Figure 3.12 Result estimation transfer function in system identification.

The table on the right of Figure 3.12 shows the model estimation using the transfer function that the toolbox found for different motor components. By row: brush, bearing, permanent magnet, and casing, and by column:1st order, 2nd order, 3rd order, and 4th order. It also provides the equation of the transfer function in the form of polynomials as presented in Equation 3.1. These outputs are generated for one of the speed points that was tested. The identification process is repeated for all the speed points tested from 20% to 100% of the nominal speed of the motor.

These model outputs will be later presented in the result chapter. To select the best model between the order choices, the error of the model evaluated will be assessed, which will be presented in the next section.

3.3.2 Error Evaluations

The transfer function estimated by the Identification Toolbox also accounts for estimated model errors, including MSE, FPE, and the fit percentage of the estimation data. MSE is commonly used in regression analysis and other predictive modelling methods to evaluate a model's performance. The FPE criterion, developed by Akaike, measures the quality of the model by simulating the situation where the model is validated using a new dataset. A fit percentage value greater than 90%, with the smallest MSE and FPE values indicates a better model fit as it shows that the projected values are closer to the experimental value. **FRSITI MALAYSIA PAHANG**

AL-SULTAN ABDULLAH

Once the transfer function is identified, the MSE value for the model error is calculated in comparison to the experimental data (see Appendix C for the details of the error output). The transfer functions with the highest MSE are eliminated as it does not accurately represent the temperature response of the components at various speeds under no load conditions. The identified transfer function result will be shown in Table 4.2 in the result and discussion chapter later for the brush component, while the other component will be available in Appendix I. In total, for all four components tested at five different speeds, four different orders of transfer function will be tested. The most precise transfer function will later be selected to represent the component at the selected speed. The precision is evaluated by the MSE error of the identified transfer function, with error values the closest to zero.

3.4 Objective 2 : Development of Generalized Transfer Function Model

This subsection is dedicated to the discussion of the generalized transfer function as depicted in Figure 3.13. From previous section, the transfer functions of each component were identified at different speed. To be useful in real-time (by providing the information of the baseline temperature that the machine should be having at any moment), a model needs to be valid at all operating speed (from 0 to 100 percent of the nominal speed). It is therefore necessary to develop a generalized transfer function valid for all speed points. To do so, the nature of the model as the speed increases need to be first analyzed, then only a generalized model can be proposed. This would enable the implementation of a single-node thermal model for each component, which is beneficial for real-time baseline temperature monitoring.

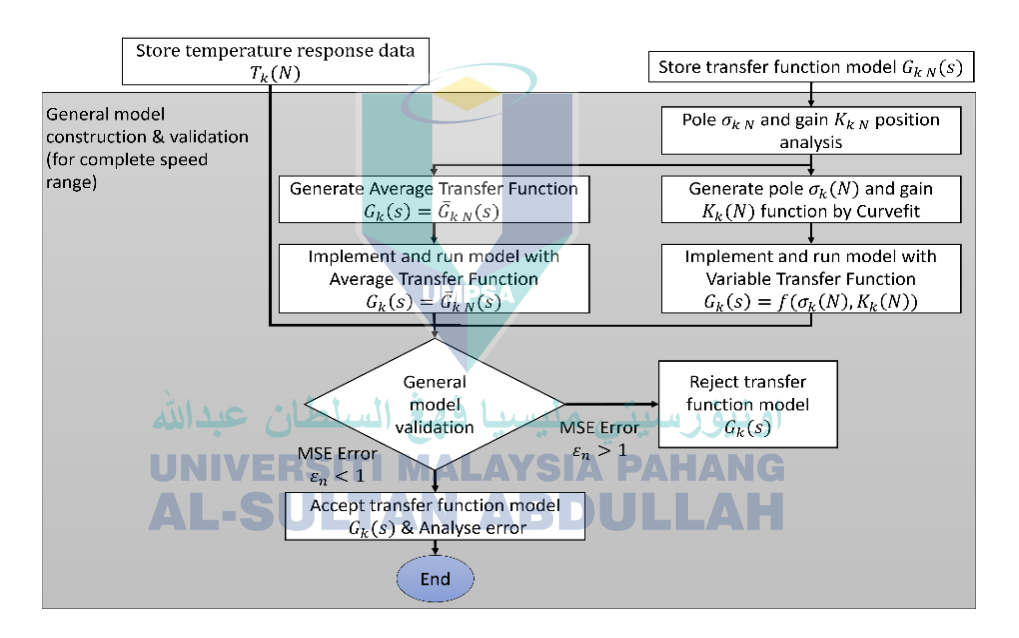


Figure 3.13 Flow chart of the development of generalized transfer function model.

3.4.1 Analysis of System Linearity

At each different speeds (20%, 40%, 60%, 80%, and 100% of the nominal rated speed), system identification produced different transfer functions. Knowing that the thermal system in which the heat is generated and transferred producing temperature is the same, which is the motor, it is understandable to assume that it should be not far from linear or LTI. However, the results showing distinct different transfer functions seem to suggest otherwise (refer to result Chapter 4.2).

An analysis of system linearity by looking at the position of the poles the transfer functions previously found was therefore done. The analysis consists of evaluating the variance of the poles' positions to evaluate their distances, leading to a conclusion of how far the system is from being able to be considered as LTI. If the system is indeed linear with minor disturbances, the pole variance value should be small. In the opposite case, if the system is non-LTI and other unidentified sources of influence change the characteristics of the system as the speed changes, then the variance value should be large.

To do linearity analysis, the identified transfer function of components such as the brush, bearing, permanent magnet, and casing for all speeds was plotted in a polezero graph in the s-plane. This allows us to observe the pole magnitude location and assess the variance between the poles. The *pzplot* function in MATLAB was used to plot the poles in the s-plane graph, where $G_{kN}(s)$ is the transfer function for the temperature response of component k at speed N as mentioned in Equation 3.2. Component k can be either brush, bearing, permanent magnet and casing.

$$Graph = pzplot(G_{kN}(s))$$
 3.2

Figure 3.14 shows a *pzplot* example for the component brush, a component where the error of model estimation done indicates that the 3rd order is the best order to represent its temperature response. All different colored points represent the transfer functions found at different speeds. All the brush poles on the complex s-plane are in the left-half plane, which means they are in the stable region. Also, a typical third-order transfer function may have one real pole and a complex conjugate pole pair, which is the necessary and sufficient condition to have real-valued coefficients in the differential equation representing the system. Notice that the brush has three poles represented as "X" for every nominal speed. The pole on the x-axis is a real pole while the y-axis represents a complex conjugate pair of poles. The poles of the brush are color-coded to represent their nominal speed. Red indicates 20%, blue indicates 40%, green indicates 60%, yellow indicates 80%, and purple indicates 100% of the nominal speed. There are no zeros represented as "O" in the s-plane graph because, as mentioned before, the identified transfer function was chosen to have no zeros for all components including the brush, bearing, permanent magnet, and casing.

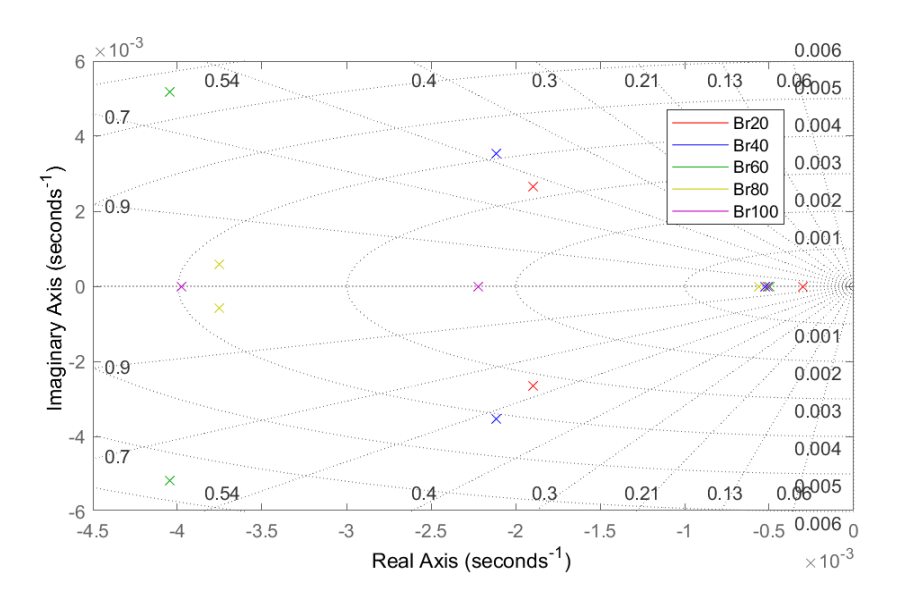


Figure 3.14 S-plane graph of pole brush.

For other components where a 1st order transfer function is sufficient, the pzmap will only have therefore one pole represented as 'X' on the s-plane. Figure 3.15 shows an example of a first-order pzmap plotted for the component bearing. Similarly, to the pzmap of a 3rd order system presented previously, all the bearing poles for the tested speeds on the complex s-plane are in the left-half plane, which means they are in the stable region and are real poles. The poles of the bearing are color-coded in the same way as well to represent their nominal speed.

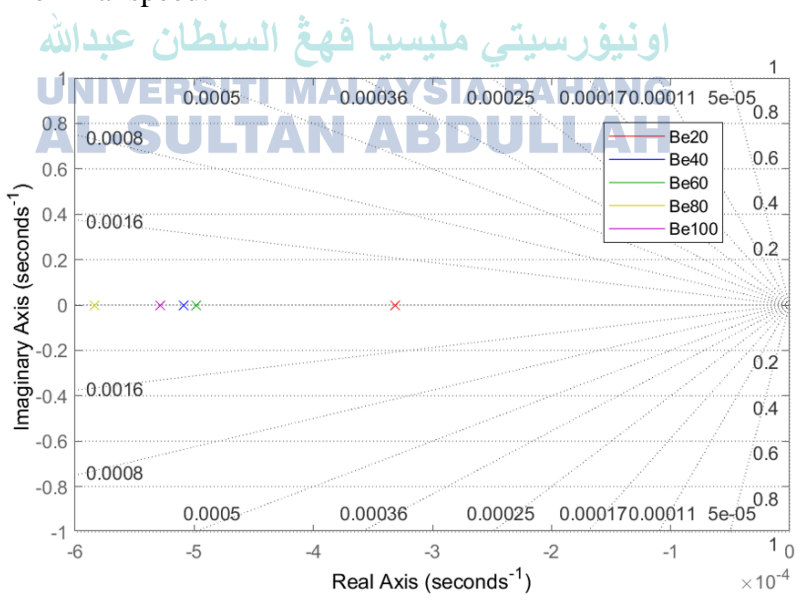


Figure 3.15 S-plane graph of pole bearing.

To perform the variance calculation of the poles values, the value of the poles needs to be retrieved from the equation of transfer function (of type Equation 3.1) that was obtained from system identification in Figure 3.12. Manually, these poles values can be retrieved from the pzmap as presented in Figure 3.14 and Figure 3.15. A more efficient and automated method was employed by extracting the pole values tf2zp function (Equation 3.3). This function extracts from the transfer function in polynomial form its values of gain, poles, and zeroes, as shown in Equation 3.4. Where Z_{kN} is zero of the transfer function for the component k at speed N, σ_{kN} is the pole of the transfer function and K_{kN} is the gain of the transfer function. On the other hand, $Z_{kN}(S)$ is the numerator coefficients of the transfer function for the component k at speed k and k an

$$[Z_{kN}, \sigma_{kN}, K_{kN}] = tf2zp(Z_{kN}(s), \sigma_{kN}(s))$$
3.3

$$G_{kN}(s) = \frac{Z_{kN}(s)}{\sigma_{kN}(s)} = K_{kN} \frac{(s - Z_{1kN})(s - Z_{2kN}) \dots (s - Z_{1kN})}{(s - \sigma_{1kN})(s - \sigma_{2kN}) \dots (s - \sigma_{3kN})}$$
3.4

This conversion step was performed for all components at all speeds using the same method. The results from converting the transfer function to the zero-pole-gain form for all components at all speeds will be shown in Table 4.4 in the result and discussion chapter. The brush transfer function has three poles, with two of them forming a complex conjugate pair of poles. For other components, the permanent magnet, bearing, and casing have a single pole for every nominal speed.

Once the values of the poles are found the variance values are deduced. It is calculated by finding the squared difference of each data point from the mean and then dividing it by the number of data points. It is used to compare the spread or dispersion of different data, in this case, the pole values. To calculate it, the mean value, $\overline{\sigma_k}$ is first calculated by Equation 3.5, then the variance, S^2 using Equation 3.6. The coefficient of deviation, CV which compares the standard deviation to the mean value of the pole are also then calculated to assess how far are the spread from the mean value of the pole

using Equation 3.7 Where $\sigma_{k N}$ is the transfer function of component k at speed N, N_{min} to N_{max} are the minimum to the maximum speed at which the transfer functions were identified, and n_N the number of speeds tested.

$$\overline{\sigma_k} = \frac{\sum_{N_{min}}^{N_{max}} \sigma_{kN}}{n_N}$$
 3.5

$$S^{2} = \frac{\sum_{N_{min}}^{N_{max}} (\sigma_{kN} - \overline{\sigma_{k}})}{n_{N}}$$
3.6

$$CV = \frac{\sqrt{S^2}}{\sigma_k}$$
 3.7

In the result chapter later, it will be explained that the analysis of the variance led to two suggestions for a generalized transfer function model: an averaged-pole model and a variable-pole model. The condition and the development of both generalized models will be explained in detail in the two following subsections.

3.4.2 Averaged-Pole Transfer Function

If the system linearity analysis revealed that the variance between the pole values of the transfer function at different speeds is small, it may suggest that the system is almost linear. The criteria for small variance is arbitrarily decided at a CV of less than 10% (CV% < 10%). In that case, it can be assumed that the temperature response across the speed range can be represented by a single transfer function that averages all previously found transfer functions.

The proposed averaged-pole transfer function method involves constructing a new transfer function. The pole of this new function equals the average of all the poles of the transfer functions at different speeds. The same process is applied to the gain value of the transfer function. The averaging of the transfer function is done in pole-zero-gain form.

Figure 3.16 illustrates the construction of the new averaged-pole transfer function for the bearing component. The pole σ_N of every speed were all summed and divided to the number of speed samples (in this case 5: 20%, 40%, 60%, 80%, and 100% of the nominal speed). The same process is also applied to the gain K_N . The process is repeated for all components of the motor.

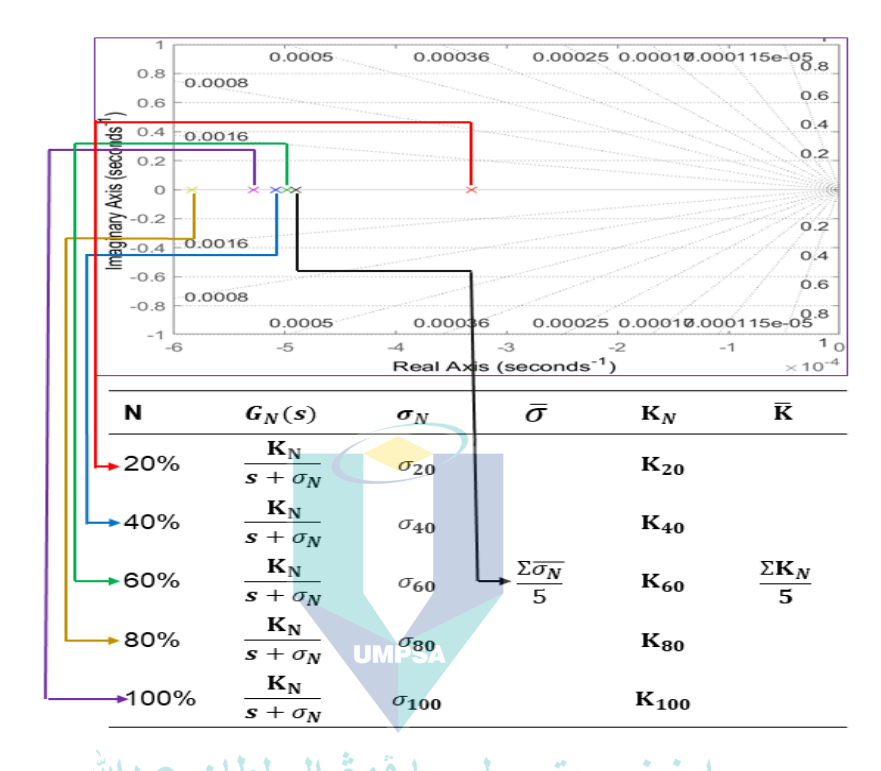


Figure 3.16 Construction of averaged-pole transfer function model.

UNIVERSITI MALAYSIA PAHANG

The averaged-pole transfer function will have the form of Equation 3.8 for components with first-order transfer function and Equation 3.9 for components with a third-order transfer function:

$$G_k(s) = \frac{\overline{K}}{s + \overline{\sigma}}$$
 3.8

$$G_k(s) = \frac{\overline{K}}{(s + \overline{\sigma_1})(s + \overline{\sigma_2})(s + \overline{\sigma_3})}$$
3.9

With $\overline{K} = \frac{\sum K_N}{5}$ the averaged gain and $\overline{\sigma} = \frac{\sum \sigma_N}{5}$ the averaged pole value. All the details of calculation for all components can be referred in Appendix E. Their results will be later presented in the chapter results and discussion in Table 4.5.

After the pole and gain were averaged, the transfer function that were in the zero-pole-gain form is converted back into polynomials form using zp2tf function in MATLAB as shown in Equation 3.10. The new averaged-pole transfer function is now in a polynomial form as shown in Equation 3.11.

$$[Z_{k,N}(s), \sigma_{k,N}(s)] = zp2tf(Z_{k,N}, \sigma_{k,N}, K_{k,N})$$
 3.10

$$G_{kN}(s) = K_{kN} \frac{(s - Z_{1kN})(s - Z_{2kN}) \dots (s - Z_{1kN})}{(s - \sigma_{1kN})(s - \sigma_{2kN}) \dots (s - \sigma_{3kN})} = \frac{Z_{kN}(s)}{\sigma_{kN}(s)}$$
3.11

Once all the averaged-pole transfer functions for each component are obtained, the temperature response of the generalized model for the whole motor can be simulated and its response will be compared to the experimental temperature response. To do so, the generalized transfer function is implemented in the Simulink control block as shown in Figure 3.17. The four blocks of transfer functions represent the averaged-pole transfer function of each component. They will be simulated with an input of step speed input determined by the PWM value, which replicates the condition of a motor operating under the continuous cycle S1 as explained in the experimental setup previously.

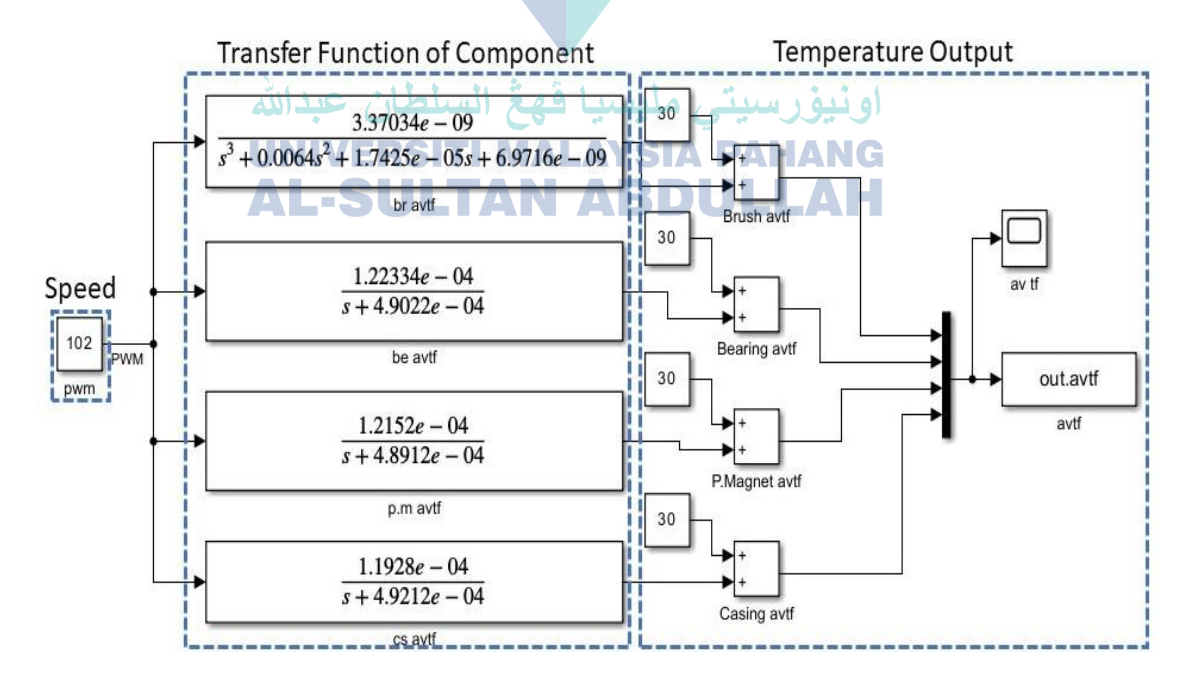


Figure 3.17 Averaged-pole transfer function block diagram.

The 'br avtf', 'be avtf', 'p.m avtf' and 'cs avtf' denote the averaged-pole transfer functions for brush, bearing, permanent magnet, and casing respectively. In the temperature output section of Figure 3.17, the output temperature responses of the transfer function are added to the ambient temperature of the experiment which is controlled at 30 °C.

The validation will be done by comparing the experimental temperature response to the simulated temperature response of the averaged-pole model at several speed points. The comparison will be done at the five speed points at which the experiments were done. Nevertheless, the model can be simulated at much higher speed resolution to have a more continuous temperature variation observation. The model will be considered valid if the maximum error between the experimental temperature and simulated temperature is less than 10 °C. This margin is arbitrarily chosen as any temperature measurement in practical application depends not only on the sensitivity and precision of the sensor element (such as the thermocouple junctions, which is usually high) but also on the attachment of the instrumentation to the component to be measured (direct surface contact, buried, thermal paste or thermal tape such as Kapton tape). This reduces the precision of measurement and increases the margin of error. Therefore, a maximum of 10 °C was chosen. The results of this comparison can be found in the results and discussion chapter 4.5.1, in Figure 4.6 and Table 4.8.

3.4.3 Variable-Pole Transfer Function ABDULLAH

In the case where the assumptions of the LTI model, where a generalized model using an averaged-pole transfer function model in the previous section fails to predict the baseline temperature within the required maximum error condition, a new generalized model needs to be developed considering that the system is non-LTI. Therefore, the poles of the systems for each component are not constant and change as the speed changes. The variation of the pole values will be considered to construct this new generalized transfer function, called the variable-pole transfer function.

In the context of real-time implementation, the speed, which is inputted via PWM voltage, will serve as the condition to alter, and adapt the value of the poles. However, the poles inferred from the prior experimental temperature data are confined to five discrete speeds. For a generalized transfer function to be valid and useful at any speed, the values of the poles are needed for all continuous values of speed input. Thus, the variation of the value of the pole regarding speed needs to be inferred by extrapolation. The solution chosen is to find an equation or function that describes the variation of poles vs speed using curve-fitting. For each component k, the pole equation will be able to output a new value of pole σ_k as the PWM speed input changes, using the function $\sigma_k = f(PWM)$ that it finds.

The curve-fitting toolbox from MATLAB is used to find these functions $\sigma_k = f(PWM)$. The curve-fitting toolbox constructs the mathematical functions by constructing a curve that has the best fit to a series of data points. The data points of input that are provided here are the pole values on the y-axis and PWM speed input on the x-axis. These are the data resulting from our previous linearity analysis. The type of curve that the toolbox can fit the data to includes polynomials and exponential equations among others. The toolbox will display the fit curve visually on the data as shown in Figure 3.16. The graphical fit result is used to examine the graph of the fits. Depending on the variation tendency of the data, the chosen fit was either a polynomial curve fitter or an exponential curve fitter. The best-fit result was chosen based on the fits having an SSE (Sum of Squared Errors) which evaluates the discrepancy between the data points and a fitted model. The value of SSE lower than 10^{-5} was chosen as criteria, as a value closer to zero indicates a better fit, as mentioned in the literature review chapter.

Specifically in Figure 3.18, it shows an example of a curve-fit done to the data of pole values for the component bearing. The five pole values for the five different speeds can be seen plotted in black dots. The blue curve is the curve that has been fitted to the input data, where an exponential equation was chosen as the curve due to its lowest SSE error (of 3.89×10^{-9}) when compared to other types of curves. In addition, the curve fitter toolbox also generates an equation, as shown in Figure 3.18 in the equation section. This equation called the pole equation is used in a function block that adapts the value of the pole of our transfer function based on input speed. The results for the pole equations for all components can be referred to in Table 4.8 in the result and discussion chapter.

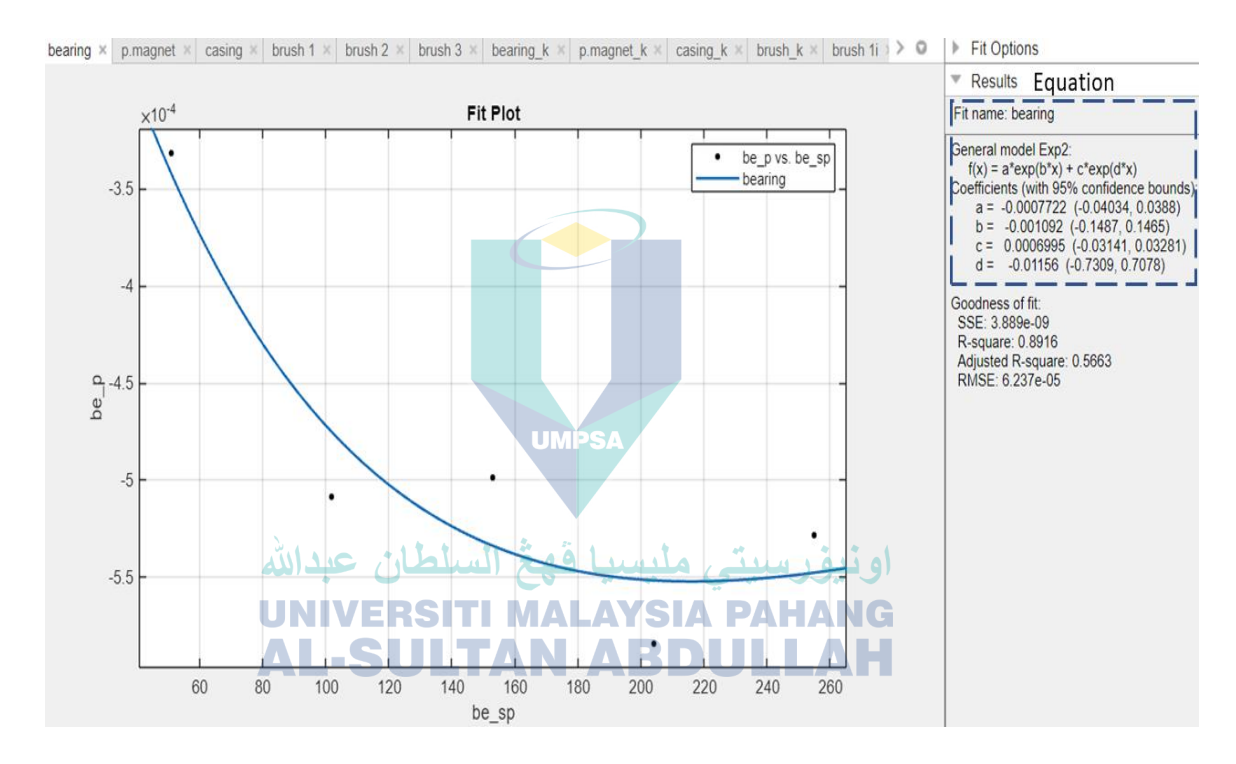


Figure 3.18 Curve-fitting of the component bearing.

Upon completion of the pole function generation, an s-block will be created in Simulink where the pole function is integrated to take the speed input and return a new pole value for each component. The implementation of this pole function is depicted in Figure 3.19 (refer to Appendix G for the code in detail). Within the pole function block, the values of the coefficients of the equations (a, b, c, and d for the exponential equation, and p1, p2, and p3 for the polynomial equation), were inserted for each component based on the results from the curve fitter. Consequently, this pole function will generate a new pole, represented as the denominator, and gain, represented as the numerator, based on the speed input. Take an example for the brush pole function, at the brush section of the output of the pole function block (Figure 3.20), there are three output ports for the denominator (annotated as br_den0 to ber_den1), with each port representing one pole respectively. This is due to the selection of the third-order transfer function for the brush component.

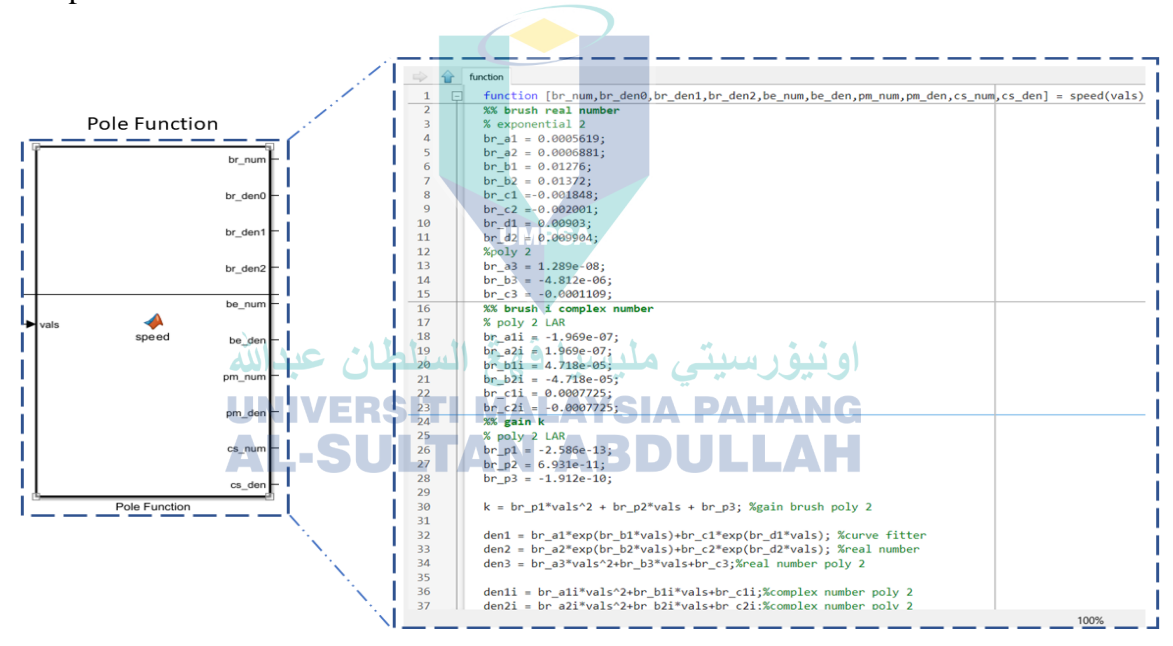


Figure 3.19 Pole function implemented in Simulink.

The variable-pole transfer function that is valid for all speed *N* will have the form of Equation 3.9 for components with first order transfer function and Equation 3.10 for components with a third-order transfer function:

$$G_k(s) = \frac{K_k(N)}{s + \sigma_k(N)}$$
3.9

$$G_k(s) = \frac{K_k(N)}{(s + \sigma_{1k}(N))(s + \sigma_{2k}(N))(s + \sigma_{3k}(N))}$$
3.10

With $K_k(N)$ is the function of gain of component k in relation to speed N and $\sigma_k(N)$ is the pole function (refer to Appendix F for the calculation details).

Figure 3.20 presents a complete variable-pole transfer function block diagram implemented in Simulink. The pole function from Figure 3.19 can be seen integrated on the left side taking the speed input and calculating the corresponding pole values. The speed part is a PWM input that can now be set to any value between the 8-bit ranges, not limited to the five different speeds in earlier experiments. The varying transfer function block (third block from the left of Figure 3.20) used in the transfer function of the component section, implements a varying coefficient based on the pole function output. b_n is the transfer function numerator coefficient while a_n is the transfer function denominator coefficient. In this model, b_n represents the gain and zero coefficients while a_n represent the poles' coefficients. In the temperature output block (on the right of Figure 3.20), the result from the transfer function is summed with an ambient temperature of 30 °C. This is done to replicate the experimental condition of a controlled ambient temperature at 30 °C.

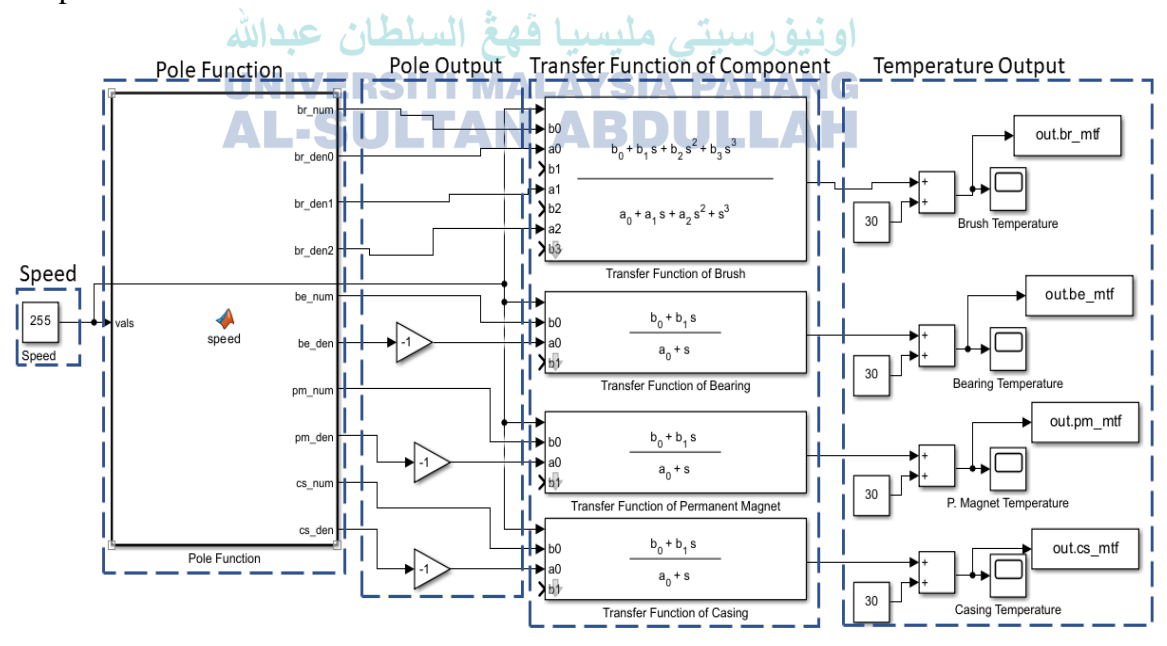


Figure 3.20 Variable-pole transfer function block diagram.

Like the averaged-pole transfer function model, the validation of this variable-pole model will be done by comparing the experimental temperature response to the simulated temperature response at several speed points. The comparison will be done at the five speed points at which the experiments were done. Nevertheless, the model can be simulated at a much higher speed resolution to have a more continuous temperature variation observation. The model will be considered valid if the maximum error between the experimental temperature and simulated temperature is less than 10 °C, considering the same reasoning mentioned in the averaged-pole model section. The result and analysis of the variable-pole transfer function model can be found in subsection 4.5.2 in the result and discussion chapter.



CHAPTER 4

RESULTS AND DISCUSSION

4.1 Introduction

This chapter presents all the results from the experiments and model simulation and validation explained in the methodology chapter. It provides a comprehensive discussion and explanation of the results from the general observation of the temperature response of the DC machine, the transfer function identified using the Identification toolbox, the system linearity analysis, and the evaluation of the averaged-pole transfer function and variable-pole transfer function developed. Finally, to demonstrate the utility of the developed transfer function model, a real-time implementation of the model to identify faults in the motor will also be presented, highlighting the ability of the model to detect anomalies in real-time.

4.2 General Observation of The Temperature Response

This section presents and discusses the temperature response data gathered from speed step input of all components at different speeds ranging from 20%, 40%, 60%, 80%, and 100% of the nominal speed. Following the execution of continuous duty cycle S1 by inputting a step speed on the MY1016 DC motor, the results of temperature rise inside the motor are extracted. The temperature reaches the steady state at 10,800 seconds for all components.

Figure 4.1 below shows DC machines operating at 60% of the nominal speed of 2650rpm for a sample observation. The same trend can be observed at other speeds, which can be referred to in Appendix H. The component that recorded the highest temperature is the brush due to the copper losses generated from the current that it conducts to the armature winding. Added to that, the friction of contact with the commutator also adds to the generated heat. In decreasing order, the highest temperature is reached next in the bearing, then the permanent magnet, and finally the casing.

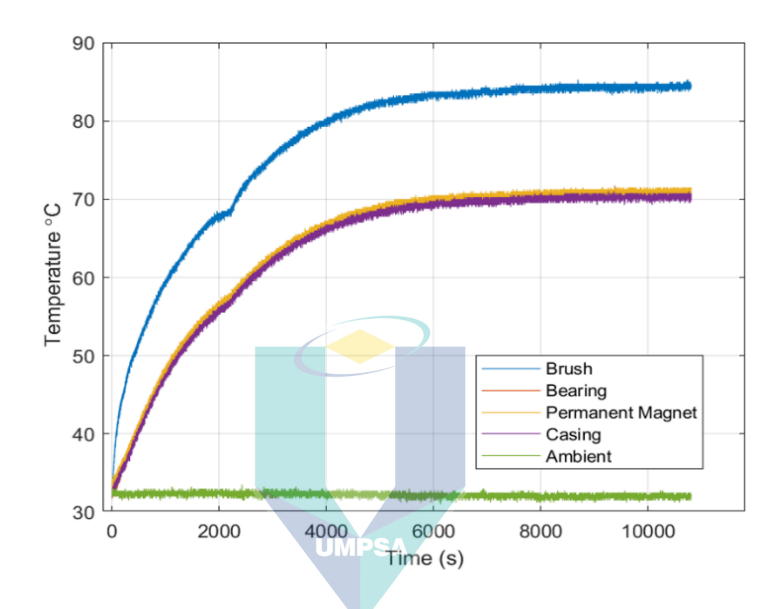


Figure 4.1 Temperature response data gathered at 60% of the nominal speed of 2650rpm. او نيور سيتي مليسيا فهغ السلطان

The summary of the steady state temperature of each component at all the speed ranges tested is shown in Table 4.1.

Table 4.1 The steady-state temperature °C of all components at different speeds.

Component	Speed (% of nominal speed of 2650rpm)				
_	20%	40%	60%	80%	100%
Brush	71.25°C	79°C	84.75°C	78.5°C	70°C
Bearing	53.5°C	65°C	71°C	67.25°C	62°C
Permanent Magnet	52.75°C	65.25°C	71.25°C	67°C	61.75°C
Casing	52°C	64.5°C	70.5°C	66.25°C	60.5°C

Subsequently, the temperature variation as the speed increases can be seen in the graph in Figure 4.2. Rotating at higher speeds generates higher temperatures across all components up until 60% of the nominal speed. After that, a decreasing trend in the temperature is observed. As explained in the experimental setup previously, the machine was running with no load, and the current was verified to be negligible, at 0.7 A maximum across the speed range. These differences in losses could not originate from the copper losses due to load, where the currents were shown to be the same.

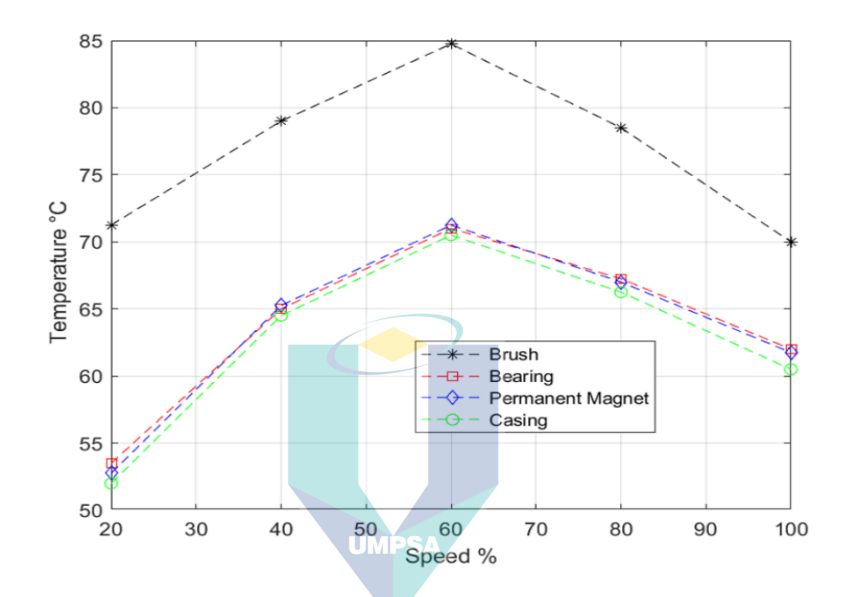


Figure 4.2 Steady state temperature of the MY1016 component at different speeds.

Therefore, the temperature rise variation can be uniquely attributed to speed-related losses (mechanical friction, windage losses). This could be explained by losses by frictions, especially mechanical due to bearing that increased with speed which is viscous in nature and demonstrated to be non-negligible here. The temperature decrease at the end may potentially be due to air circulation in the machine cavity and air gap that increases the convection rate. These losses are demonstrated to be non-linear and difficult to model across the speed range. This observation justifies the modelling of the temperature response using a transfer function to capture both transient and steady state characteristics of the complex speed-dependent temperature response. The developed transfer function later will reflect the temperature variability due to this speed variability, but not load or current. It is reminded here that the objective is to develop a model that replicates the temperature response, without necessarily being able to physically explain the phenomenon, which will be a subject for a future study.

4.3 Objective 1 : Transfer Function of Each Component at Different Speed Input

From the temperature response gathered data in the previous subsection, the system identification toolbox deduces the transfer functions for each component and the error of each model. It was used to find the best order of transfer function model to represent the temperature response of every component at each speed. Table 4.2 shows the resulting transfer function and the MSE error for the estimated model from the Identification toolbox. The results shown are only for the component brush (refer to Appendix I for the identified transfer function of other components). The best model is chosen by selecting the model with the lowest MSE error across all speeds.

Interestingly, the 1-pole model and 3-pole model consistently have the lowest MSE error for all speed ranges. To choose between these two pole numbers, an observation at the speed of 60% shows that the 3-pole model has a lower maximum MSE error than the 1-pole model, respectively at 0.41 and 0.65. This shows the pole 3-pole model is a better order for the identified transfer function model, and thus is selected to represent the temperature response of the component brush. The 2-pole and 4-pole model are too far from being precise with a huge MSE error observed.



Table 4.2 Identified transfer function for brush.

No.			
of	Speed	Transfer Function	MSE
Pole	Бресс	2.44.4.4.2.2.2.2.2.2.2.2.2.2.2.2.2.2.2.	error
		2.557e-4	
	20	$\frac{2.5576-4}{s+3.102e-4}$	0.3202
		2.454e-4	
	40	$\frac{2.16 \text{ fe}^{-1}}{\text{s} + 5.232e - 4}$	0.2475
1	60	1.781e-4	0.6504
1	00	s + 5.156e - 4	0.0504
	80	1.396e-4	0.3042
	00	s + 6.072e-4	0.00.2
	100	<u>8.05<i>e</i>-5</u>	0.1794
		s + 5.412e - 4	
	20	-6.06e-8	113.9
		$s^2 + 1.757e - 3 s + 3.557e - 14$	
	40	$\frac{4.607e - 7}{s^2 + 1.908e - 2 s + 1.377e - 10}$	24.23
		3.215 <i>e</i> -7	
2	60	$\frac{3.213e^{-7}}{s^2 + 1.806e - 2 s + 7.993e - 11}$	30.16
		3.487e-7	
	80	$s^2 + 2.883e - 2s + 8.761e - 8$	26.96
		2.001e-7	
	100	$s^2 + 2.521e - 2s + 2.512e - 9$	17.91
	20	2.671 <i>e</i> -9	0.2266
	20	$s^3 + 4.09e - 3 s^2 + 1.184e - 5 s + 3.223e - 9$	0.2366
	40	او نيو رسيت 9-4.188e فهغ السلطان عبدالله	0.1458
	40	$s^3 + 4.751e - 3 s^2 + 1.919e - 5 s + 8.929e - 9$	0.1436
3	60	7.463 <i>e</i> -9	0.4134
C		$s^3 + 8.589e - 3 s^2 + 4.725e - 5 s + 2.154e - 8$	07.10
	80	1.862e-9	0.2525
		$s^3 + 8.062e - 3 s^2 + 1.86e - 5 s + 8.066e - 9$	
	100	$\frac{6.679e - 10}{s^3 + 6707e - 3 s^2 + 1.198e - 5 s + 4.473e - 9}$	0.1533
		$8^{3} + 67076 - 38^{2} + 1.1986 - 58 + 4.4736 - 9$ - 1.997e - 13	
	20	$\frac{-1.9976-15}{s^4+1.975e-3 s^3+7.221e-6 s^2+9.242e-9 s+2.108e-22}$	89.82
		1.412e-12	
	40	$rac{1.412e - 12}{s^4 + 1.125e - 2 s^3 + 3.639e - 5 s^2 + 4.029e - 8 s + 2.204e - 12}$	4.942
		5.26e-13	
4	60	$s^4 + 7.546e - 3 s^3 + 1.794e - 5 s^2 + 1.816e - 8 s + 1.169e - 12$	6.995
		4.613 <i>e</i> -13	
	80	$s^4 + 6.91e - 3 s^3 + 1.931e - 5 s^2 + 1.752e - 8 s + 1.778e - 12$	1.67
	40-	9.125 <i>e</i> -14	
	100	$s^4 + 3.578e - 3 s^3 + 4.885e - 6 s^2 + 1.353e - 8 s + 7.936e - 21$	18.17

Table 4.3 The identified transfer function at each component and each speed.

Component	Speed	Transfer function	MSE erro
	20	2.671 <i>e</i> -9	0.2366
Brush	20	$s^3 + 4.09e - 3 s^2 + 1.184e - 5 s + 3.223e - 9$	0.2300
214011	40	4.188 <i>e</i> -9	0.1458
	40	$s^3 + 4.751e - 3 s^2 + 1.919e - 5 s + 8.929e - 9$	0.1430
	60	7.463 <i>e</i> -9	0.4134
	00	$s^3 + 8.589e - 3 s^2 + 4.725e - 5 s + 2.154e - 8$	0.4154
	80	1.862 <i>e</i> -9	0.2525
	00	$s^3 + 8.062 - 3 s^2 + 1.86e - 5 s + 8.066e - 9$	0.2323
	100	6.679 <i>e</i> -10	0.1533
	100	$s^3 + 6.707 - 3 s^2 + 1.198e - 5 s + 4.473e - 9$	0.1333
	20	1.471 <i>e</i> -4	0.1186
Permanent	20	s + 3.402e - 4	0.1100
magnet	40	1.695 <i>e</i> -4	0.1145
mugnet	10	s + 5.08e - 4	0.1110
	60	1.274 <i>e</i> -4	0.2324
		s + 4.937e - 4	0.2321
	80	1.024e-4	0.1658
		s + 5.818e-4	0.1000
	100	6.118 <i>e</i> – 5	0.1214
	100	s + 5.218e-4	0.1211
	20	<u>1.494e-4</u>	0.1271
Bearing		$u_{\text{MPS}} s + 3.315e - 4$	
	40	1.693 <i>e</i> -4	0.1185
		s + 5.086e - 4	
	60 1	$\frac{1.279e-4}{1.279e-4}$	0.2252
	200)	s + 4.985e - 4	*
	80_	ERSITI MALA\1.028e-4 AHANG	0.1599
	AL-S	$\Delta s + 5.841e - 4 \Delta -$	
	100	6.227 <i>e</i> -5	0.1198
		s + 5.284e - 4	
	20	1.437e-4	0.126
Casing		s + 3.416e-4	
	40	1.667e-4	0.1212
		s + 5.1e - 4	
	60	1.256e-4	0.2455
		s + 4.949e - 4	
	80	1.012 <i>e</i> -4	0.1644
		s + 5.872e - 4	
	100	5.921 <i>e</i> – 5	0.1395
		s + 5.269e - 4	

Summarizing for all the components, Table 4.3 below shows the transfer functions chosen for each component and the respective values of the MSE error at all the five speeds points. These transfer functions are the best fit for the experimental temperature response data that were provided. The brush is best represented by a third-order transfer function while the first-order transfer function is the best for all the other components. Despite being represented by an overdamped third-order transfer function, it is important to note that physically, the brush temperature does not have any possibility of having any oscillations or damped oscillations. The model is adopted mathematically to obtain the highest precision without having any physical connotation, as largely agreed for a surrogate model (mathematical representative model).

Despite the low MSE error values, to better visualize the fidelity of the transfer function models to replicate the temperature response of the DC machine to a step input, a plot of response of the model compared to the experimental response was done as illustrated in Figure 4.3. The example plotted here is for the component brush for a speed of 60% (The result for the component brush is chosen to be the sample for discussion due to it being the point at which the maximum temperature was attained. Sampling the result presentation using the brush at 60% will be recurring throughout this thesis). The transfer function model (red line) follows the experimental temperature response (blue line) with sufficient precision where only 2°C of steady-state error was observed.

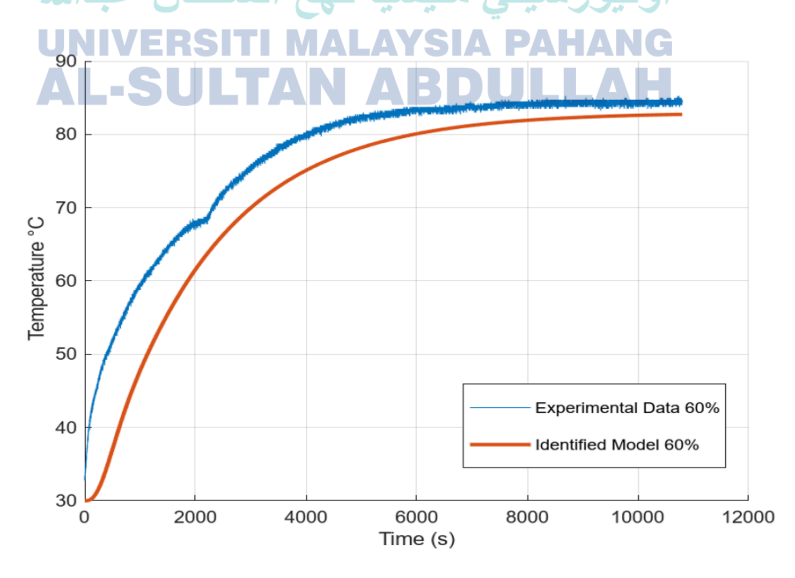


Figure 4.3 Temperature response of identified transfer function model for 60% of nominal speed for the component brush.

In transient response, a slight delay which is a characteristic of a system with an order higher than 1 can be observed. Most importantly, the steady state temperature estimated by the transfer function model is sufficiently precise. The same observation was also observed for other components, suggesting that the chosen transfer functions in Table 4.3 are valid. The graphs of the model-experiment comparisons for other components at all speeds can be found in Appendix J.

4.4 Objective 2 Part (A): Analysis of System Linearity

As mentioned in subsection 3.4.1 in the methodology chapter, the identified transfer function was plotted in the s-plane graph to observe the poles' location in the s-plane. The purpose is to evaluate their spread using the calculation of variance and coefficients of variation CV so that an assumption on the LTI nature of the system can be made.

Figures 4.4 and 4.5 illustrate the plot of the pole location on the s-plane for both the brush (representing a 3rd-order model) and the bearing (representing a 1st-order model) respectively. Notice that the brush (Figure 4.4) has three poles represented as "X" for every nominal speed. The pole on the x-axis is a real pole while the y-axis represents a complex conjugate pair of poles. The poles of the brush are color-coded to represent their nominal speed. Red indicates 20%, blue indicates 40%, green indicates 60%, yellow indicates 80%, and purple indicates 100% of the nominal speed.

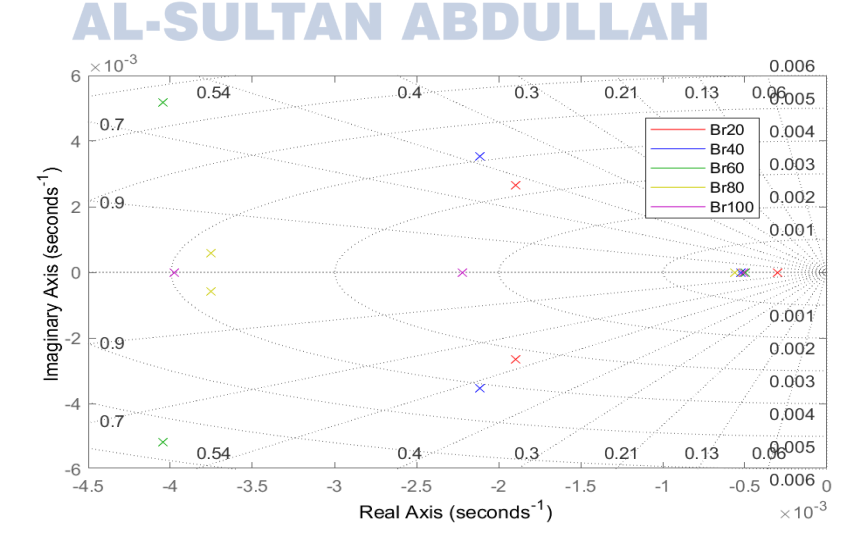


Figure 4.4 Pole-zero map plot for the brush transfer function.

Figure 4.5, on the other hand, shows only one poles for the component bearing. Similarly, to the brush, the poles of the bearing are color-coded in the same way as well to represent their nominal speed. For other components, the pzmap plot can be found in Appendix D.

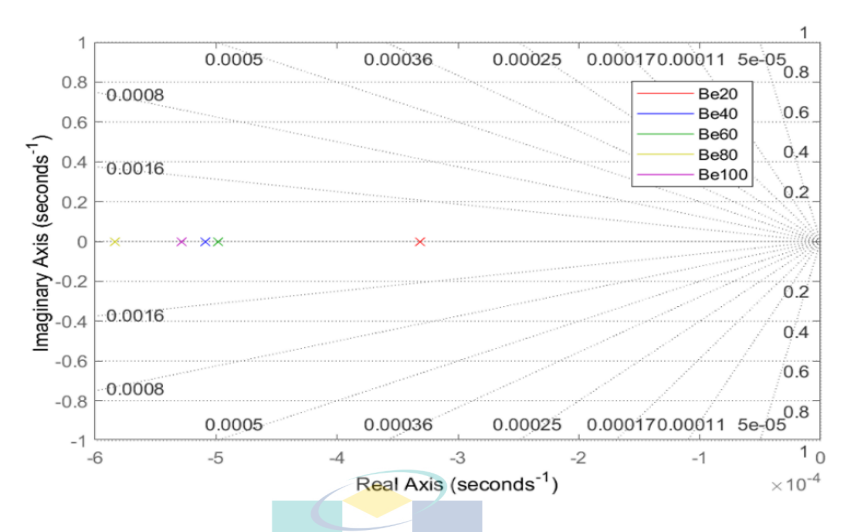


Figure 4.5 Pole-zero map plot for the bearing transfer function.

In both cases. The order of magnitude of the values of the poles are similar (in the order of 10^{-3} and 10^{-4} for brush and bearing respectively). This may allow an assumption that the poles are so close to each other that they are the same and the system is LTI. To quantitatively evaluate the spread of the poles' values, the values of the variance and coefficients of variation CV for all components at all speeds are reported in Table 4.4.

Table 4.4 Pole position, average and variance of each component.

Component	Speed		Poles				
		$\sigma_{Brush 1}$	$\sigma_{Brush \ 1}$	σ _{Brush 1}			
	20	-1.89e-3+2.67e-3i	-1.89e-3-2.67e-3i	-3.0 <i>e</i> -			
	40	-2.11e-3+3.54e-3i	-2.11e-3-3.54e-3i	- 5.26 <i>e</i> -			
	60	-4.05e-3+5.18e-3i	-4.05e-3-5.18e-3i	- 4.98 <i>e</i> -			
Brush	80	-3.75e-3+5.73e-3i	-3.75e-3-5.73e-3i	- 5.6 <i>e</i> -			
	100	-3.98 <i>e</i> -3	-2.22 <i>e</i> -3	- 5.06 <i>e</i> -			
	$\overline{\sigma_{Brush}}$	-3.2e-3+2.4e-3i	-2.8e-3-2.4e-3i	- 4.78 <i>e</i> -			
	S^2	5.68 <i>e</i> -6	5.57 <i>e</i> -6	1.04 <i>e</i> -			
	CV	0.74	0.84	0.22			
		σ_{Bea}	ring				
	20		-3.31 <i>e</i> -4				
	40		- 5.09 <i>e</i> - 4				
	60		- 4.99 <i>e</i> - 4				
Bearing	80		- 5.84 <i>e</i> - 4				
	100		- 5.28 <i>e</i> - 4				
	$\overline{\sigma_{Bearing}}$		-4.90 <i>e</i> -4				
	S^2		8.97 <i>e</i> -9				
	CV	UMPSA	0.19				
		$\sigma_{Perm.}$	Magnet				
	20		-3.4 <i>e</i> -4				
	ن عبرالله	مليسيا فهغ السلطار	5.08e-4-10				
	U ₆₀ IVE	RSITI MALAYSIA	24.94e-4 NG				
Perm.	A ₈₀ -S	ULTAN ABD	_5.82e-4				
Magnet	100		-5.22 <i>e</i> -4				
	σ _{Perm. Magnet}		-4.89 <i>e</i> -4				
	S^2		8.05 <i>e</i> –9				
	CV		0.18				

Table 4.4 Continued.

Component	Speed	Poles	
		σ_{Casing}	
	20	- 3.42 <i>e</i> - 4	
	40	- 5.10 <i>e</i> - 4	
	60	- 4.95 <i>e</i> - 4	
Casing	80	- 5.87 <i>e</i> - 4	
	100	- 5.27 <i>e</i> - 4	
	$\overline{\sigma_{Casing}}$	- 4.92 <i>e</i> - 4	
	S^2	8.31 <i>e</i> -9	
	CV	0.19	

From Table 4.4, the small values of variance should not be mistaken for a small spread. The CV value for the brush component is especially high where the maximum value of 0.84. In percentage, it is translated to 82% which means the standard deviation is at 82% equal to the mean. This level of variability is significant because it means that the data points are spread out over a wide range relative to the mean. Other CV for other components were also recorded at close to 0.2 or close to 20% which signifies a relatively high variability. From the pole variances observation for data from different speeds, it can be assumed that the thermal system of the DC machine is not linear, thus non-LTI.

From this observation, can be decided that the best way to create a generalized transfer function for the motor components that is valid for all speeds is to use a variable pole method. As a result, the following sections will discuss the results of validation of the generalized transfer function model, comparing the averaged-pole and the variable-pole transfer function.

4.5 Objective 2 Part (B): Analysis of Generalized Transfer Function

A general transfer function is a transfer function for a component that should be able to precisely model the temperature response across the speed range of the motor. This would allow the implementation of a single-node thermal model, which is beneficial for real-time baseline temperature monitoring. The transfer functions of each component at different speeds were combined into a single generalized transfer function using the two methods mentioned in the methodology chapter. In this subsection, an analysis and validation of two generalized transfer function models are presented: the averaged-pole transfer function and the variable-pole transfer function.

From the previous section 4.4, the linearity analysis of the system has shown that the system could not be considered linear. However, the validation of the averaged-pole transfer function will still be done and presented in the next subsection 4.5.1 to demonstrate the consequence of assuming the system as linear. By doing so, the incapability of the averaged-pole transfer function model in precisely estimating the baseline temperature of the motor at different speeds will be analyzed and proven. In the following subsection of 4.5.2, the validation of the variable-pole transfer function will be presented. To complete the discussion, the variable-pole transfer function is also simulated and confronted with an experimental temperature response at a much higher speed input resolution to assess its precision across the motor speed range.

Considering the many components at which the temperature was measured and modeled, the validation process presented in all the following subsections is done on the component brush. This selection is due to the brush's critical role in the operation of the DC motors. The brush is primarily responsible for conducting current and creating friction with the armature winding, which can lead to excessive temperature within the DC machines. Therefore, its performance and behavior have a significant impact on the overall efficiency and state of health of the motor. The validation data for other components presented as a graph comparing the model output and experimental temperature response can be found in their respective appendix that will be mentioned in each subsection.

4.5.1 Averaged-Pole Transfer Function

Table 4.5 shows each component's averaged-pole transfer function deduced from the methodology employed in chapter 3.4.2. The brush is represented by a third order transfer function while other components are represented by a first order transfer function. The values of the averaged-pole transfer function were implemented in the Simulink block diagram to simulate the baseline temperature response of the electrical motor using the averaged-pole transfer function model.

Table 4.5 Averaged-pole transfer function of each component.

Component	Averaged-Pole Transfer Function				
Brush	$\frac{3.37e - 9}{s^3 + 6.4e - 3s^2 + 1.74e - 5s + 6.97e - 9}$				
Bearing	$\frac{1.22e - 4}{s + 4.90e - 4}$				
Permanent Magnet	$\frac{1.21e - 4}{s + 4.89e - 4}$				
Casing	$\frac{1.19e - 4}{s + 4.92e - 4}$				

The validation of the averaged-pole transfer function model will assess both the steady state and the transient temperature response. Figure 4.4 shows the comparison at steady-state temperature between the experimental data and the averaged-pole transfer function model response for the brush (refer to Appendix K for other components). The comparisons were done for the speed points recorded during experiments which are at 20%, 40%, 60%, 80%, and 100% of the nominal speed. The blue line represents the experimental data while the black line represents the response of the averaged-pole transfer function. Also plotted are the temperature differences between the experimental data and the averaged-pole transfer function model in red.

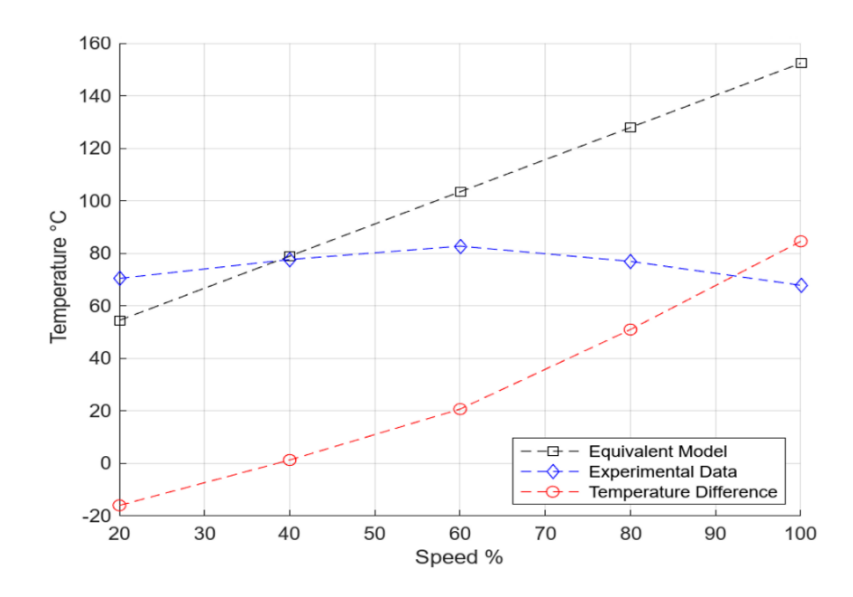


Figure 4.4 Comparison between averaged-pole transfer function vs. experimental temperature response at steady state temperature (brush).

In a steady state, it is noticeable that the temperature difference initially starts from a negative value. As the speed increases, the temperature difference also increases. At 40% speed, the temperature difference in temperature estimation is zero, indicating that the transfer function's estimation is accurate at this speed. It's because the averagedpole transfer function for the brush part as stated in Table 4.5 and the identified transfer function for the brush at 40% as stated in Table 4.3 are almost the same. With a slight difference of 0.8e-9 for the numerator and $1.6e-3s^2$, 0.1e-5s, 1.9e-9 for the denominators' poles. However, as the speed increases beyond 40%, up to 100%, the temperature difference shows an increasing trend, with the transfer function overestimating the temperature by almost 20 °C. This is in line with the characteristic of a transfer function which is LTI, thus an increasing input speed generates an increasing estimated temperature output. Having the experimental data that decreases at the speed beyond 60%, the averaged-transfer function estimation diverged away from the experimental temperature. To sum up, when the speed is less than 40%, the averagedpole transfer function tends to underestimate the temperature. Conversely, when the speed exceeds 40%, the averaged-pole transfer function overestimates the temperature.

The reason this happen due to averaging different transfer function model into single-node model led to loss of information. Whereas each individual speed-specific model can capture specific dynamics at the specific operating speed. This confirms the linearity analysis conclusion that was made in 4.4 previously.

For all the components, the difference of temperature between experimental data and averaged-pole transfer function model at steady state at different speed are summarized in Table 4.6 and plotted as a bar chart in Figure 4.5 for a visual comparison. Among all components, the brush exhibits the most significant discrepancy, with a temperature difference of approximately 84 °C between the averaged-pole transfer function model and the experimental data. The temperature difference from the equivalent model for the brush component increases as the speed increases, like an LTI system is expected to behave.

Table 4.6 The temperature difference °C of averaged-pole transfer function at steady state of all component at different speed.

Component	S	Speed (% c	of nominal speed of	f 2650rp	om)
	20%	40%	60%	80%	100%
Brush	-15°C UM	PSA1°C	20°C	50°C	84°C
Bearing	-9°C	-8°C	-1°C	14°C	33°C
Permanent Magnet	-8°C	-8°C	-1°C	14°C	33°C
Casing Lasing	-8°C	-8°C	اونيۋى _{1°1} ييتي ه	14°C	32°C

AL-SULTAN ABDULLAH

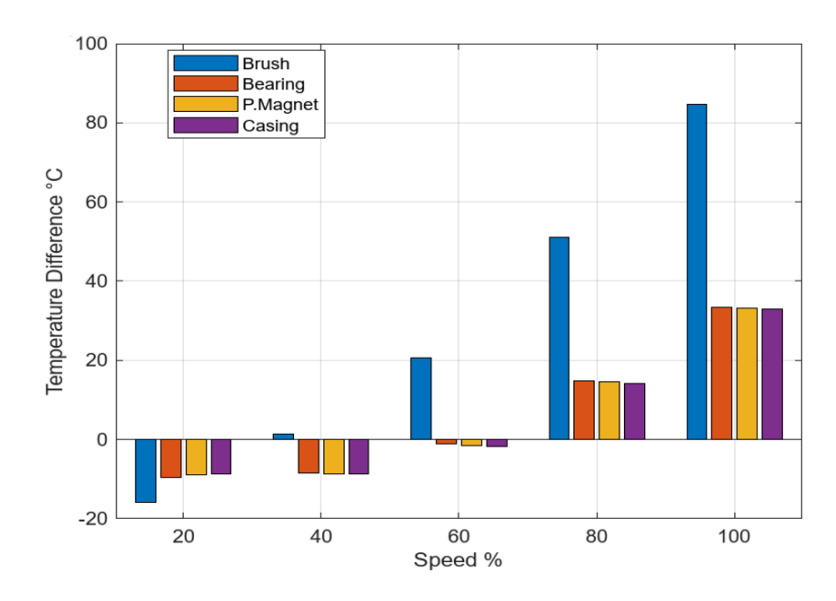


Figure 4.5 Temperature difference between experimental and averaged-pole transfer function model at steady state for all components.

In contrast, for the components such as the bearing, permanent magnet, and casing, the averaged-pole transfer function model underestimates the temperature at a lower difference of around 8 °C from 20% up to 40% of the nominal speed. At 60% of the nominal speed, the averaged-pole transfer function model accurately estimates the steady-state temperature with an error of only 1 °C for all components, unlike the brush which is precise at 40%. In the same way as the brush for a speed beyond 60%, the equivalent model overestimates the temperature as the speed increases.

UNIVERSITI MALAYSIA PAHANG

The errors of temperature estimation in terms of percentage are also reported in Table 4.7 below. With these errors in steady-state, this indicates that the averaged-pole transfer function model which is LTI cannot replicate the thermal response of the motor which the system is non-linear.

Table 4.7 Steady-state temperature estimation error from Figure 4.5 in percentage.

Component	Speed (% of nominal speed of 2650rpm)							
	20%	40%	60%	80%	100%			
Brush	-22.7%	1.7%	25%	66.3%	124.7%			
Bearing	-18.5%	-13.3%	-1.6%	22.5%	55.7%			
Permanent Magnet	-17.3%	-13.6%	-2.1%	22.2%	55.6%			
Casing	-16.9%	-13.6%	-2.5%	21.7%	56.2%			

Moving on to the validation in the transient phase, Figure 4.6 shows the transient state temperature comparison done at the time constant ($\tau = 2160$ seconds) for the component brush (The comparison graph for other components can be found in Appendix L). The blue line represents the experimental data while the black line represents the response of the averaged-pole transfer function. Also plotted are the temperature differences between the experimental data and the averaged-pole transfer function model in red.

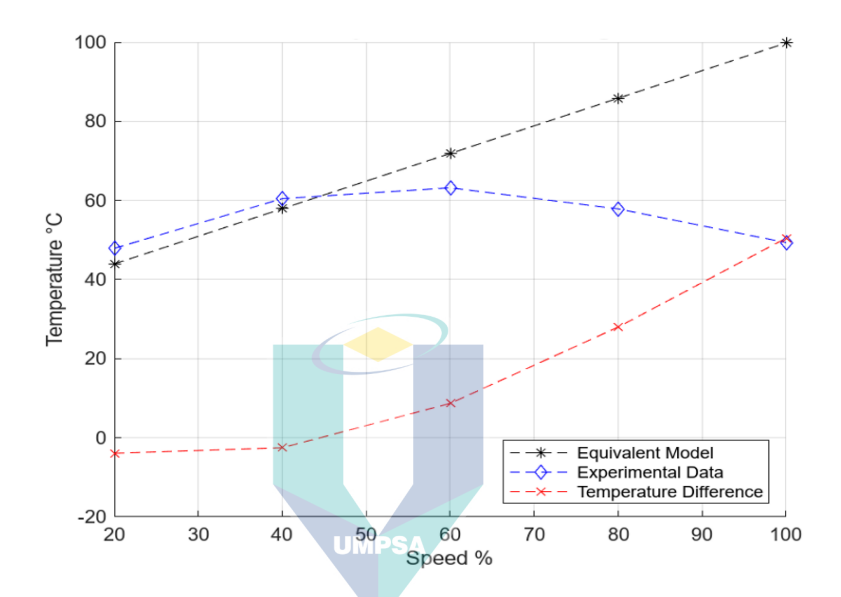


Figure 4.6 Comparison between averaged-pole transfer function vs. experimental temperature response at transient temperature (brush).

Upon closer inspection, the comparison conducted during the transient phase reveals that the averaged-pole transfer function model underestimates the temperature at the initial condition at approximately 3 °C lower until it reaches 40% of the nominal speed. As the speed increases, the model overestimates the temperature, reaching a discrepancy of nearly 20 °C when operating at 100% of the nominal speed. This observation in transient state response is like what has been observed in the steady state previously.

The summary of the temperature difference between experimental data and averaged-pole transfer function model simulation at the transient state of each component at different speeds is shown in Table 4.8 and plotted as a bar chart in Figure 4.7 for a visual comparison.

Table 4.8 The temperature difference °C of the averaged-pole transfer function at the transient state of all components at different speeds.

Component	Speed (% of nominal speed of 2650rpm)						
	20%	40%	60%	80%	100%		
Brush	-3°C	-2°C	8°C	27°C	50°C		
Bearing	-3°C	-6°C	-1°C	7°C	21°C		
Permanent Magnet	-14°C	-6°C	-1°C	7°C	21°C		
Casing	-3°C	-6°C	-1°C	7°C	21°C		

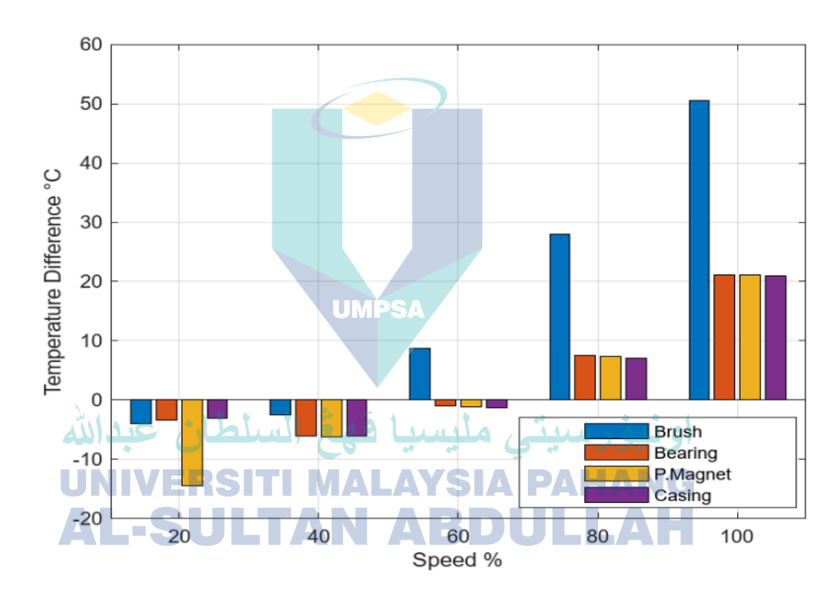


Figure 4.7 Temperature difference between experimental data and averaged-pole transfer function model at transient state for all components.

As depicted in Figure 4.7, the temperature difference between experimental data and averaged-pole transfer function model at the transient phase for all components was plotted. The averaged-pole transfer function model underestimates the temperature at the lower speed until the system reaches 40% of the nominal speed. The maximum temperature difference for all components occurs at 100% of the nominal speed, with the brush component leading the others with a discrepancy of 30 °C. The temperature difference at 60% of the speed is almost negligible for all components except for the brush.

The errors of transient-state temperature estimation in terms of percentage are also reported in Table 4.9 below. With these errors, the averaged-pole transfer function model which is LTI cannot replicate the thermal response of the motor in a transient state like in a steady state.

Table 4.9 Percentage error between experimental data and averaged-pole transfer function model at transient state for all components from Figure 4.7.

Component	Speed (% of nominal speed of 2650rpm)						
	20%	40%	60%	80%	100%		
Brush	-8.2%	-4.2%	13.7%	48.4%	102.3%		
Bearing	-8.2%	-11.4%	-1.7%	13.5%	41.8%		
Permanent Magnet	-27.4%	-11.7%	-2.1%	13.2%	42.1%		
Casing	-7.5%	-11.6%	-2.2%	12.8%	42.4%		

In conclusion, the estimated baseline temperature of the motor components using the averaged transfer function has too large errors and inconsistency in both steady state and transient state temperature. The non-linear nature of the motor thermal system in response to speed input cannot be approximated by averaging the poles of the transfer functions of the components at different speeds.



4.5.2 Variable-pole Transfer Function

Variable-pole transfer function is the method where a generalized transfer function model with adaptive pole values that depend on the speed was constructed based on the variable pole function generated from curve fitting. To recall the method, subsection 3.4.3 can be referred to. Table 4.10 below presents the functions obtained by curve fitting to describe the variation of the pole and gain values regarding speed for each component. The symbol $\bar{\sigma}$ and \bar{K} signifies the pole function and the gain function respectively. The term 'fit type' indicates the type of function. Within the pole and gain functions, the letters a, b, c, and d are used for the coefficients of the exponential function, while p1, p2, and p3 are used for the coefficients of the polynomial function.

Table 4.10 Function for variable-pole position for each component.

k	$G_k(s)$	σ_{k}		$\overline{\sigma}$		Fit Type		SSE	K _k	K	Fit Type	SSE
			$\bar{\sigma}_1$	a*exp(b*x) + c*exp(d*x)	$\bar{\sigma}_1$	Exponential 2	$\bar{\sigma}_1$	7.41e-7				
	17		$\bar{\sigma}_2$	a*exp(b*x) + c*exp(d*x)	$\bar{\sigma}_2$	Exponential 2	$\bar{\sigma}_2$	6.63e-7				
Brush	$\frac{K}{s + \sigma_b}$	$\sigma_{\mathbf{k}}$	$\bar{\sigma}_3$	p1*x^2 + p2*x + p3	$\bar{\sigma}_3$	Polynomial 2	$\bar{\sigma}_3$	6.16e-9	$\mathbf{K}_{\mathbf{k}}$	p1*x^2 + p2*x + p3	Polynomial 2	1.14e-17
	S T OK			p1*x^2 + p2*x + p3								
			$\bar{\sigma}_{2i}$	p1*x^2 + p2*x + p3	$\bar{\sigma}_{2i}$	Polynomial 2	$\bar{\sigma}_{2i}$	5.90e-6				
Bearing	$\frac{\mathbf{K}}{\mathbf{s} + \sigma_{\mathbf{k}}}$	$\sigma_{\mathbf{k}}$	ć	a*exp(b*x) + c*exp(d*x)		Exponential 2	3	.89e-9	$K_{\mathbf{k}}$	p1*x + p2	Polynomial 1	1.16e-9
P. magnet	$\frac{\mathbf{K}}{\mathbf{s} + \sigma_{\mathbf{k}}}$	$\sigma_{\mathbf{k}}$	â	a*exp(b*x) + c*exp(d*x)		Exponential 2				p1*x+p2	Polynomial 1	1.29e-9
Casing	$\frac{\mathbf{K}}{\mathbf{s} + \sigma_{\mathbf{k}}}$	$\sigma_{\mathbf{k}}$	٩	*exp(b*x) + c*exp(d*x)	1	Exponential 2	4	.76e-9	K_k	p1*x+p2	Polynomial 1	1.32e-9

As observed in the table, the complex conjugate pole pair for the brush $\bar{\sigma}_{1i}$ and $\bar{\sigma}_{2i}$ functions have the highest SSE of 5.90e-6. Conversely, the bearing pole function has the lowest SSE, estimated at 3.89e-9. The brush gain function exhibits the lowest SSE at 1.14e-17, while the other components have higher SSE errors at a magnitude of order of 1e-9. The pole function is represented by mostly exponential functions except for the third pole and the two complex poles of the brush which are represented by polynomial functions. All the gain functions are exclusively represented by the polynomial function. Overall, all the poles and gain are well-fitted with all the errors are extremely small (lower than 10^{-5}).

Moving on to the validation process of the variable-pole transfer function model, the implementation of these variable-pole functions is validated in comparison to the experimental data both at steady state and transient state. Figure 4.8 shows this comparison between at steady state for the component brush. For other components, the comparison can be found in Appendix M. The comparison is done at the five speed points from 20% to 100% of the nominal speed. The blue line represents the experimental data, while the black line represents the response of the variable-pole transfer function model. Additionally, the absolute temperature difference between the experimental data and the variable-pole transfer function model is also plotted in red.

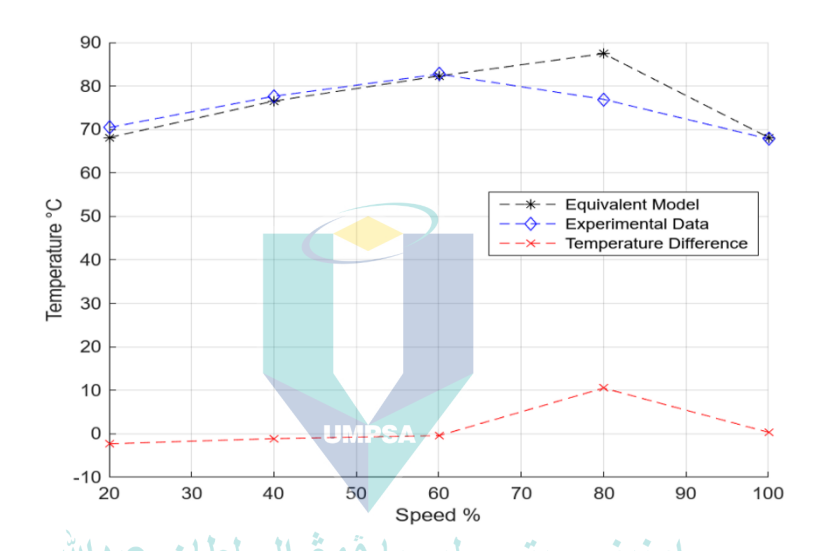


Figure 4.8 Comparison between variable-pole transfer function vs. experimental temperature response at steady state temperature (brush).

It can be observed that the variable-pole transfer function model barely underestimates the temperature response of the component brush at 20% and 40% of the nominal speed with an estimation error of less than 2°C. The generalized model accurately predicts the temperature response at 60% before largely overestimating the temperature at 80% of the nominal speed with an observed error of 10 °C. 80% speed is the speed at which the maximum estimation error is observed, after which the estimation becomes precise again at 100% of the nominal speed with zero error observed. The variable-pole transfer function model can be seen following the trend of increasing temperature as the speed first increases, then decreasing temperature towards the end. The variation of the pole, adapted to the speed input has managed to allow the temperature estimation to follow the change in direction and be more precise.

However, the turning point at which the temperature variation changes its slope after 60% of the nominal speed is a complex behavior that cannot be captured even by the adaptive pole. It may be suggested that if the sampling of temperature were done at more speed points, the change of temperature slope may be better captured. The influence of the sampling resolution for model construction is however out of our research scope and will be done in a future study. Nevertheless, to properly test this variable-pole transfer function model, it will also be confronted to a comparison with an experimental temperature taken at different speeds, other than the original five speed points of 20%, 40%, 60%, 80%, and 100%. This will be presented later in subsection in 4.5.3.

The summary of the temperature difference between experimental data and the variable-pole transfer function model at steady state for all the components of the motor at different speeds is reported in Table 4.11 and plotted as a bar chart in Figure 4.9 for a visual comparison. The individual comparison graph can be found in Appendix M.

Table 4.11 The temperature difference °C of the variable-pole transfer function at steady state for all components at different speeds.

Speed (%	of nominal speed of 2650rpm)
20% UMPSA40%	60% 80%	100%
-2.3°C -1°C	-0.4°C 10.5°C	0.3°C
2.4°C -2.5°C	-4.1°C 0.4°C	4.4°C
2.3°C -2.6°C	-4.2°C 0.4°C	4.6°C
2.3°C -2.5°C	A P-4.3°C 0.2°C	4.8°C
	20% 40% -2.3°C -1°C 2.4°C -2.5°C 2.3°C -2.6°C	-2.3°C -1°C -0.4°C 10.5°C 2.4°C -2.5°C -4.1°C 0.4°C 2.3°C -2.6°C -4.2°C 0.4°C

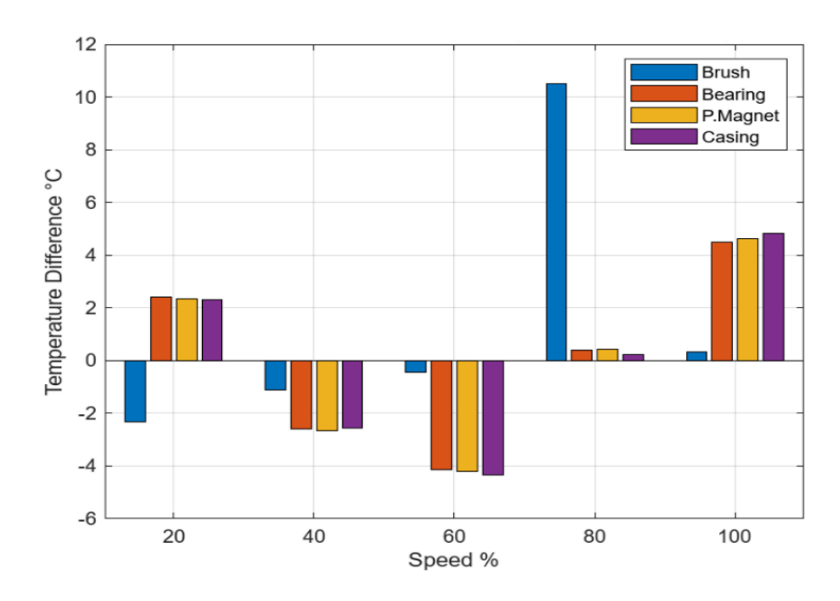


Figure 4.9 Temperature different between experimental and variable-pole transfer function model for all components at steady state.

Figure 4.9 illustrates the temperature difference between the experimental data and the variable-pole transfer function model for all components in a steady-state scenario. It is observed that the variable-pole transfer function model overestimates the temperature for the components bearing, permanent magnet, and casing at 20% and 100% of the nominal speed, and it underestimates the temperature of the same components at 40% and 60% of the nominal speed. For these components, across the range of speed variations, the temperature difference was less than 5 °C, and the model precisely predicted the temperature at 80% of the nominal speed.

AL-SULTAN ABDULLAH

Exceptionally for the brush, its temperature response exhibits the maximum temperature difference observed at 80% of speed with a temperature difference of 10 °C. It is the less precise when other components exhibit the most precise estimation. This shows that, unlike other components, the brush pole function may need to be improved by reducing the curve-fitting SSE error. It is in accordance with the observation made from Table 4.10 where the highest SSE errors were identified in brush pole functions. So, despite the high SSE error condition of less than 10⁻⁵, the pole function of the brush generated a temperature response that has a 10 °C of temperature difference in comparison to the experimental data.

The errors of steady-state temperature estimation in terms of percentage are also reported in Table 4.12 below. With these errors, the variable-pole transfer function model which is shown to be able to replicate the thermal response of the motor in a steady state. The brush estimation difference at 80% of speed may seem high at 13.7%, but in absolute temperature, it reflects only a difference of 10 °C. At a higher ambient temperature, the percentage would have been much lower.

Table 4.12 Similarity percentage between experimental and variable-pole transfer function model for all components at steady state.

Component	Speed (% of nominal speed of 2650rpm)							
	20%	40%	60%	80%	100%			
Brush	-3.3%	-1.4%	-0.5%	13.7%	0.5%			
Bearing	4.6%	-4.1%	-6%	0.6%	7.5%			
Permanent Magnet	4.6%	-4.2%	-6.1%	0.7%	7.7%			
Casing	4.6%	-4%	-6.3%	0.4%	8.2%			



Moving on to the validation in transient phase, Figure 4.10 provides a comparison of transient temperatures at a time constant ($\tau = 2160$ seconds) for the component brush. (Refer to Appendix N for other components). The experimental data temperature is represented by the blue line, while the variable-pole transfer function model estimated temperature is depicted by the black line. Additionally, the figure also includes a plot of the temperature differences between the experimental data and the variable-pole transfer function model, which is represented in red line.

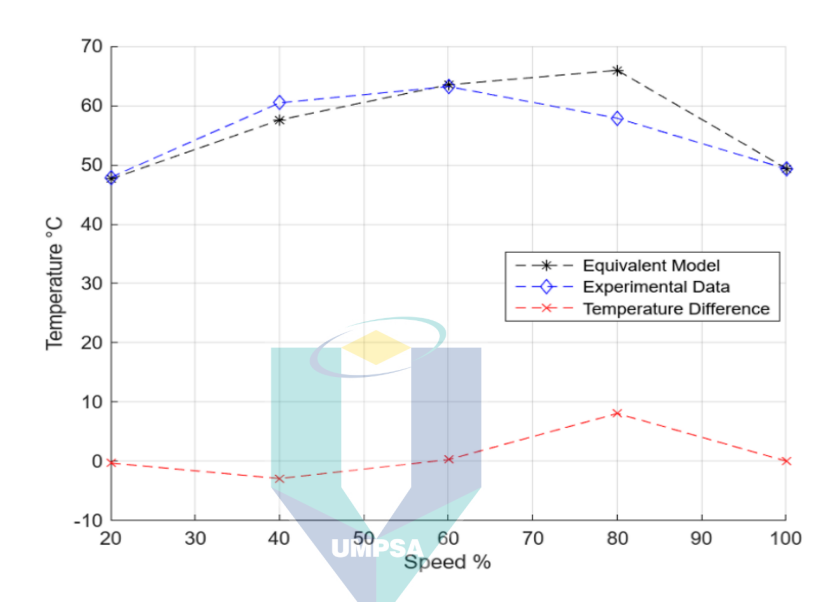


Figure 4.10 Comparison between variable-pole transfer function vs. experimental temperature response at transient temperature (brush).

The variable-pole transfer function model demonstrates a commendable ability to track the variation of the temperature response of the DC machines, even during the transient state. This observation is particularly noteworthy, as the equivalent model accurately predicts the temperature response at three distinct speeds: 20%, 60%, and 100% of the nominal speed with no errors observed.

However, it is important to note that the model does not perform uniformly across all speeds. Similar to the steady state response, the model underestimates the temperature at 40% of the nominal speed by approximately 3 °C and overestimates the temperature by 8 °C at 80% of the nominal speed which is the highest estimation error observed. Despite these discrepancies, the model's temperature differences do not exceed the maximum temperature differences at the steady state, which shows its overall reliability.

The summary of the temperature difference between experimental data and the variable-pole transfer function model at the transient state of all components at different speeds is shown in Table 4.13 and plotted in a bar chart for visual comparison in Figure 4.11.

Table 4.13 The temperature difference °C of variable-pole transfer function at transient state of all component at different speed.

Component	Speed (% of nominal speed of 2650rpm)							
	20%	40%	60%	80%	100%			
Brush	-0.2°C	-2.8°C	$0.2^{\circ}\mathrm{C}$	8°C	0.1°C			
Bearing	1.5°C	-2.4°C	-1.8°C	-0.4°C	3.5°C			
Permanent Magnet	-9.6°C	-2.5°C	-2°C	-0.4°C	3.6°C			
Casing	1.5°C	-2.5°C	-2°C	-0.6°C	3.8°C			

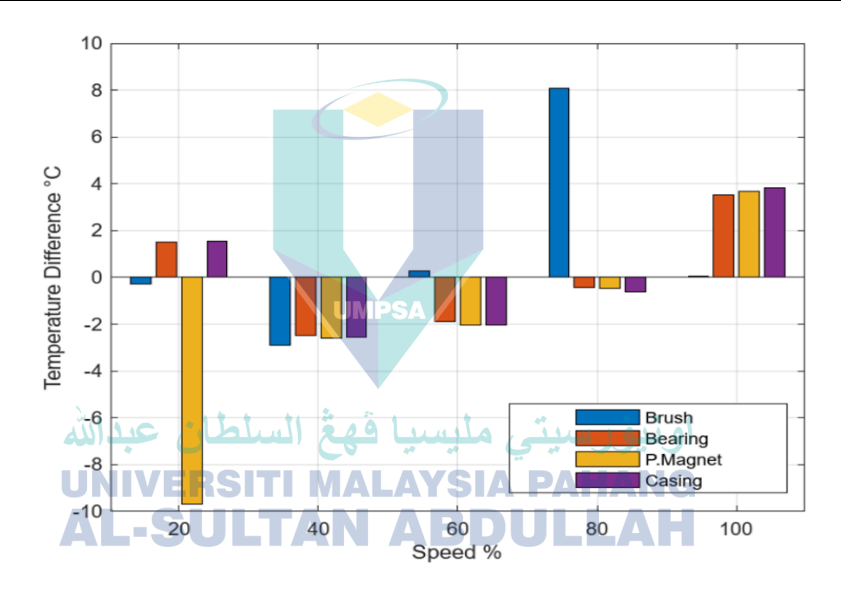


Figure 4.11 Temperature difference between experimental data and variable-pole transfer function model at transient state for all components.

In general, the brush's variable pole transfer function performs better where negligible temperature differences were noted with the exception at 80% of speed. Other components' models generate errors that are nonetheless acceptable of lower than 4 °C except for the permanent magnet. At 20% of speed, the variable-pole transfer function of the permanent magnet underestimates its temperature by 9 °C. It is however not disturbing as it is still lower than a difference of 10 °C. Added to that, it is observed at the lowest speed and in transient which is a lower temperature than at steady state and at other higher speed.

The errors of transient-state temperature estimation in terms of percentage are also reported in Table 4.14 below. With these errors, the variable-pole transfer function model is shown to be able to replicate the thermal response of the motor in the transient state as well as seen for the steady state previously. The brush and permanent magnet estimation difference of -18.4% and 14% may seem large, but in absolute temperature, it reflects only a difference of respectively 9 °C and 8 °C. At a higher ambient temperature, the percentage would have been much lower. It is worth noting that for temperature estimation purposes, an overestimation is safer than an underestimation as confirmed that the maximum degrading temperature is not yet attained. However, it prevents the system from operating at its maximum allowable temperature.

Table 4.14 Similarity percentage between experimental data and variable-pole transfer function model at transient state for all components.

Component	Speed (% of nominal speed of 2650rpm)						
	20%	40%	60%	80%	100%		
Brush	-0.6%	4.8%	0.5%	14%	0.1%		
Bearing	3.6%	4.7%	-3.4%	-0.8%	7%		
Permanent Magnet	-18.4%	4.9%	-3.6%	-0.8%	7.3%		
Casing	3.8% UMPSA-4	4.9%	-3.7%	-1.1%	7.7%		

In conclusion, the variable-pole transfer function model has demonstrated its ability to accurately model the temperature response of the DC machines in both steady state and transient state scenarios with the acceptable temperature differences of less than 10 °C. Therefore, it can be confidently used as a reliable model for estimating electrical machine baseline temperature across different speed ranges and can be implemented in real-time applications.

4.5.3 Test Validation for Model Robustness at Different Speed Points

From the previous chapter, the variable-pole transfer function was validated. The validation was done at 5 different speeds. To further check its robustness, the model is confronted with a test at different speeds which were not used in the variable-pole function development. Running the model in real-time and comparing it to the temperature measured is here done for a speed increment of 10%.

Figure 4.12 shows the comparison between the baseline temperature estimated by the variable-pole transfer function model (in red line) and the temperature measured on the machine (in black line) at steady state on the component brush. The increment of 10% of speed makes up to a total of 10 speeds at which the temperature can be compared.

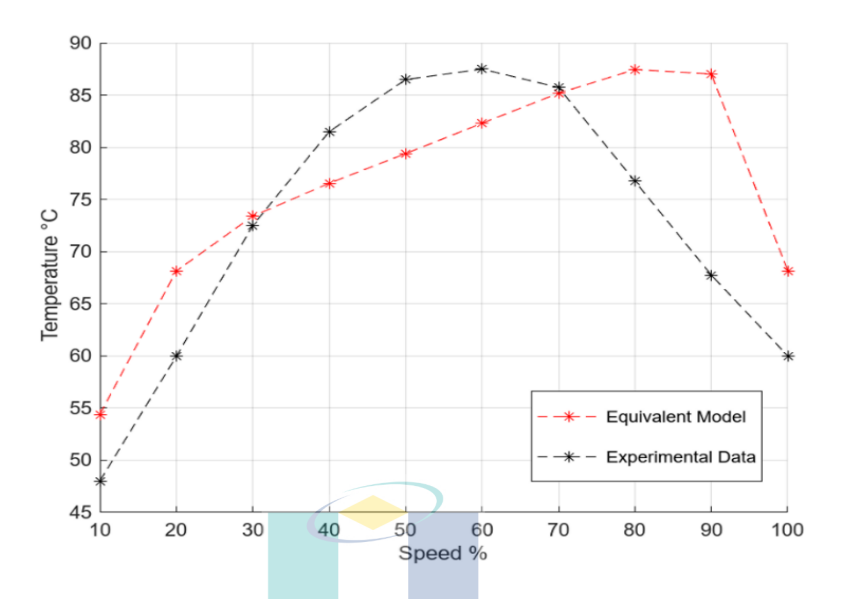


Figure 4.12 Comparison between equivalent model vs. experimental data at different speed point (brush).

Noted that the estimated baseline temperature follows the general trend of the measured temperature. With the variable pole function defined at an interval of 20% speed, the estimated temperature exhibits an LTI characteristic in each 20% interval. For example, from the speed of 60% to 80%, the increasing temperature trend sustains, failing to capture the already changing trend (from a positive slope to a negative slope) in the measured temperature. So, instead of having a maximum temperature at 60% of speed as in the measured temperature, the model gives an estimation of a maximum temperature achieved at 80% of speed. It is however noteworthy to remark that despite the difference in speed at which the maximum temperature is achieved, the value of the maximum temperature is the same at 87 °C.

The equivalent model accurately predicts the temperature response of the DC machines at 30% and 70% of the nominal speed. This precision provides a significant advantage when conducting condition monitoring of electrical machines at lower and medium speeds. Underestimation occurs between 40% and 60% of speed, but the

difference is smaller than 10 °C. It is important to observe that the maximum temperature difference was recorded at 90% of the nominal speed, with a deviation of approximately 20 °C overestimation. The speed of 90% is a speed that was not sampled for the construction of the variable pole function. It is therefore clear that to develop a model that estimates the baseline temperature precisely across the speed, more sampling is needed to develop the variable-pole transfer function. At 5 samples, the model is unreliable with a 20 °C overestimation observed.

It can also be remarked that the difference between the model and the measured temperature is slightly different from what has been presented during validation at previously sampled speed (of 20% increments) in Figure 4.8. The experimental temperature is different from the one presented in Figure 4.8 due to a potential variation of thermocouple placements and attachment. To have a robust estimation, the positioning, and the attachment of the thermocouple during data acquisition for model development need to be consistent with the one that will be used during the monitoring application. The variability of the differences (between measured and estimated temperature) due to uncertainties of thermocouple positioning and attachment will be another subject for a future study.

4.6 Objective 3 : Usage of Generalized Transfer Function in Fault Detection وثيوْرسيتي مليسيا فهغ السلطان عبدالله

Having validated the model in previous sections (except at 90% of speed due to the robustness of the model at higher speed resolution), an implementation case is going to be demonstrated in this last section. The objective is to demonstrate the usability of the baseline temperature estimation model (variable-pole transfer function model) in detecting anomalies in faulty DC machines. The faults in detail were explained in the methodology chapter (3.2.5). The idea is that anomalies can be detected if the measured temperature differs from the estimated baseline temperature. To do so, experimental temperature data of healthy machine, and machine with faulty bearings and faulty brushes were taken at different speeds.

Figure 4.13 shows the steady-state temperature response of the DC machine at three different states of health, monitored on the brush. The magenta line represents the DC machine with degreased bearing, the blue line represents the machine with broken brush and lastly the black line represents the healthy motor.

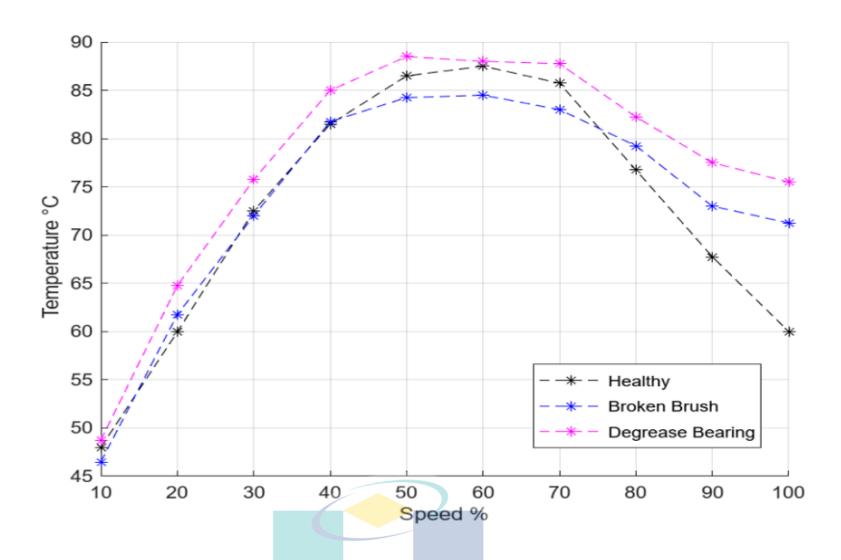


Figure 4.13 Comparison between healthy and faulty DC machines (brush).

It can be observed that the DC machines with degreased bearings (magenta line) exhibited the highest temperature throughout the speed range. The temperature difference between the motor with degreased bearing and the healthy motor is approximately 5 °C from 10% to 70% of the nominal speed. It can be said that despite a consistently higher temperature, the difference is minimal. However, from 80% to 100% of the nominal speed, the temperature difference increased as the speed increased, indicating that the friction in the bearing generates much higher losses, and is transferred to the brush. This is consistent with a friction-generated force which is viscous, thus increasing with the square of the speed. So, despite the decrease in temperature exhibited by the healthy motor (better convection at higher speed), the temperature decrease is much slower in the faulty machine.

The temperature response of the motor with a broken brush (blue line) presents a similar temperature to a healthy motor until 40% of speed, after which the temperature becomes lower with a difference of close to 4 °C, located at 60% of speed. It is also the speed at which the maximum temperature is achieved. Similar to the bearing fault, the temperature difference with the healthy machine increases towards higher speed

indicating an increase in losses with speed. This can be explained by the less smooth contact between the brush and commutator caused by the chipped brush surface. As in frictional generated losses, friction forces are viscous and increase with the square of the speed. Therefore, the same remark as in the bearing fault is also true here. The only difference is that the degreased bearing temperature is higher than the broken brush temperature.

In practical implementation, the temperature of the machine in Figure 4.13 will be plotted and compared with the baseline temperature estimated by the variable-pole transfer function. Figure 4.14 shows this comparison for the component brush. The comparison for other components can be found in Appendix O. Added to the previous graph is now the baseline estimated temperature in the red line.

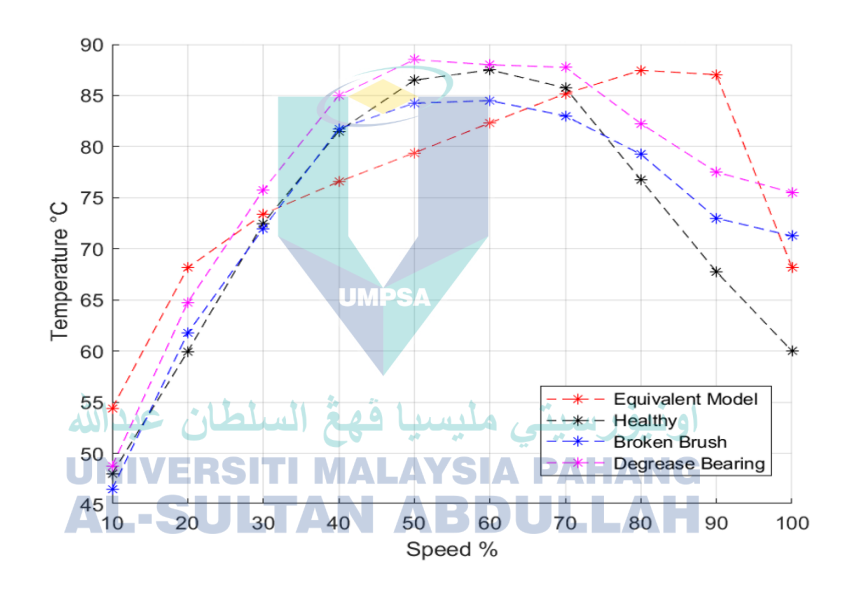


Figure 4.14 Comparison between variable-pole transfer function model vs. healthy and faulty DC machines (brush).

In Figure 4.14, it is observed that in general, the variable-pole transfer function model (called here the equivalent model for short) overestimates the temperature at the lower (< 20%) and upper speed (> 80%) ranges, while it underestimates at the middle speeds. Just like in Figure 4.12, the equivalent model accurately predicts the temperature response of the DC machines at 30% and 70% of the nominal speed. The temperature at 0% and 100% speed are interesting speed points that can be considered for anomaly detection. A proposition for its usage can take the following form:

During steady-state operation, electrical machines typically operate at full-rated speed (100%). A measurement of temperature that shows a brush temperature higher than the estimated baseline temperature would indicate an occurrence of a fault. However, confirmation on which fault between the brush and bearing fault cannot be definitively identified because the temperature difference between the two faults of less than 5 °C from our experiments (Figure 4.14) may be too small, considering other uncertainties. All those knowns are that a fault occurs.

To distinguish the bearing fault from the brush fault, the temperature at 70% of speed may be used. Running at 70% speed, it can be seen from Figure 4.14 that the brush fault has a lower temperature than the healthy machine, while a bearing fault has a higher temperature. This comparison would allow a distinction between the 2 faults.

Figure 4.15 below shows the summary of the temperature difference between the equivalent model versus healthy and faulty DC machines extracted from Figure 4.14 in a bar chart. The useful speed point of 100% and 70% speed can be seen exhibiting the useful characteristics previously mentioned.

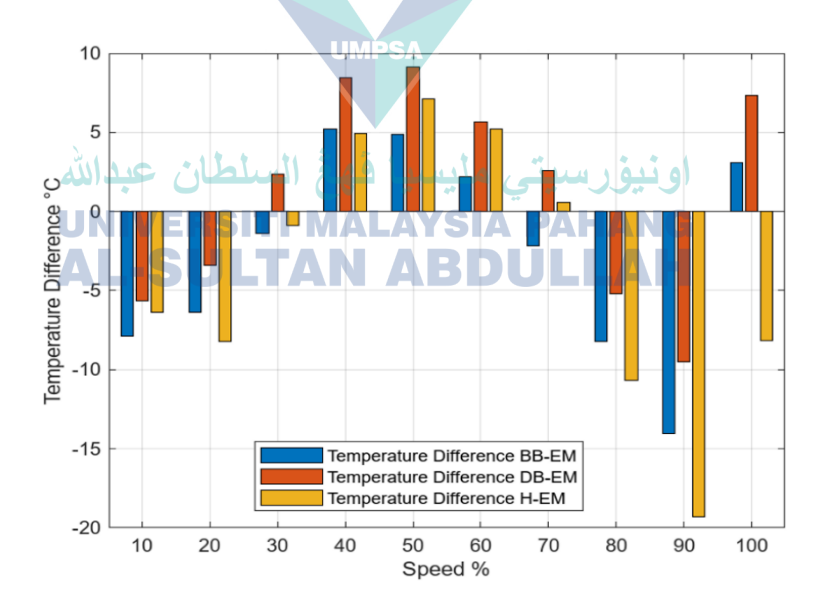


Figure 4.15 Temperature differessnce between variable-pole transfer function vs. faulty and healthy DC machines (brush).

Another component where anomaly detection can be done is in the component casing. This observation can be seen in Figure 4.16, which clearly shows that the temperature response of both faulty motors exceeded that of the healthy motor starting at as low as 30% of speed and continuing to increase as the speed increased.

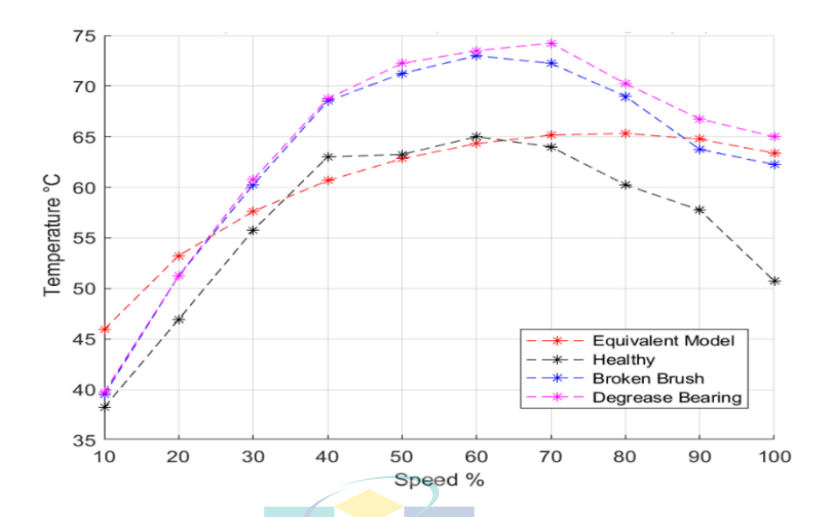


Figure 4.16 Comparison between variable-pole transfer function model vs. healthy and faulty DC machines (casing).

The equivalent model for the casing provides an accurate estimation of the temperature response at the intermediate stage, specifically within the speed range of 30% to 70% of the nominal speed. However, it overestimates the temperature response at the lower and higher speed ranges. While the differences between the brush and bearing fault are small across the speed range below 90%, the temperature difference between both the faulty motors and the healthy motors exceeds 5 °C at all speeds starting from 30%. The highest temperature recorded was approximately 75 °C at 70% of the nominal speed for the motor with a decreased bearing. A proposition for the usage of the estimated temperature on the casing can take the following form:

The equivalent model can be effectively utilized for anomaly detection when the motor operates within a speed range of 30% to 70%. If the temperature reading at the casing exceeds the equivalent model by 5 °C, it is indicative of a fault. This method is employed for early fault detection in electrical machines. However, it can pose a challenge to pinpoint the specific type of fault, whether it is a brush or a bearing fault. To classify the fault, a method using temperature readings at the brush component that was previously discussed can be implemented.

Figure 4.17 below shows the summary of the temperature difference between the equivalent model versus healthy and faulty DC machines extracted from Figure 4.16 in a bar chart. The useful speed point between 30% and 70% speed can be seen exhibiting a higher temperature of more than 5 °C as previously mentioned.

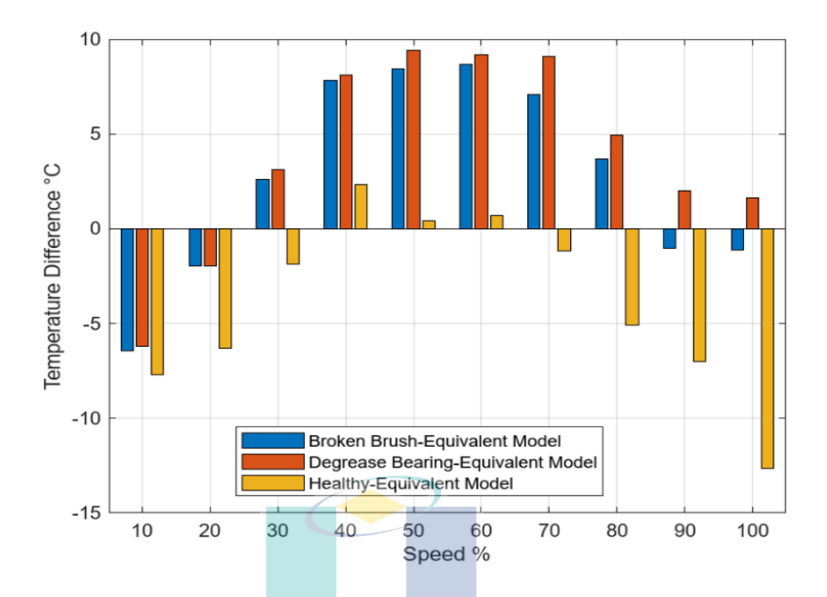


Figure 4.17 Temperature difference between variable-pole transfer function vs. faulty and healthy DC machines (casing).

Based on all the obtained results, it can be inferred that the application of the generalized transfer function as an anomaly detection tool is feasible. It will alarm the user to trigger a more in-depth diagnostic process or maintenance. Therefore, a scheduled preventive maintenance process could be reduced, decreasing the total down time and maintenance cost.

CHAPTER 5

CONCLUSION

5.1 Introduction

The use of DC machines will continue to grow as industries strive to meet their green and sustainability goals through electrification. To ensure a long lifespan and reliable performance, it is crucial to prevent overheating of the machines. It is even more advantageous to detect anomalies before the maximum temperature is reached, particularly when the machine is operating at lower speeds and under low or no-load conditions. Therefore, the motivation of this study is to explore a potential solution for estimating the baseline temperature of the machine when it operates at any speed, starting with no-load conditions. The estimated baseline temperature can then be compared to the measured temperature and the discrepancy between the two can serve as an anomaly detection.

The development of this baseline temperature estimation was done using transfer functions due to its ability to represent the temperature response to a speed input using a single block which can be implemented easily in real time. Addressing the first objective, the identification of the transfer function of different motor components (brush, bearing, permanent magnet, and casing) running with no load at 5 speed samples was done using the Identification Toolbox by MATLAB. The brush was best represented by a 3rd order transfer function, while a 1st order transfer function is sufficient to represent other components. The transfer functions of each component at different speeds were found to not obey the LTI system assumption after a linearity analysis due to the complex nature of heat transfer in the DC machine.

Following the observation, the second objective was addressed by developing a generalized transfer function that can represent the temperature response of the machine at any speed. Using an averaged-pole transfer function, the validation test shows a nonacceptable estimated temperature which is expected because the system was found previously to be non-LTI. The baseline temperature estimation error increases as the speed increases. The poles of the generalized transfer function need to be adaptable depending on the speed. Therefore, in the second method, the pole values of the transfer function are generated by a pole function that was defined using mathematical equations deduced from a curve fitting. The validation shows that the trends of the temperature response exhibited by the model follow the one observed in the experimental data. The precision was validated after observing a maximum steady state estimation error of 10 °C at 80% of the motor's nominal speed. At the transient state, the estimation error is much lower at 8 °C when the motor speed is also 80%. The variable-pole transfer function was chosen and can be refer at Table 4.10. Meanwhile, for the specific chases that conducted same as the experiment in data generation, the identified transfer function in Table 4.3 can be used as model. A robustness test confronting the model to a higher speed sampling resolution at a 10% speed increment was also done. It was shown that a higher number of speeds at which the temperature response was sampled for transfer function identification can increase the model temperature estimation.

اونيؤرسيتي مليسيا فهغ السلطان عبدالله

In the last objective, the validated variable-pole transfer function model was confronted with an anomaly detection feasibility test where its temperature response was compared to the temperature response of machines with broken brushes and degreased bearings. The comparison shows that the casing temperature response can be used, where a higher measured temperature in comparison to the estimated temperature by the model of more than 5 °C in the speed range of 30% - 70% indicates an occurrence of a fault. A further distinction between brush and bearing fault can be made by looking at the temperature on the brush at a speed of 70%. A bearing fault would be indicated by a higher estimated temperature while a brush fault would be indicated by a lower temperature. This observation proves that the concept of anomaly detection and fault identification using the baseline temperature model is feasible.

Finally, to conclude, several remarks can be made concerning the positioning of the results obtained in this study in comparison to previous findings and development in literature reviews. For comparison, (Ray et al., 2020), an algorithm for loose brush contact was developed with a 1.5-second delay in fault detection whereas our model can instantly signal anomalies via discrepancies of baseline estimated temperature in comparison to measured temperature. The development and monitoring using the algorithm itself need current measurement instrumentation which is much more expensive than thermocouples. In comparison to studies employing artificial intelligence such as neural networks (Benedik et al., 2015 and Silva et al., 2023), this study does not need a huge amount of historical data. A baseline temperature model was constructed from a new healthy model.

5.2 Perspectives

This thesis has made significant contributions to the development of a baseline temperature response model of an electric machine, using a generalized transfer function. Despite these advancements, there are still areas of research that could be explored in future studies to expand the work presented herein. These potential avenues for further investigation can be categorized as follows:

- 1. Increase sampling experimental data: The development of the transfer function in this thesis was based on 5 points speed sampling of the nominal speed. To enhance the model's predictive accuracy for motor temperature, it is recommended to increase the sampling of experimental data used in the model's development. This could include expanding the sample data to 10, 15, 20, 25, and 30 data points.
- 2. Implement transfer function model to motor under load condition: The model presented in this thesis was developed and studied based on a DC machine operating under no-load conditions. For future research, it would be useful to develop and study the model on a DC machine under varying load conditions, with a magnetic brake attached as load. This would allow for an examination of the model's capability to predict the temperature response of the DC machines, as well as an investigation into the characteristics of the temperature response

- when a load is applied. The input in this case would be multiple, the speed and the load which will be more complex to treat.
- 3. Implement transfer function model on various motors: This thesis has observed a complex speed-dependant phenomenon in the temperature response of the MY1016 motor, which exhibits an increasing trend from the initial to the middle state of nominal speed, followed by a decreasing trend until the final state of nominal speed. This is likely due to the complex internal structure of the DC machines. Therefore, it would be of interest to study the temperature response in motors with more complex structures, such as fan-cooled motors or totally enclosed motors. Concurrently, the transfer function model could be evaluated for its ability to accurately predict and follow the trend of the temperature response in these electric machines.



REFERENCES

- Abadie, C., Billard, T., & Lebey, T. (2019). Partial Discharges in Motor Fed by Inverter: From Detection to Winding Configuration. *IEEE Transactions on Industry Applications*, 55(2). https://doi.org/10.1109/TIA.2018.2874875
- Abdelli, A., Chareyron, B., & Nasr, A. (2020). Separation of the losses at no load conditions in the electric motor with oil cooling shaft. 23rd International Conference on Electrical Machines and Systems, ICEMS 2020. https://doi.org/10.23919/ICEMS50442.2020.9290851
- Acho, L., Pujol-Vázquez, G., & Gibergans-Báguena, J. (2020). A Recent Electronic Control Circuit to a Throttle Device. *Electronics*, 9(1). https://doi.org/10.3390/electronics9010191
- Ai, Z., Zhang, Y., Zhang, Y., Feng, Y., Zhang, J., & Murphey, Y. (2018). Smart Pinch Detection for Car's Electric Sunroof Based on Estimation and Compensation of System Disturbance. *Control and Systems Engineering*, 1. https://doi.org/10.18063/cse.v1i1.398
- Akaike, H. (1971). Autoregressive model fitting for control. *Annals of the Institute of Statistical Mathematics*, 23(1), 163–180. https://doi.org/10.1007/BF02479221
- Akaike, H. (1974). A New Look at the Statistical Model Identification. *IEEE Transactions on Automatic Control*, 19(6). https://doi.org/10.1109/TAC.1974.1100705
- Akram, S., Wang, P., Zhu, X., Huang, J., Liu, F., Fang, Z., & Ahmed, H. (2023). Prediction of Partial Discharge Inception Voltage for Electric Vehicle Motor Insulation Using Deep Learning. *IEEE Transactions on Instrumentation and Measurement*, 72. https://doi.org/10.1109/TIM.2023.3269120
- Al Khafaji, F. S. M., Wan Hasan, W. Z., Isa, M. M., & Sulaiman, N. (2019). A HSMDAQ System for EstimatingTransfer Function of a DC motor. *Asia Pacific Conference on Postgraduate Research in Microelectronics and Electronics*, 2019-November. https://doi.org/10.1109/PrimeAsia47521.2019.8950719
- Alfredo Osornio-Rios, R., Antonino-Daviu, J. A., & De Jesus Romero-Troncoso, R. (2019). Recent industrial applications of infrared thermography: A review. *IEEE Transactions on Industrial Informatics*, 15(2). https://doi.org/10.1109/TII.2018.2884738

- Anoop, G. L., Mini, V. P., Harikumar, R., & Mayadevi, N. (2020, November 27). Thermal analysis of squirrel cage Induction Motor. 2020 IEEE International Conference on Power Electronics and Renewable Energy Applications, PEREA 2020. https://doi.org/10.1109/PEREA51218.2020.9339772
- Anshory, I., Robandi, I., & Wirawan. (2020). Identification parameter system for mathematical modeling BLDC motor using transfer function models. *IOP Conference Series: Materials Science and Engineering*, 821(1). https://doi.org/10.1088/1757-899X/821/1/012023
- Avina-Corral, V., Rangel-Magdaleno, J., Morales-Perez, C., & Hernandez, J. (2021). Bearing Fault Detection in Adjustable Speed Drive-Powered Induction Machine by Using Motor Current Signature Analysis and Goodness-of-Fit Tests. *IEEE Transactions on Industrial Informatics*, 17(12). https://doi.org/10.1109/tii.2021.3061555
- Azri, M., Rasid, H., Friedrich, G., Doc, C., Examiner, R., & Lanfranchi, V. (2016). Contribution to multi-physical studies of small synchronous-reluctance machine for automotive equipment Information and System Technologies in front of the jury panel.
- Badoni, S., & Jarial, R. K. (2021). Health Monitoring of three phase induction motor using infrared thermography. *Proceedings of the 6th International Conference on Communication and Electronics Systems, ICCES* 2021, 156–160. https://doi.org/10.1109/ICCES51350.2021.9489095
- Balakrishnan, V. (2002). System identification: theory for the user (second edition): Lennart Ljung; Prentice-Hall, Englewood Cliffs, NJ, 1999, ISBN 0-13-656695-2. *Automatica*, 38(2), 375–378. https://doi.org/https://doi.org/10.1016/S0005-1098(01)00214-X
- Bermudez, M., Arahal, M. R., Duran, M. J., & Gonzalez-Prieto, I. (2021). Model Predictive Control of Six-Phase Electric Drives including ARX Disturbance Estimator. *IEEE Transactions on Industrial Electronics*, 68(1). https://doi.org/10.1109/TIE.2019.2962477
- Bilgin, B., Liang, J., Terzic, M. V., Dong, J., Rodriguez, R., Trickett, E., & Emadi, A. (2019).
 Modeling and Analysis of Electric Motors: State-of-the-Art Review. *IEEE Transactions on Transportation Electrification*, 5(3). https://doi.org/10.1109/TTE.2019.2931123
- Blundell S.; Blundell K. (n.d.). Concepts in Modern Physics 2006. Oxford University Press.

- Bonnett, A. H., & Soukup, G. C. (1992). Cause and Analysis of Stator and Rotor Failures in Three-Phase Squirrel-Cage Induction Motors. *IEEE Transactions on Industry Applications*, 28(4). https://doi.org/10.1109/28.148460
- Bouafia, M., Bertin, Y., Saulnier, J. B., & Ropert, P. (1998). Analyse expérimentale des transferts de chaleur en espace annulaire étroit et rainuré avec cylindre intérieur tournant. *International Journal of Heat and Mass Transfer*, 41(10). https://doi.org/10.1016/S0017-9310(97)00317-7
- Brusamarello, B., Da Silva, J. C. C., De Morais Sousa, K., & Guarneri, G. A. (2023). Bearing Fault Detection in Three-Phase Induction Motors Using Support Vector Machine and Fiber Bragg Grating. *IEEE Sensors Journal*, 23(5). https://doi.org/10.1109/JSEN.2022.3167632
- Cao, W., Huang, R., Wang, H., Lu, S., Hu, Y., Hu, C., & Huang, X. (2023). Analysis of Inter-Turn Short-Circuit Faults in Brushless DC Motors Based on Magnetic Leakage Flux and Back Propagation Neural Network. *IEEE Transactions on Energy Conversion*, 38(4). https://doi.org/10.1109/TEC.2023.3285899
- Chou, Y. C., & Yao, L. (2009). Automatic diagnosis system of electrical equipment using infrared thermography. *SoCPaR* 2009 *Soft Computing and Pattern Recognition*, 155–160. https://doi.org/10.1109/SoCPaR.2009.41
- Choupanzadeh, R., & Zadehgol, A. (2020). Stability, Causality, and Passivity Analysis of Canonical Equivalent Circuits of Improper Rational Transfer Functions with Real Poles and Residues. *IEEE Access*, 8. https://doi.org/10.1109/ACCESS.2020.3007854
- Cioboată, D., Neacşu, M. G., Stanciu, D., Matei, S. Ştefan, & Neacşu, I. (2020). Modelling and simulation of a brushless motor dc for electric power steering assistance. *EEA Electrotehnica*, *Electronica*, *Automatica*, 68(3). https://doi.org/10.46904/eea.20.68.3.1108003
- Colombo, L., Corradini, M. L., Cristofaro, A., Ippoliti, G., & Orlando, G. (2019). An Embedded Strategy for Online Identification of PMSM Parameters and Sensorless Control. *IEEE Transactions on Control Systems Technology*, 27(6). https://doi.org/10.1109/TCST.2018.2862415
- Craiu, O., Machedon, A., Tudorache, T., Morega, M., & Modreanu, M. (2010). 3D finite element thermal analysis of a small power PM DC motor. *Proceedings of the International Conference on Optimisation of Electrical and Electronic Equipment, OPTIM*, 389–394. https://doi.org/10.1109/OPTIM.2010.5510335

- Critical Raw Materials Resilience: Charting a Path towards greater Security and Sustainability. (n.d.). Retrieved December 18, 2023, from https://eur-lex.europa.eu/legal-content/EN/TXT/?uri=CELEX:52020DC0474
- Cuiping, L., Pujia, C., Shukang, C., & Feng, C. (2014). Research on motor iron losses and temperature field calculation for mini electric vehicle. 2014 17th International Conference on Electrical Machines and Systems, ICEMS 2014. https://doi.org/10.1109/ICEMS.2014.7013887
- Dawood, A., Ismeil, M. A., Hussein, H. S., Hasaneen, B. M., & Abdel-Aziz, A. M. (2024). An Efficient Protection Scheme Against Single-Phasing Fault for Three-Phase Induction Motor. *IEEE Access*, 12. https://doi.org/10.1109/ACCESS.2024.3351106
- De Jesus Rangel-Magdaleno, J. (2021). Induction machines fault detection: An overview. In *IEEE Instrumentation and Measurement Magazine* (Vol. 24, Issue 7). https://doi.org/10.1109/MIM.2021.9549228
- Demetriades, G. D., De La Parra, H. Z., Andersson, E., & Olsson, H. (2010). A real-time thermal model of a permanent-magnet synchronous motor. *IEEE Transactions on Power Electronics*, 25(2). https://doi.org/10.1109/TPEL.2009.2027905
- Dennis, J. E., & Schnabel, R. B. (1996). *Numerical Methods for Unconstrained Optimization and Nonlinear Equations*. Society for Industrial and Applied Mathematics. https://doi.org/10.1137/1.9781611971200
- Dong, T., Zhang, X., Zhu, C., Lu, Y., & Li, M. (2020). Improved hotspot monitoring method for thermal management system of automotive traction motor. *IET Electric Power Applications*, 14(11). https://doi.org/10.1049/iet-epa.2020.0182

UNIVERSITI MALAYSIA PAHANG

- Donjaroennon, N., Nuchkum, S., & Leeton, U. (2021). Mathematical model construction of DC Motor by closed-loop system Identification technique Using Matlab/Simulink. *Proceeding of the 2021 9th International Electrical Engineering Congress, IEECON 2021*. https://doi.org/10.1109/iEECON51072.2021.9440305
- Electric Motor Failure Causes. (n.d.). Retrieved December 18, 2023, from https://electricalacademia.com/motor-control/electric-motor-failure-causes/
- El-Hasan, T. S. (2018). Development of automotive permanent magnet alternator with fully controlled AC/DC converter. *Energies*, 11(2). https://doi.org/10.3390/en11020274

- Ellis, G. (2012). The Frequency Domain. In *Control System Design Guide* (pp. 9–29). Elsevier. https://doi.org/10.1016/b978-0-12-385920-4.00002-3
- Fedosov, I. I. (2020). Thermocouple Condition Monitoring Using Thermocouple Resistance. Experimental Study. *Proceedings 2020 Ural Symposium on Biomedical Engineering, Radioelectronics and Information Technology, USBEREIT 2020*. https://doi.org/10.1109/USBEREIT48449.2020.9117727
- Ferreira, F. J. T. E., & de Almeida, A. T. (2008). Novel multiflux level, three-phase, squirrel-cage induction motor for efficiency and power factor maximization. *IEEE Transactions on Energy Conversion*, 23(1). https://doi.org/10.1109/TEC.2007.914355
- Gao, Q., Wang, X., Deng, Z., & Zhang, Y. (2023). Loss Calculation, Analysis, and Separation Method of 550 000 r/min Ultrahigh-Speed Permanent Magnet Motor. *IEEE Transactions* on *Industrial Electronics*, 70(4). https://doi.org/10.1109/TIE.2022.3177816
- García-Saldaña, J. D., Gasull, A., & Giacomini, H. (2020). A new approach for the study of limit cycles. *Journal of Differential Equations*, 269(7). https://doi.org/10.1016/j.jde.2020.04.038
- Gedlu, E. G., Wallscheid, O., & Bocker, J. (2021). Temperature estimation of electric machines using a hybrid model of feed-forward neural and low-order lumped-parameter thermal networks. 2021 IEEE International Electric Machines and Drives Conference, IEMDC 2021. https://doi.org/10.1109/IEMDC47953.2021.9449548

اونيؤرسيتي مليسيا فهغ السلطان عبدالله

- Glowacz, A., Glowacz, W., Glowacz, Z., & Kozik, J. (2018). Early fault diagnosis of bearing and stator faults of the single-phase induction motor using acoustic signals. *Measurement:*Journal of the International Measurement Confederation, 113. https://doi.org/10.1016/j.measurement.2017.08.036
- Glowacz, A., & Glowacz, Z. (2017). Diagnosis of the three-phase induction motor using thermal imaging. *Infrared Physics and Technology*, 81. https://doi.org/10.1016/j.infrared.2016.12.003
- Golnaraghi, F., & Benjamin C.Kuo. (2017). Automatic Control Systems(10th Edition). In *McGraw-Hill Education*.
- Gonzalez-Cordoba, J. L., Osornio-Rios, R. A., Granados-Lieberman, D., Romero-Troncoso, R. D. J., & Valtierra-Rodriguez, M. (2017). Correlation Model between Voltage Unbalance

- and Mechanical Overload Based on Thermal Effect at the Induction Motor Stator. *IEEE Transactions on Energy Conversion*, 32(4). https://doi.org/10.1109/TEC.2017.2706194
- Goodman, J. R., & Colombo, L. J. (2020). On the Existence and Uniqueness of Poincaré Maps for Systems with Impulse Effects. *IEEE Transactions on Automatic Control*, 65(4). https://doi.org/10.1109/TAC.2019.2941446
- Guo, G., & Cai, W. (2023). Prediction of Electromagnetic Vibration With Simulated Transfer Function for Interior Permanent Magnet Synchronous Motor. *IEEE Transactions on Energy Conversion*, 38(4). https://doi.org/10.1109/TEC.2023.3292061
- Gutfrind, C., Dufour, L., Liebart, V., & Migaud, J. (2015). Energy consumption comparison between two optimized limited motion actuator topologies for an EGR system used in automotive applications. PCIM Europe 2015; International Exhibition and Conference for Power Electronics, Intelligent Motion, Renewable Energy and Energy Management; Proceedings Of.
- Hattori, M., Murakami, S., Ohhira, T., & Hashimoto, H. (2023). A Coil Temperature Estimation for Disk Rotor Type Brushless DC Motors. *Proceedings 2023 IEEE International Conference on Mechatronics, ICM 2023*. https://doi.org/10.1109/ICM54990.2023.10101907
- He, C., Han, P., Lu, J., Wang, X., Song, J., Li, Z., & Lu, S. (2023). Real-Time Fault Diagnosis of Motor Bearing via Improved Cyclostationary Analysis Implemented onto Edge Computing System. *IEEE Transactions on Instrumentation and Measurement*, 72. https://doi.org/10.1109/TIM.2023.3295476
- He, Y., Tang, Y., Xie, H., Ke, D., & Wang, F. (2021). Rotor Optimization for Two-phase High-speed Switched Reluctance Motor. *Proceedings of the Energy Conversion Congress and Exposition* Asia, ECCE Asia 2021. https://doi.org/10.1109/ECCE-Asia49820.2021.9479399
- Huang, L. Y., Lu, S. Der, & Liu, H. D. (2023). New Graphene-Based on Nickel-Carbon Compounding Applied to Carbon Brushes of Traction Motors in Subway Vehicles. *IEEE Access*, 11. https://doi.org/10.1109/ACCESS.2023.3325431
- Idalgo, G. F., Altuna, J. A. T., Capovilla, C. E., Pelizari, A., & Schulter, W. (2019). DC Motor Model for Windows Pinch Protection Applications. 2019 IEEE 15th Brazilian Power Electronics Conference and 5th IEEE Southern Power Electronics Conference, COBEP/SPEC 2019. https://doi.org/10.1109/COBEP/SPEC44138.2019.9065778

- Jeffali, F., Ouariach, A., El Kihel, B., & Nougaoui, A. (2019). Diagnosis of three-phase induction motor and the impact on the kinematic chain using non-destructive technique of infrared thermography. *Infrared Physics and Technology*, 102. https://doi.org/10.1016/j.infrared.2019.07.001
- Ji, W., Ni, F., Gao, D., Luo, S., Lv, Q., & Lv, D. (2021). Electromagnetic design of high-power and high-speed permanent magnet synchronous motor considering loss characteristics. *Energies*, 14(12). https://doi.org/10.3390/en14123622
- Jing, H., Chen, Z., Wang, X., Wang, X., Ge, L., Fang, G., & Xiao, D. (2023). Gradient Boosting Decision Tree for Rotor Temperature Estimation in Permanent Magnet Synchronous Motors. *IEEE Transactions on Power Electronics*, 38(9). https://doi.org/10.1109/TPEL.2023.3291464
- Juditsky, A., Hjalmarsson, H., Benveniste, A., Delyon, B., Ljung, L., SjÖberg, J., & Zhang, Q. (1995). Nonlinear black-box models in system identification: Mathematical foundations. *Automatica*, 31(12), 1725–1750. https://doi.org/https://doi.org/10.1016/0005-1098(95)00119-1
- Khamisan, N., Ghazali, K. H., Almisreb, A., & Zin, A. H. M. (2018). Histogram-based of healthy and unhealthy bearing monitoring in induction motor by using thermal camera. *Journal of Telecommunication, Electronic and Computer Engineering*, 10(1–9).
- Khan, M. S., Okonkwo, U. V., Usman, A., & Rajpurohit, B. S. (2018). Finite Element Modeling of Demagnetization Fault in Permanent Magnet Direct Current Motors. *IEEE Power and Energy Society General Meeting*, 2018-August. https://doi.org/10.1109/PESGM.2018.8586622
- Khan, N., Rafiq, F., Abedin, F., & Khan, F. U. (2019). IoT based health monitoring system for electrical motors. *15th International Conference on Emerging Technologies, ICET 2019*. https://doi.org/10.1109/ICET48972.2019.8994398
- Khan, Q., Refaat, S. S., Abu-Rub, H., & Toliyat, H. A. (2020). Partial Discharge Modeling of Internal Discharge in Electrical Machine Stator Winding*. 2020 IEEE Kansas Power and Energy Conference, KPEC 2020. https://doi.org/10.1109/KPEC47870.2020.9167548
- Kiesenhofer, M. (2021). Assessment of an electrical coolant pump on a heavy-duty diesel engine. *SN Applied Sciences*, *3*(3). https://doi.org/10.1007/s42452-021-04340-x

- Kim, C. W., Jang, G. H., Kim, J. M., Ahn, J. H., Baek, C. H., & Choi, J. Y. (2017). Comparison of Axial Flux Permanent Magnet Synchronous Machines with Electrical Steel Core and Soft Magnetic Composite Core. *IEEE Transactions on Magnetics*, 53(11). https://doi.org/10.1109/TMAG.2017.2701792
- Kim, D. H., Im, J. H., Zia, U., & Hur, J. (2020). Online Detection of Irreversible Demagnetization Fault with Non-excited Phase Voltage in Brushless DC Motor Drive System. *ECCE 2020 IEEE Energy Conversion Congress and Exposition*. https://doi.org/10.1109/ECCE44975.2020.9235654
- Kirchgassner, W., Wallscheid, O., & Bocker, J. (2021). Estimating Electric Motor Temperatures with Deep Residual Machine Learning. *IEEE Transactions on Power Electronics*, *36*(7). https://doi.org/10.1109/TPEL.2020.3045596
- Kirchgässner, W., Wallscheid, O., & Böcker, J. (2023). Thermal neural networks: Lumped-parameter thermal modeling with state-space machine learning. *Engineering Applications of Artificial Intelligence*, 117. https://doi.org/10.1016/j.engappai.2022.105537
- Kumar, P., Bhaskar, D., Muduli, U. R., Beig, A., & Behera, R. K. (2022). Disturbance Observer Based Sensorless Predictive Control for High Performance PMBLDCM Drive Considering Iron Loss. *IEEE Transactions on Industrial Electronics*, 69(6). https://doi.org/10.1109/TIE.2021.3091937
- Kumar, P. S., Xie, L., Halick, M. S. M., & Vaiyapuri, V. (2021). Stator End-Winding Thermal and Magnetic Sensor Arrays for Online Stator Inter-Turn Fault Detection. *IEEE Sensors Journal*, 21(4). https://doi.org/10.1109/JSEN.2020.3029041
- Kwad, A. M., Hanafi, D., Omar, R. Bin, & Rahman, H. B. A. (2020). A Real-Time Nonlinear Hammerstein Model for Bidirectional DC Motor Based on Multi-Layer Neural Networks. 2020 IEEE Student Conference on Research and Development, SCOReD 2020. https://doi.org/10.1109/SCOReD50371.2020.9250988
- Langarica, S., Ruffelmacher, C., & Nunez, F. (2020). An Industrial Internet Application for Real-Time Fault Diagnosis in Industrial Motors. *IEEE Transactions on Automation Science and Engineering*, 17(1). https://doi.org/10.1109/TASE.2019.2913628
- Lee, H. W., Kim, T. H., & Choi, C. (2005). A novel internal fault analysis of a brushless DC motor using winding function theory. 2005 IEEE International Conference on Electric Machines and Drives. https://doi.org/10.1109/iemdc.2005.195694

- Li, J. (2020). Research on dc motor driver in automobile electric power steering system. *Proceedings - 2020 International Conference on Intelligent Transportation, Big Data and Smart City, ICITBS 2020.* https://doi.org/10.1109/ICITBS49701.2020.00097
- Li, S., Yang, G., Zhang, J., & Yang, J. (2022). An Online VSI Error Parameter Identification Method for Multiphase IM With Non-Sinusoidal Power Supply. *IEEE Access*, *10*. https://doi.org/10.1109/ACCESS.2022.3210125
- Liang, D., Zhu, Z. Q., Shao, B., Feng, J., Guo, S., Li, Y., & Zhao, A. (2022). Tracking of Winding and Magnet Hotspots in SPMSMs Based on Synergized Lumped-Parameter and Sub-Domain Thermal Models. *IEEE Transactions on Energy Conversion*, *37*(3). https://doi.org/10.1109/TEC.2022.3158017
- Liang, X. (2019). Temperature estimation and vibration monitoring for induction motors and the potential application in electrical submersible motors. *Canadian Journal of Electrical and Computer Engineering*, 42(3). https://doi.org/10.1109/CJECE.2018.2875111
- Liang, X., Ali, M. Z., & Zhang, H. (2020). Induction motors fault diagnosis using finite element method: A review. *IEEE Transactions on Industry Applications*, 56(2). https://doi.org/10.1109/TIA.2019.2958908
- Liang, Y., Zhao, F., Xu, K., Wang, W., Liu, J., & Yang, P. (2021). Analysis of Copper Loss of Permanent Magnet Synchronous Motor with Formed Transposition Winding. *IEEE Access*, 9. https://doi.org/10.1109/ACCESS.2021.3094833
- Liu, C. (2018). Emerging electric machines and drives An overview. *IEEE Transactions on Energy Conversion*, 33(4). https://doi.org/10.1109/TEC.2018.2852732

UNIVERSITI MALAYSIA PAHANG

- Liu, C., Gerada, D., Xu, Z., Chong, Y. C., Michon, M., Goss, J., Li, J., Gerada, C., & Zhang, H. (2021). Estimation of Oil Spray Cooling Heat Transfer Coefficients on Hairpin Windings with Reduced-Parameter Models. *IEEE Transactions on Transportation Electrification*, 7(2). https://doi.org/10.1109/TTE.2020.3031373
- Liu, Z., Xiang, Y., & Zhou, Y. (2021). Finite Element Modeling Method and Modal Analysis of a High Temperature Superconducting Motor. *IEEE Transactions on Applied Superconductivity*, 31(8). https://doi.org/10.1109/TASC.2021.3101765
- Ma, D., Li, J., Tian, B., Zhang, H., Li, M., & Pei, R. (2022). Studies on Loss of a Motor Stator Iron Core with High Silicon Electrical Steel Considering Temperature and Compressive

- Stress Factors. *Proceedings of 2022 IEEE 5th International Electrical and Energy Conference, CIEEC 2022.* https://doi.org/10.1109/CIEEC54735.2022.9846149
- Majdoubi, R., Masmoudi, L., Bakhti, M., Elharif, A., & Jabri, B. (2021). Parameters estimation of BLDC motor based on physical approach and weighted recursive least square algorithm. *International Journal of Electrical and Computer Engineering*, 11(1). https://doi.org/10.11591/ijece.v11i1.pp133-145
- Mathurin, T., Duchesne, S., & Parent, G. (2020). Assessment of Finite Element Simulation Methodologies for the Use of Paschen's Law in the Prediction of Partial Discharge Risk in Electrical Windings. *IEEE Access*, 8. https://doi.org/10.1109/ACCESS.2020.3013337
- Midya, M., Ganguly, P., Datta, T., & Chattopadhyay, S. (2023). ICA-Feature-Extraction-Based Fault Identification of Vehicular Starter Motor. *IEEE Sensors Letters*, 7(2). https://doi.org/10.1109/LSENS.2023.3242814
- Miloudi, H., Bendaoud, A., Miloudi, M., Dickmann, S., & Schenke, S. (2017). A novel method of transfer-function identification for modeling DM Impedance of AC motor. 2017 International Symposium on Electromagnetic Compatibility EMC EUROPE 2017, EMC Europe 2017. https://doi.org/10.1109/EMCEurope.2017.8094770
- Mitra, S., & Koley, C. (2023). Early and Intelligent Bearing Fault Detection Using Adaptive Superlets. *IEEE Sensors Journal*, 23(7). https://doi.org/10.1109/JSEN.2023.3245186

اونيؤرسيتي مليسيا فهغ السلطان عبدالله

- Mohammed, A., Melecio, J. I., & Djurovic, S. (2019). Stator winding fault thermal signature monitoring and analysis by in Situ FBG sensors. *IEEE Transactions on Industrial Electronics*, 66(10). https://doi.org/10.1109/TIE.2018.2883260
- Mokhlis, S. E., Sadki, S., & Bensassi, B. (2019). System Identification of a DC Servo Motor Using ARX and ARMAX Models. *Proceedings 2019 4th International Conference on Systems of Collaboration, Big Data, Internet of Things and Security, SysCoBIoTS 2019*. https://doi.org/10.1109/SysCoBIoTS48768.2019.9028015
- Naung, Y., Schagin, A., Oo, H. L., Ye, K. Z., & Khaing, Z. M. (2018). Implementation of data driven control system of DC motor by using system identification process. *Proceedings of the 2018 IEEE Conference of Russian Young Researchers in Electrical and Electronic Engineering*, ElConRus 2018, 2018-January. https://doi.org/10.1109/EIConRus.2018.8317455

- New Market Reports. (n.d.). Retrieved December 18, 2023, from https://www.marketsandmarkets.com/Market-Reports/electric-motor-marketalternative-fuel-vehicles
- Nguyen, N. T. (2018). Lyapunov stability theory. In *Advanced Textbooks in Control and Signal Processing* (Issue 9783319563923). https://doi.org/10.1007/978-3-319-56393-0_4
- Nise, N. S. (n.d.). Control systems engineering.
- Niu, G., Dong, X., & Chen, Y. (2023). Motor Fault Diagnostics Based on Current Signatures: A Review. In *IEEE Transactions on Instrumentation and Measurement* (Vol. 72). https://doi.org/10.1109/TIM.2023.3285999
- Ogata, Katsuhiko. (2010). Modern control engineering. Prentice-Hall.

يسبا فهع السلطان عبدالله

- Park, J. K., Jeong, C. L., Lee, S. T., & Hur, J. (2015). Early detection technique for stator winding inter-turn fault in BLDC motor using input impedance. *IEEE Transactions on Industry Applications*, 51(1). https://doi.org/10.1109/TIA.2014.2330067
- Park, S. H., Lee, E. C., Park, J. C., Hwang, S. W., & Lim, M. S. (2021). Prediction of Mechanical Loss for High-Power-Density PMSM Considering Eddy Current Loss of PMs and Conductors. *IEEE Transactions on Magnetics*, 57(2). https://doi.org/10.1109/TMAG.2020.3007439
- Patel, L., & Patel, T. (2019). Experimental Investigation and Performance Analysis of an Automobile Air Conditioning System. *Asian Journal For Convergence In Technology* (AJCT) ISSN -2350-1146, 4(3). https://asianssr.org/index.php/ajct/article/view/840
- Pawlus, W., Birkeland, J. T., Van Khang, H., & Hansen, M. R. (2017). Identification and Experimental Validation of an Induction Motor Thermal Model for Improved Drivetrain Design. *IEEE Transactions on Industry Applications*, 53(5). https://doi.org/10.1109/TIA.2017.2700283
- Pecinka, P., Kocman, S., Orsag, P., & Otypka, J. (2017). Solutions to increase the efficiency of induction motors. *Proceedings of the 2017 18th International Scientific Conference on Electric Power Engineering, EPE 2017*. https://doi.org/10.1109/EPE.2017.7967266
- Pescetto, P., Ferrari, S., Pellegrino, G., Carpaneto, E., & Boglietti, A. (2020). Winding Thermal Modeling and Parameters Identification for Multithree Phase Machines Based on Short-

- Time Transient Tests. *IEEE Transactions on Industry Applications*, 56(3). https://doi.org/10.1109/TIA.2020.2969643
- Phuc, P. N., Bozalakov, D., Vansompel, H., Stockman, K., & Crevecoeur, G. (2021). Rotor Temperature Virtual Sensing for Induction Machines Using a Lumped-Parameter Thermal Network and Dual Kalman Filtering. *IEEE Transactions on Energy Conversion*, 36(3). https://doi.org/10.1109/TEC.2021.3060478
- Pintelon, R., & Schoukens, J. (2012). System Identification: A Frequency Domain Approach, Second Edition. In *System Identification: A Frequency Domain Approach, Second Edition*. https://doi.org/10.1002/9781118287422
- Rasid, M. A. H., Zulkafli, M. N. A., & Nafiz, D. M. (2022). Evaluation of DC Machine Armature Winding Temperature Estimation Using Temperature Measured on Brush and Bearing. *1st IEEE Industrial Electronics Society Annual On-Line Conference, ONCON* 2022. https://doi.org/10.1109/ONCON56984.2022.10126816
- Ray, D. K., Roy, T., & Chattopadhyay, S. (2021). Skewness Scanning for Diagnosis of a Small Inter-Turn Fault in Quadcopter's Motor Based on Motor Current Signature Analysis. *IEEE Sensors Journal*, 21(5). https://doi.org/10.1109/JSEN.2020.3038786
- Rogel'berg, I. and B. V. (n.d.). Splavy dlya termopar: sprav.[Alloys for thermocouples. Handbook]. Moscow: Metallurgiya; 1983. 360 p. Russ.
- Rusu-Zagar, C., Notingher, P., Navrapescu, V., Mares, G., Gilda, R.-Z., Setnescu, T., & Setnescu, R. (2013). Method for estimating the lifetime of electric motors insulation. In 2013 8th
 - International Symposium on Advanced Topics in Electrical Engineering, ATEE 2013. https://doi.org/10.1109/ATEE.2013.6563466
- Sadeq, T., & Wai, C. K. (2019). Model the DC-DC Converter with Supercapacitor Module based on System Identification. 2019 IEEE International Conference on Automatic Control and Intelligent Systems, I2CACIS 2019 Proceedings. https://doi.org/10.1109/I2CACIS.2019.8825095
- Seol, H. S., Kang, D. W., Jun, H. W., Lim, J., & Lee, J. (2017). Design of Winding Changeable BLDC Motor Considering Demagnetization in Winding Change Section. *IEEE Transactions on Magnetics*, *53*(11). https://doi.org/10.1109/TMAG.2017.2695890

- Seung, M., Choi, W., Hur, S., & Kwon, I. (2022). Cold Junction Compensation Technique of Thermocouple Thermometer Using Radiation-Hardened-by-Design Voltage Reference for Harsh Radiation Environment. *IEEE Transactions on Instrumentation and Measurement*, 71. https://doi.org/10.1109/TIM.2022.3205931
- Sharveswaran, A., & Nirmal, U. (2020). Research Development on Wiper Mechanism in Automotive Application: A Critical Review. *Current Journal of Applied Science and Technology*. https://doi.org/10.9734/cjast/2020/v39i3531064
- Sheikh, M. A., Bakhsh, S. T., Irfan, M., Nor, N. bin M., & Nowakowski, G. (2022). A Review to Diagnose Faults Related to Three-Phase Industrial Induction Motors. *Journal of Failure Analysis and Prevention*, 22(4). https://doi.org/10.1007/s11668-022-01445-2
- Shen, M., Pfister, P. D., Tang, C., & Fang, Y. (2021). A Hybrid Model of Permanent-Magnet Machines Combining Fourier Analytical Model with Finite Element Method, Taking Magnetic Saturation into Account. *IEEE Transactions on Magnetics*, 57(2). https://doi.org/10.1109/TMAG.2020.3005802
- Shifat, T. A., & Hur, J. W. (2020). An Effective Stator Fault Diagnosis Framework of BLDC Motor Based on Vibration and Current Signals. *IEEE Access*, 8. https://doi.org/10.1109/ACCESS.2020.3000856
- Shih, K. J., Hsieh, M. F., Chen, B. J., & Huang, S. F. (2022). Machine Learning for Inter-Turn Short-Circuit Fault Diagnosis in Permanent Magnet Synchronous Motors. *IEEE Transactions on Magnetics*, 58(8). https://doi.org/10.1109/TMAG.2022.3169173

MALAYSIA PAHANG

- Shubita, R. R., Alsadeh, A. S., & Khater, I. M. (2023). Fault Detection in Rotating Machinery Based on Sound Signal Using Edge Machine Learning. *IEEE Access*, 11. https://doi.org/10.1109/ACCESS.2023.3237074
- Siraj, F. M., Ayon, S. T. K., Samad, M. A., Uddin, J., & Choi, K. (2024). Few-Shot Lightweight SqueezeNet Architecture for Induction Motor Fault Diagnosis Using Limited Thermal Image Dataset. *IEEE Access*, 12, 50986–50997. https://doi.org/10.1109/ACCESS.2024.3385430
- Staton, D. A., & Cavagnino, A. (2006). Convection heat transfer and flow calculations suitable for analytical modelling of electric machines. *IECON Proceedings (Industrial Electronics Conference)*. https://doi.org/10.1109/IECON.2006.348143

- Stone, G. C., Culbert, I. M., & Lloyd, B. A. (2007). Stator insulation problems associated with low voltage and medium voltage PWM drives. 2007 IEEE Cement Industry Technical Conference Record. https://doi.org/10.1109/CITCON.2007.358997
- Straka, M., Mares, M., & Horejs, O. (2021). The impact of key temperature measuring points on thermal error compensation model transfer between milling centers of the same product line. *MM Science Journal*, 2021-November. https://doi.org/10.17973/MMSJ.2021_11_2021173
- Sundararajan, R., Natarajan, V., Viswanathan, V., & Shankar, S. H. R. (2022). Automatic Temperature Control of Electric Motor Using PIC Microcontroller. 2022 IEEE Delhi Section Conference, DELCON 2022. https://doi.org/10.1109/DELCON54057.2022.9752892
- Tallam, R. M., Lee, S. Bin, Stone, G. C., Kliman, G. B., Yoo, J., Habetler, T. G., & Harley, R. G. (2007). A survey of methods for detection of stator-related faults in induction machines. IEEE Transactions on Industry Applications, 43(4). https://doi.org/10.1109/TIA.2007.900448
- Upadhyay, A., Alakula, M., & Marquez-Fernandez, F. J. (2019). Characterization of Onboard Condition Monitoring Techniques for Stator Insulation Systems in Electric Vehicles A Review. *IECON Proceedings (Industrial Electronics Conference)*, 2019-October. https://doi.org/10.1109/IECON.2019.8926678
- Vaseghi, B., Nahid-Mobarakh, B., Takorabet, N., & Meibody-Tabar, F. (2011). Inductance identification and study of PM motor with winding turn short circuit fault. *IEEE Transactions on Magnetics*, 47(5). https://doi.org/10.1109/TMAG.2010.2083639
- Wang, E., Grabherr, P., Wieske, P., & Doppelbauer, M. (2022). A Low-Order Lumped Parameter Thermal Network of Electrically Excited Synchronous Motor for Critical Temperature Estimation. 2022 International Conference on Electrical Machines, ICEM 2022. https://doi.org/10.1109/ICEM51905.2022.9910939
- Wang, X., Wang, X., Lu, S., Lu, S., Lu, S., & Zhang, S. (2020). Rotating angle estimation for hybrid stepper motors with application to bearing fault diagnosis. *IEEE Transactions on Instrumentation and Measurement*, 69(8). https://doi.org/10.1109/TIM.2019.2963582
- Wang, X., Zhou, S., Wu, L., Zhao, M., & Hu, C. (2019). Iron Loss and Thermal Analysis of High Speed PM motor Using Soft Magnetic Composite Material. 2019 22nd International Conference on Electrical Machines and Systems, ICEMS 2019. https://doi.org/10.1109/ICEMS.2019.8922504

- Wockinger, D., Bramerdorfer, G., Drexler, S., Vaschetto, S., Cavagnino, A., Tenconi, A., Amrhein, W., & Jeske, F. (2023). Measurement-Based Identification of Lumped Parameter Thermal Networks for sub-Kw Outer Rotor PM Machines. *IEEE Transactions on Industry Applications*, 59(1). https://doi.org/10.1109/TIA.2022.3217029
- Wrobel, R., Vainel, G., Copeland, C., Duda, T., Staton, D., & Mellor, P. H. (2015). Investigation of Mechanical Loss Components and Heat Transfer in an Axial-Flux PM Machine. *IEEE Transactions on Industry Applications*, 51(4). https://doi.org/10.1109/TIA.2015.2405499
- Wu, H., & Dobson, I. (2012). Cascading stall of many induction motors in a simple system. *IEEE Transactions on Power Systems*, 27(4). https://doi.org/10.1109/TPWRS.2012.2189420
- Xu, H., Lin, K., Ehrenpreis, C., Roux, G., & De Doncker, R. W. (2020). Thermal Modeling of Electrical Machines with Advanced Fluid Cooling. *InterSociety Conference on Thermal and Thermomechanical Phenomena in Electronic Systems, ITHERM*, 2020-July. https://doi.org/10.1109/ITherm45881.2020.9190944
- Xu, Z., Tang, G., & Pang, B. (2022). An Infrared Thermal Image Few-Shot Learning Method Based on CAPNet and Its Application to Induction Motor Fault Diagnosis. *IEEE Sensors Journal*, 22(16). https://doi.org/10.1109/JSEN.2022.3192300
- Yang, C., Zhang, Y., & Qiu, H. (2019). Influence of Output Voltage Harmonic of Inverter on Loss and Temperature Field of Permanent Magnet Synchronous Motor. *IEEE Transactions on Magnetics*, 55(6). https://doi.org/10.1109/TMAG.2019.2899468

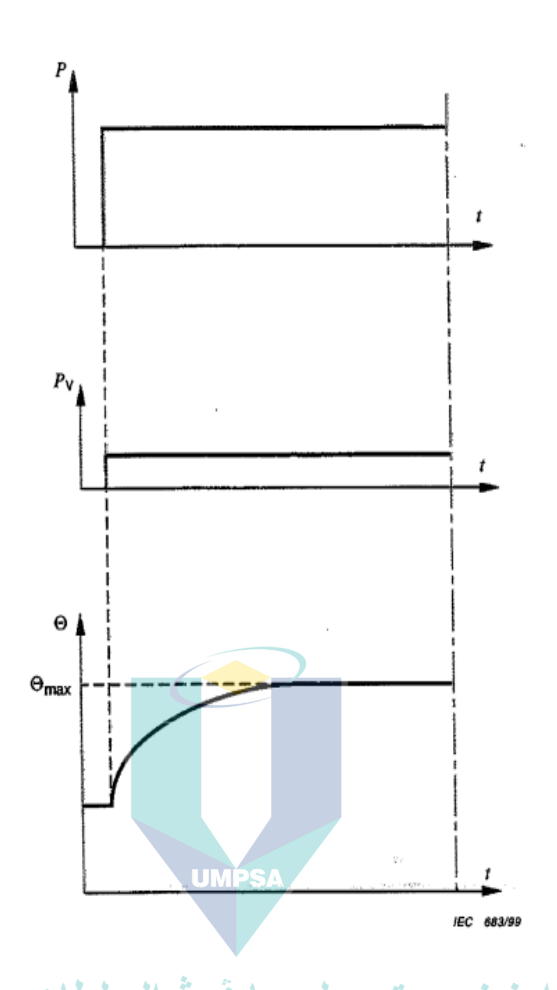
UNIVERSITI MALAYSIA PAHANG

- Yatsugi, K., Pandarakone, S. E., Mizuno, Y., & Nakamura, H. (2023). Common Diagnosis Approach to Three-Class Induction Motor Faults Using Stator Current Feature and Support Vector Machine. *IEEE Access*, 11. https://doi.org/10.1109/ACCESS.2023.3254914
- Yu, J., Kim, K., & Yi, K. (2019). Development of a hardware-in-the-loop simulation system for power seat and power trunk electronic control unit validation. *Proceedings of the Institution of Mechanical Engineers, Part D: Journal of Automobile Engineering*, 233(3). https://doi.org/10.1177/0954407017751951
- Yu, W., Hua, W., Zhang, Z., Wu, Z., Wang, P., & Xia, W. (2022). Comparative Analysis of AC Copper Loss With Round Copper Wire and Flat Copper Wire of High-Speed Stator-PM Flux-Switching Machine. *IEEE Transactions on Industry Applications*, 58(6). https://doi.org/10.1109/TIA.2022.3194042

- Zanelli, A., Kullick, J., Eldeeb, H. M., Frison, G., Hackl, C. M., & Diehl, M. (2022). Continuous Control Set Nonlinear Model Predictive Control of Reluctance Synchronous Machines. *IEEE Transactions on Control Systems Technology*, 30(1). https://doi.org/10.1109/TCST.2020.3043956
- Zeng, L., Li, X., He, X., Li, G., Wang, Z., & Bao, H. (2014). Key factors on the accuracy of measurement temperature by using infrared thermometer. *ICRMS 2014 Proceedings of 2014 10th International Conference on Reliability, Maintainability and Safety: More Reliable Products, More Secure Life*. https://doi.org/10.1109/ICRMS.2014.7107311
- Zhang, H. (2015). Online Thermal Monitoring Models for Induction Machines. *IEEE Transactions on Energy Conversion*, 30(4). https://doi.org/10.1109/TEC.2015.2431444
- Zhang, P., Du, Y., & Habetler, T. G. (2010). A transfer-function-based thermal model reduction study for induction machine thermal overload protective relays. *IEEE Transactions on Industry Applications*, 46(5), 1919–1926. https://doi.org/10.1109/TIA.2010.2058831
- Zhang, P., Du, Y., Habetler, T. G., & Lu, B. (2011). A survey of condition monitoring and protection methods for medium-voltage induction motors. In *IEEE Transactions on Industry Applications* (Vol. 47, Issue 1). https://doi.org/10.1109/TIA.2010.2090839
- Zhang, Q. (1997). Using wavelet network in nonparametric estimation. *IEEE Transactions on Neural Networks*, 8(2). https://doi.org/10.1109/72.557660
- اونيۇرسىتى ملىسىيا قەغ السلطان عبدالله
- Zhang, Q., Deng, J., & Fu, N. (2019). Minimum Copper Loss Direct Torque Control of Brushless DC Motor Drive in Electric and Hybrid Electric Vehicles. *IEEE Access*, 7. https://doi.org/10.1109/ACCESS.2019.2927416
- Zhao, H., Xiong, B., & Li, Z. (2022). Three-dimensional Transient Temperature Rise Calculation of Induction Motor under Overload Condition. 2022 International Conference on Electrical Machines and Systems, ICEMS 2022. https://doi.org/10.1109/ICEMS56177.2022.9983124



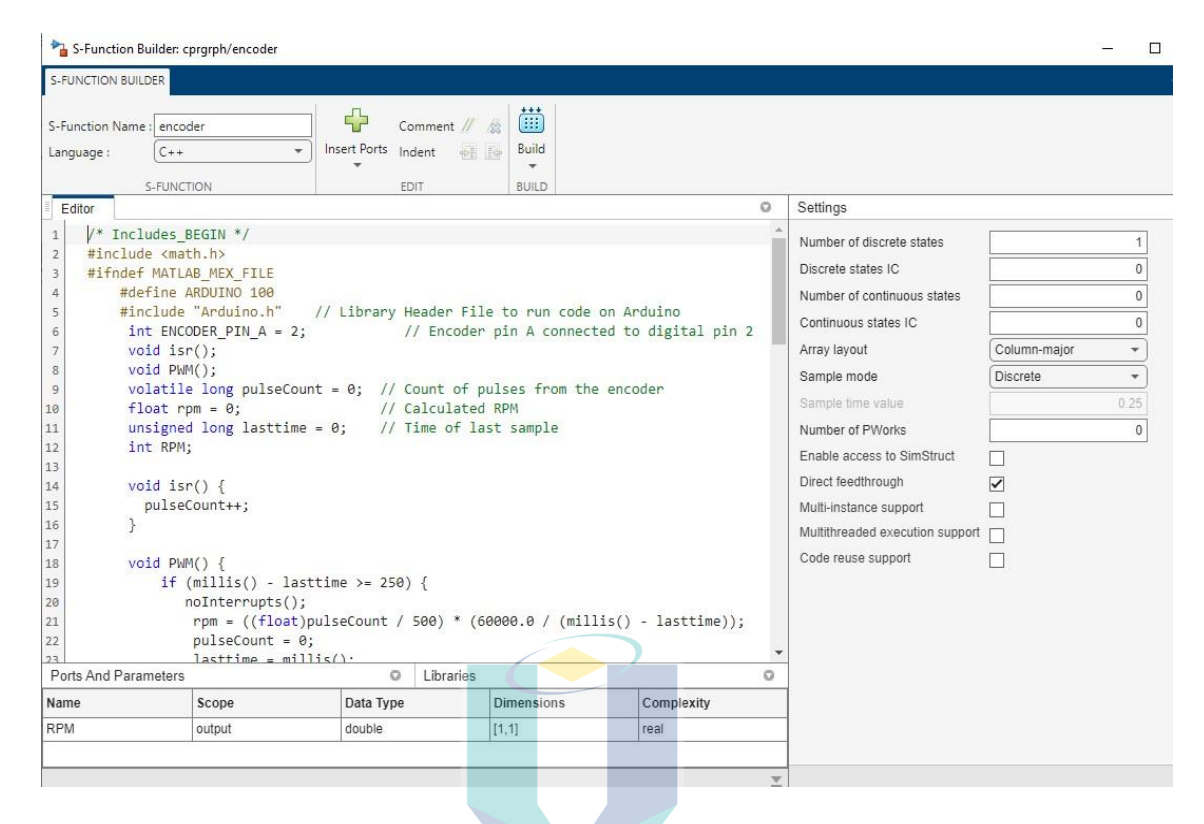
Appendix A: IEC Electric machines Duty Cycle



Continuous Duty Cycle.

Where P is load, P_v is electrical losses, θ is temperature, θ_{max} is maximum temperature attained and t is time.

Appendix B: Simulink Block Diagram.

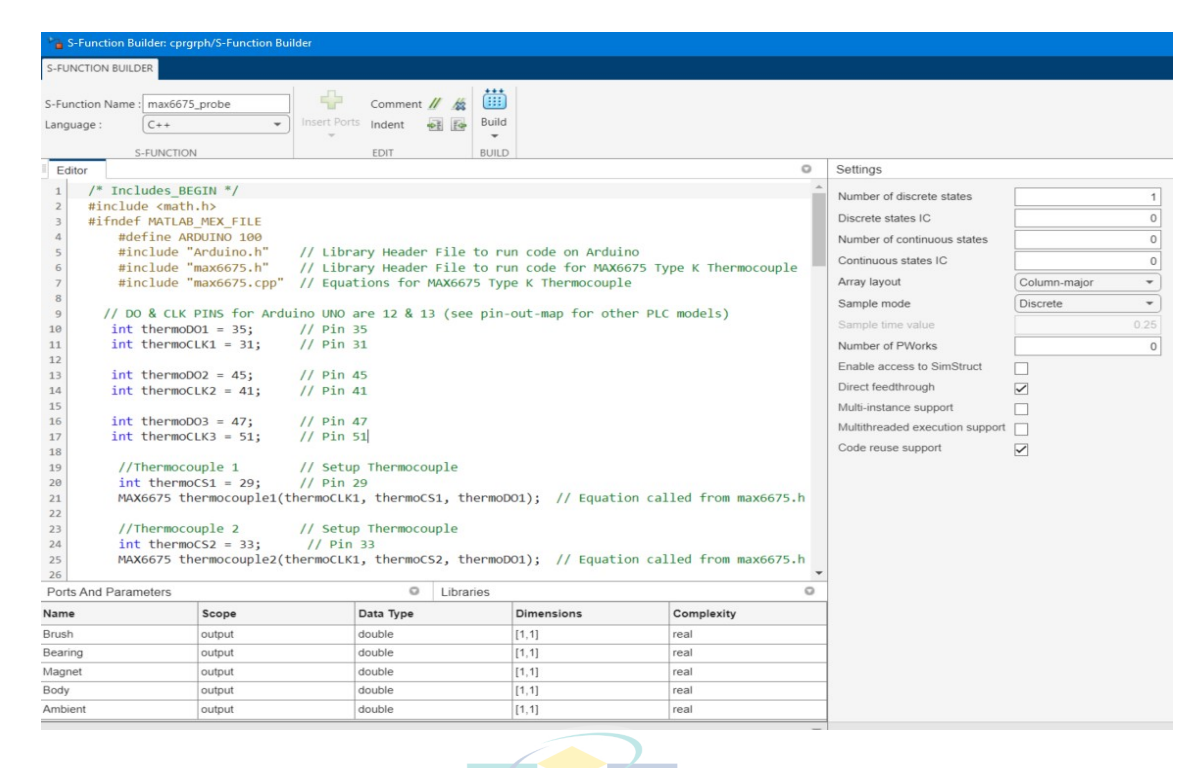


Encoder setup in s-function builder.

```
Encoder Code
```

```
/* Includes END */
#include<math.h>
او نيور سيتي مليسيا فهغ السلطان#ifndef MATLAB_MEX_FILE
#define ARDUINO 100 VERSITI MALAYSIA PAHANG
#define "Arduino.h" //Library header to run on Arduino
int ENCODER_PIN_A=2; //Encoder pin A connect to pin 2
void isr();//Declare function pulse counting positive only
void PWM();//Declare function encoder read
volatile long pulseCount=0; //Initial value pulse
float rpm=0;//Initial value RPM
unsigned long lasttime=0;//Time of last sample
int RPM;//Declare RPM
void isr(){//Function pulse counting positive only
pulseCount++;
}
void PWM(){//Function encoder read
if (millis()-lastime >=250){
      noInterrupts();
      rpm=((float)pulseCount/500)*(60000.0/millis()-lasttime));
      pulseCount=0;
      lasttime=millis();
      interrupts();
```

```
rpm;
      }
}
#endif
/* Includes_END */
/* Externs_END */
void encoder_Start_wrapper(real_T *xD)
/* Start_BEGIN */
/* Start_END */
void encoder_Outputs_wrapper(real_T *RPM,
                          const real_T *xD)
{
/* Output BEGIN */
if(xD[0] == 1) // void loop()
{
    #ifndef MATLAB_MEX_FILE// basic readout test, just print the current temp
    PWM();
    RPM[0] = rpm;
    #endif
/* Output_END */
void encoder_Update_wrapper(real_T *RPM,
                            real_T *xD)
/* Update_BEGIN */
if(xD[0] != 1) // void setup()
                               اونبؤر سبتي ملبسيا فهغ
{
    #ifndef MATLAB_MEX_FILE// use Arduino pins PAHANC
        pinMode(ENCODER_PIN_A, INPUT);
        attachInterrupt(digitalPinToInterrupt(ENCODER_PIN_A), isr, RISING);
    #endif//done with initialization
   xD[0] = 1;
/* Update_END */
void encoder_Terminate_wrapper(real_T *xD)
/* Terminate BEGIN */
/* Terminate_END */
}
```

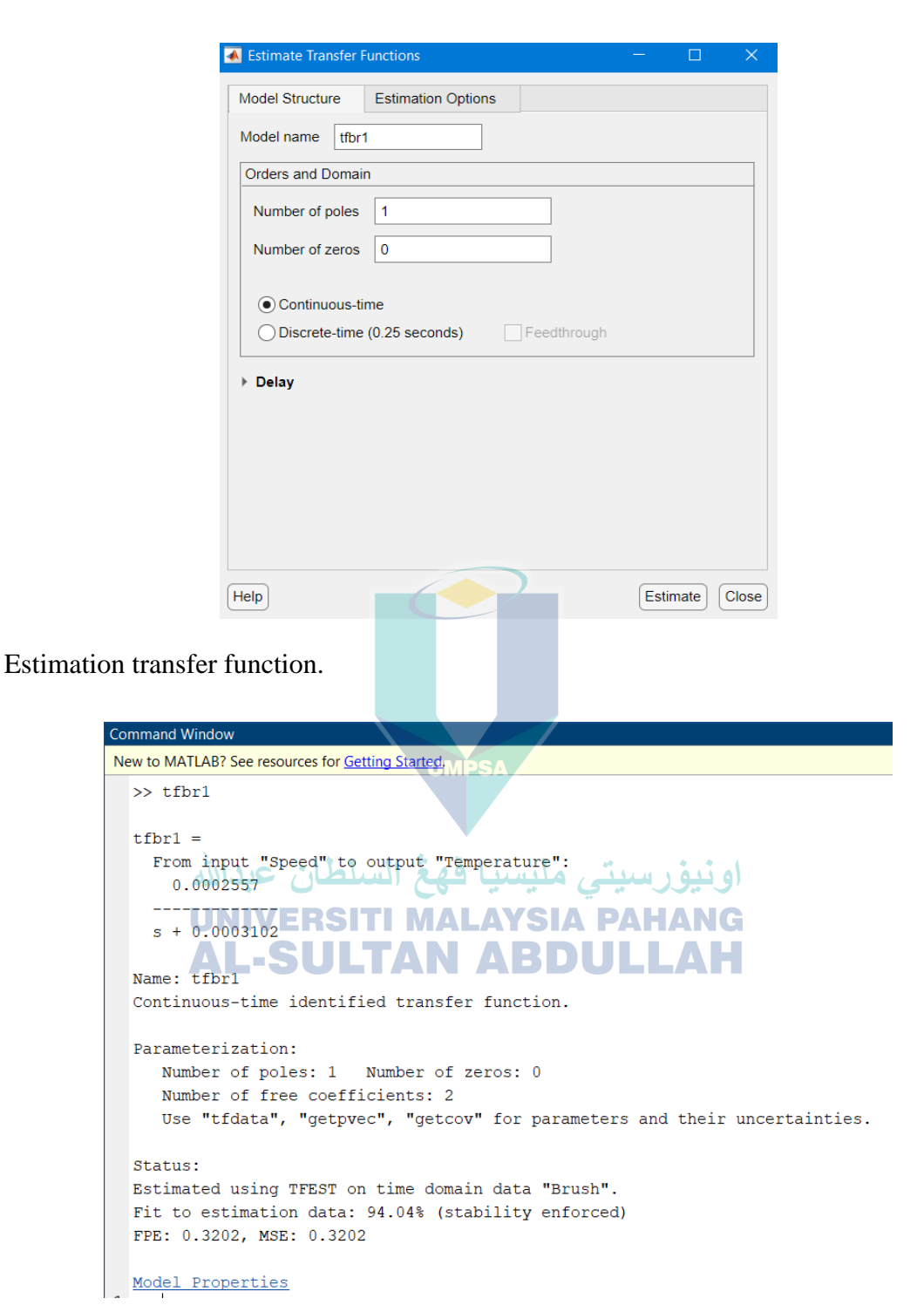


MAX6675 setup in s-function builder.

```
MAX6675 Code
/* Includes_BEGIN */
 #include <math.h>
 #ifndef MATLAB MEX FILE
 #define ARDUINO 100
 #include "Arduino.h"//Library header file to run code on Arduino
 #include "max6675.h"// Library header file to run MAX6675
 #include "max6675.cpp"//Equations for MAX6675 type K thermocouple
   int thermoDO1 = 35;// Pin 35 MALAYSIA PAHANG
   int thermoCLK1 = 31;// Pin 31
   int thermoDO2 = 45;// Pin 45 N ABDULLAH
   int thermoCLK2 = 41;// Pin 41
   int thermoDO3 = 47;// Pin 47
   int thermoCLK3 = 51;// Pin 51
   int thermoCS3 = 29;// Pin 29 Thermocouple 1
   MAX6675 thermocouple3(thermoCLK2, thermoCS3, thermoDO2);
   int thermoCS3 = 33;// Pin 33 Thermocouple 2
   MAX6675 thermocouple3(thermoCLK2, thermoCS3, thermoDO2);
   int thermoCS4 = 39;// Pin 39 Thermocouple 3
   MAX6675 thermocouple4(thermoCLK2, thermoCS4, thermoDO2);
   int thermoCS4 = 43;// Pin 43 Thermocouple 4
   MAX6675 thermocouple4(thermoCLK2, thermoCS4, thermoDO2);
   int thermoCS5 = 49;// Pin 49 Thermocouple 5
   MAX6675 thermocouple5(thermoCLK3, thermoCS5, thermoDO3);
#endif
/* Includes END */
/* Externs_END */
```

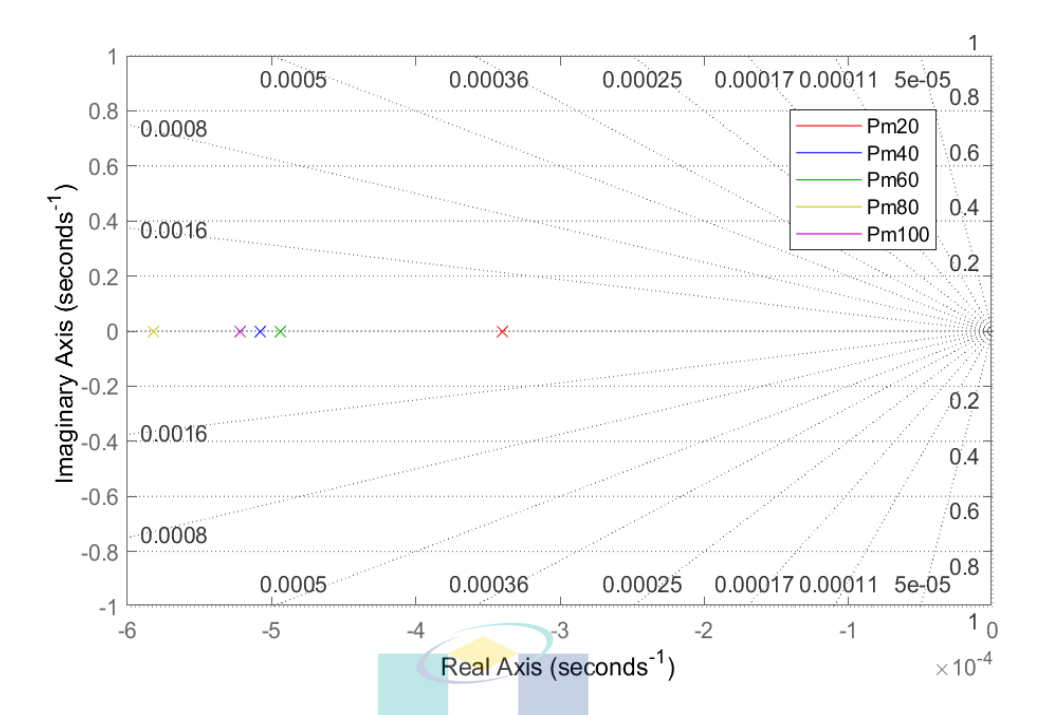
```
void max6675_probe_Start_wrapper(real_T *xD)
/* Start BEGIN */
/* Start END */
void max6675_probe_Outputs_wrapper(real_T *Brush,
                                   real_T *Bearing,
                                   real_T *Magnet,
                                   real_T *Body,
                                   real_T *Ambient,
                                   const real_T *xD)
/* Output_BEGIN */
if(xD[0] == 1) // void loop()
{
    #ifndef MATLAB_MEX_FILE// basic readout test, just print the current temp
        Brush[0]=thermocouple1.readcelsius();//Thermocouple1
        Bearing[0]=thermocouple2.readcelsius();//Thermocouple2
        Magnet[0]=thermocouple3.readcelsius();//Thermocouple3
        Body[0]=thermocouple4.readcelsius();//Thermocouple4
        Ambient[0]=thermocouple5.readcelsius();//Thermocouple5
    #endif
}
/* Output END */
void max6675_probe_Update_wrapper(real_T *Brush, real_T *Bearing, real_T
*Magnet,
                                  real_T *Ambient,
              (real_T *xD ملسباً فهغُ السلطان عبدالله
                                  اونيۇرسىيتى مليس<del>ي</del>ا <u>ھ</u>ھ
/* Update_BEGINJ*/IVERSITI MALAYSIA PAHANG
if(xD[0] != 1) // void setup() A B D U L A H
{
    #ifndef MATLAB_MEX_FILE// use Arduino pins
        pinMode(thermoCS1,OUTPUT);digitalWrite(thermoCS1,HIGH);
        pinMode(thermoCS2,OUTPUT);digitalWrite(thermoCS2,HIGH);
        pinMode(thermoCS3,OUTPUT);digitalWrite(thermoCS3,HIGH);
        pinMode(thermoCS4,OUTPUT);digitalWrite(thermoCS4,HIGH);
        pinMode(thermoCS5,OUTPUT);digitalWrite(thermoCS5,HIGH);
    #endif//done with initialization
    xD[0] = 1;
/* Update_END */
void max6675 probe Terminate wrapper(real T *xD)
/* Terminate_BEGIN */
/* Terminate_END */
```

Appendix C: System Identification Toolbox.

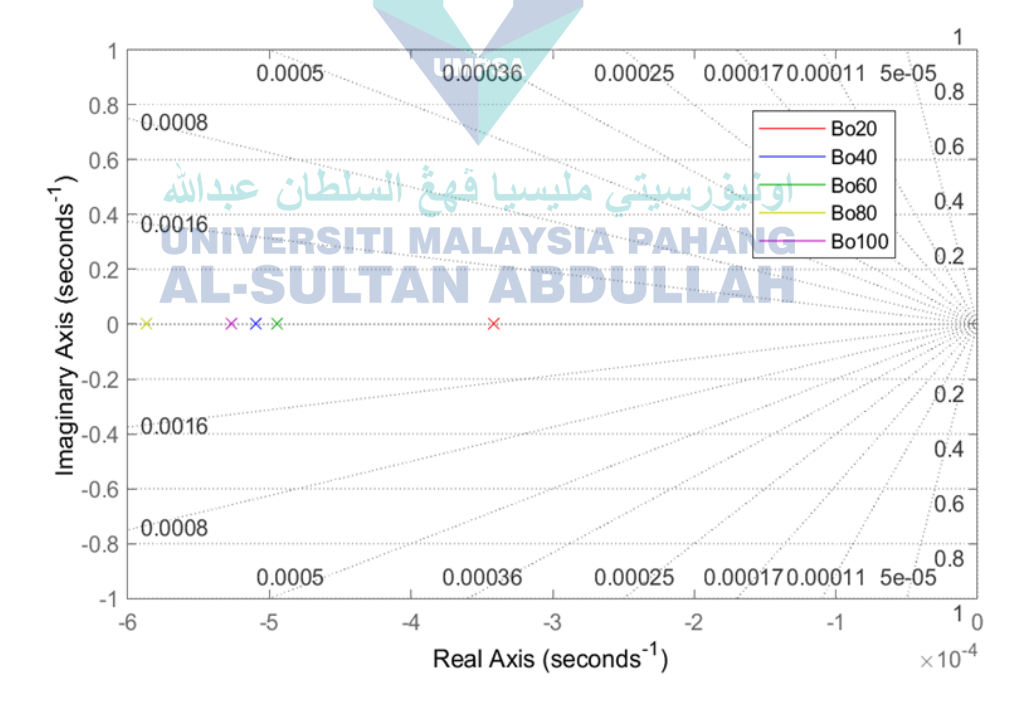


Result estimation of transfer function.

Appendix D: System Linearity.



S-plane graph of permanent magnet.



S-plane graph of casing.

Appendix E: Calculation for Averaged-pole Transfer Function.

Transfer function for brush at varying speed.

$$G_{brush \ 20\%}(s) = \frac{K}{(s + \sigma_1)(s + \sigma_2)(s + \sigma_3)}$$

$$G_{brush \ 20\%}(s) = \frac{2.671e - 9}{(s^3 + 4.09e - 3)(s^2 + 1.18e - 5)(s + 3.223e - 9)}$$

$$[Z_{\text{brush 20}}, \sigma_{\text{brush 20}}, K_{\text{brush 20}}] = tf2zp(Z_{\text{brush 20}}(s), \sigma_{\text{brush 20}}(s))$$

$$\begin{split} [Z_{\text{br}\,20}, \sigma_{\text{br}\,20}, K_{\text{br}\,20}] \\ &= tf2zp(2.671e-9, [1,4.09e-3,1.18e-5,3.223e-9]) \end{split}$$

$$\begin{split} \sigma_{\rm br1\,20} = & -1.9e - 3 + 2.7e - 3, \sigma_{\rm br1\,40} = -2.1e - 3 + 3.5e - 3, \\ \sigma_{\rm br1\,60} = & -4.0e - 3 + 5.2e - 3, \sigma_{\rm br1\,80} = -3.8e - 3 + 6.0e - 4 \\ \sigma_{\rm br1\,100} = & -4.0e - 3 \end{split}$$

$$K_{\rm br20} = 2.8e - 9, K_{\rm br40} = 4.2e - 9, K_{\rm br60} = 7.5e - 9, K_{\rm br80} = 1.9e - 9$$

$$K_{\rm br100} = 6.7e - 10$$

$$\begin{split} \sigma_{1\ brush} &= [(\sigma_{1\ 20} + \sigma_{1\ 40} + \cdots + \sigma_{1\ 100})/5] = -3.2\text{e}-3 + 2.4\text{e}-3\text{i} \\ \sigma_{2\ brush} &= [(\sigma_{2\ 20} + \sigma_{2\ 40} + \cdots + \sigma_{2\ 100})/5] = -2.8\text{e}-3 + 2.4\text{e}-3\text{i} \\ \sigma_{3\ brush} &= [(\sigma_{3\ 20} + \sigma_{3\ 40} + \cdots + \sigma_{3\ 100})/5] = -4.8\text{e}-4 \end{split}$$

$$K_{brush} = [(K_{20} + K_{40} + \dots + K_{100})/5] = 3.4e-9$$

 $Z_{brush} = 0$

$$[\bar{Z}_{brush}(s), \bar{\sigma}_{brush}(s)] = zp2tf(Z_{brush}, \sigma_{(1,2,3)brush}, K_{brush})$$

$$G_{brush}(s) = \frac{\overline{K}}{(s + \overline{\sigma_1})(s + \overline{\sigma_2})(s + \overline{\sigma_3})}$$

$$G_{brush}(s) = \frac{3.37e - 9}{(s^3 + 6.4e - 3)(s^2 + 1.7e - 5)(s + 7.0e - 9)}$$

Transfer function for bearing at varying speed.

$$G_{bearing}(s) = \frac{K}{(s+\sigma)}$$

$$G_{bearing\ 20\%}(s) = \frac{1.4e-4}{s+3.3e-4}$$

 $\left[Z_{\text{bearing 20}}, \sigma_{\text{bearing 20}}, K_{\text{bearing 20}}\right] = tf2zp(Z_{\text{bearing 20}}(s), \sigma_{\text{bearing 20}}(s))$

$$[Z_{\text{be 20}}, \sigma_{\text{be 20}}, K_{\text{be 20}}] = tf2zp(1.4e-4, [1,3.3e-4])$$

$$\sigma_{\text{be }20} = -0.33e - 3$$
, $\sigma_{\text{be }40} = -0.5e - 3$, $\sigma_{\text{be }60} = -0.49e - 3$, $\sigma_{\text{be }80} = -0.58e - 3$, $\sigma_{\text{be }100} = -0.52e - 3$

$$K_{\text{be20}} = 0.14e - 3, K_{\text{be40}} = 0.16e - 3, K_{\text{be60}} = 0.12e - 3,$$

$$K_{\text{be80}} = 0.10, e - 3, K_{\text{be100}} = 0.06e - 3$$

$$\sigma_{bearing} = [(\sigma_{20} + \sigma_{40} + \dots + \sigma_{100})/5] = -4.9e-4$$

$$K_{bearing} = [(K_{20} + K_{40} + \dots + K_{100})/5] = 1.2e-4$$

$$Z_{bearing} = 0$$

اونيؤرسيتي مليسيا فهغ السلطان عبدالله

 $\left[\bar{Z}_{bearing}\left(s\right), \bar{\sigma}_{bearing}\left(s\right)\right] = zp2tf(Z_{bearing}, \sigma_{bearing}, K_{bearing})$

$$G_{bearing}(s) = \frac{\overline{K}}{s + \overline{\sigma}}$$

$$G_{bearing}(s) = \frac{1.2e-4}{s+4.9e-4}$$

Transfer function for permanent magnet at varying speed.

$$G_{permanent\ magnet}(s) = \frac{K}{(s+\sigma)}$$

$$G_{permanent\ magnet\ 20\%}(s) = \frac{1.4e-4}{s+3.4e-4}$$

$$[Z_{\text{p.m 20}}, \sigma_{\text{p.m 20}}, K_{\text{p.m 20}}] = tf2zp(Z_{\text{p.m 20}}(s), \sigma_{\text{p.m 20}}(s))$$

$$[Z_{\text{p.m }20}, \sigma_{\text{p.m }20}, K_{\text{p.m }20}] = tf2zp(1.4e-4, [1,3.4e-4])$$

$$\sigma_{\text{p.m 20}} = -0.34e - 3, \sigma_{\text{p.m 40}} = -0.5e - 3, \sigma_{\text{p.m 60}} = -0.49e - 3,$$

$$\sigma_{\text{p.m 80}} = -0.58e - 3, \sigma_{\text{p.m 100}} = -0.52e - 3$$

$$K_{\text{p.m20}} = 0.14e-3, K_{\text{p.m40}} = 0.16e-3, K_{\text{p.m60}} = 0.12e-3,$$

$$K_{\text{p.m80}} = 0.10e-3, K_{\text{p.m100}} = 0.06e-3$$

$$\sigma_{\text{p.magnet}} = [(\sigma_{20} + \sigma_{40} + \dots + \sigma_{100})/5] = -4.8e-4$$

$$K_{p.magnet} = [(K_{20} + K_{40} + \dots + K_{100})/5] = 1.2e-4$$

$$Z_{p.magnet} = 0$$

 $\left[\bar{Z}_{p.magnet}(s), \bar{\sigma}_{p.magnet}(s)\right] = zp2tf(Z_{p.magnet}, \sigma_{p.magnet}, K_{p.magnet})$

$$G_{p.magnet}(s) = \frac{\overline{K}}{s + \overline{\sigma}}$$

$$G_{p.magnet}(s) = \frac{1.2e-4}{s+4.8e-4}$$

$$G_{p.magnet}(s) = \frac{1.2e-4}{s+4.8e-4}$$

Transfer function for casing at varying speed. SIA PAHANG

AL-SULTAN ARBULLAH $G_{casing}(s) = \frac{ARBULLAH}{(s+\sigma)}$

$$G_{casing\ 20\%}(s) = \frac{1.4e-4}{s+3.4e-4}$$

$$[Z_{\rm cs\,20},\sigma_{\rm cs\,20},K_{\rm cs\,20}]=tf2zp(Z_{\rm cs\,20}(s),\sigma_{\rm cs\,20}(s))$$

$$[Z_{\rm cs\,20},\sigma_{\rm cs\,20},K_{cs\,20}]=tf2zp(1.5e\!-\!4,[1,\!3.4e\!-\!4])$$

$$\sigma_{\text{cs }20} = -0.34e - 3, \sigma_{\text{cs }40} = -0.51e - 3, \sigma_{\text{cs }60} = -0.49e - 3,$$

$$\sigma_{\text{cs }80} = -0.58e - 3, \sigma_{\text{cs }100} = -0.52e - 3$$

$$\begin{split} K_{cs20} &= 0.14e - 3, K_{cs40} = 0.16e - 3, K_{cs60} = 0.12e - 3, \\ K_{cs80} &= 0.10e - 3, K_{cs100} = 0.05e - 3 \end{split}$$

$$\sigma_{casing} = \left[(\sigma_{20} + \sigma_{40} + \dots + \sigma_{100})/5 \right] = -4.9e - 4$$

$$K_{casing} = \left[(K_{20} + K_{40} + \dots + K_{100})/5 \right] = 1.1e - 4$$

$$Z_{casing} = 0$$

 $\left[\bar{Z}_{casing}\left(s\right),\bar{\sigma}_{casing}(s)\right]=zp2tf(Z_{casing},\sigma_{casing},K_{casing})$

$$G_{casing}(s) = rac{\overline{K}}{s + \overline{\sigma}}$$
 $G_{casing}(s) = rac{1.1e - 4}{s + 4.9e - 4}$

اونيؤرسيتي مليسيا قهڠ السلطان عبدالله UNIVERSITI MALAYSIA PAHANG AL-SULTAN ABDULLAH Appendix F: Calculation for Variable-pole Transfer Function.

Transfer function for brush at varying speed.

Brush real number $\sigma_{brush}(N)$ @ Numerator. Coefficient exponential:

$$a1 = 5.6e - 4$$
, $b1 = 1.3e - 2$, $c1 = -1.8e - 3$, $d1 = 9.0e - 3$

$$a2 = 6.9e - 4$$
, $b2 = 1.4e - 2$, $c1 = -2.0e - 3$, $d1 = 9.9e - 3$

Coefficient polynomial 2:

$$a3 = 1.3e - 8$$
, $b3 = -4.8e - 6$, $c3 = -1.1e - 4$

Brush complex number $\sigma_{brush}i(N)$.

Coefficient polynomial 2:

$$a1i = -2.0e - 7$$
, $b1i = 4.7e - 5$, $c1 = 7.7e - 4$

$$a2i = 2.0e - 7$$
, $b2 = -4.7e - 5$, $c1 = -7.7e - 4$

Gain $K_{brush}(N)$ @ Denominator.

Coefficient polynomial 2:

$$p1 = -2.6e - 13, p2 = 6.9e - 11, p3 = -1.9e - 10$$

$$N = sneed$$

$$\sigma_{1brush}(N) = a1 * \exp(b1 * N) + c1 * \exp(d1 * N)$$

$$\sigma_{2brush}(N) = a2 * \exp(b2 * N) + c2 * \exp(d2 * N)$$

$$\sigma_{3brush}(N) = a3 * N^2 + b3 * N + c3$$

$$\sigma_{1brush}i(N) = a1i*N^2 + b1i*N + c1i$$

$$\sigma_{2brush}i(N) = a1i*N^2 + b1i*N + c1i$$

$$\sigma_{3brush}i(N) = 0$$

$$Z_{hrush}(N) = 0$$

$$\begin{split} \sigma_{brush}(N) &= \left[\sigma_{1br}(N) + \sigma_{1br}i(N) * i, \sigma_{2br}(N) + \sigma_{2br}i(N) * i, \right. \\ &\left. \sigma_{3br}(N) + \sigma_{3br}i(N) * i \right] \end{split}$$

$$K_{brush}(N) = p1 * N^2 + p2 * N + p3$$

$$[Z_{brush}(s), \sigma_{brush}(s)] = zp2tf(Z_{brush}(N), \sigma_{brush}(N), K_{brush}(N))$$

$$G_k(s) = \frac{K_{brush}(N)}{(s + \sigma_{brush1}(N))(s + \sigma_{brush2}(N))(s + \sigma_{brush3}(N))}$$

$$\sigma_{\text{brush 1}}(N) = s + \sigma_{\text{brush 1}}(N)$$

$$\sigma_{\text{brush 2}}(N) = s + \sigma_{\text{brush2}}(N)$$

$$\sigma_{\text{brush }3}(N) = s + \sigma_{\text{brush}3}(N)$$

$$K_{\text{brush}}(N) = K_{brush}(N)$$

Transfer function for bearing at varying speed.

Pole $\sigma_{bearing}(N)$ @ Numerator.

Coefficient exponential:

$$a = -7.7e - 4$$
, $b = -1.1e - 3$, $c = 7.0e - 4$, $d = -1.2e - 2$

Gain $K_{bearing}(N)$ @ Denominator.

Coefficient polynomial:

$$p1 = -4.7e - 7, p2 = 1.9e - 4$$

$$UMPSA$$

$$N = speed$$

$$\sigma_{bearing}(N) = a * \exp(b * N) + c * \exp(d * N)$$

$$K_{bearing}(N) = p1 * N + p2$$

Transfer function for permanent magnet at varying speed.

Pole $\sigma_{permanent\ magnet}(N)$ @ Numerator.

Coefficient exponential:

$$a = -8.8e - 4$$
, $b = -1.4e - 3$, $c = 7.4e - 4$, $d = -9.2e - 3$

Gain $K_{permanent \ magnet}(N)$ @ Denominator.

Coefficient polynomial:

$$p1 = -4.7e - 7$$
, $p2 = 1.9e - 4$

$$N = speed$$

$$\sigma_{\text{permanent magnet}}(N) = a * \exp(b * N) + c * \exp(d * N)$$

$$K_{permanent \; magnet}(N) = p1 * N + p2$$

Transfer function for casing at varying speed.

Pole $\sigma_{casing}(N)$ @ Numerator.

Coefficient exponential:

$$a = -9.3e - 4$$
, $b = -1.6e - 3$, $c = 7.8e - 4$, $d = -8.3e - 3$

Gain $K_{casing}(N)$ @ Denominator.

Coefficient polynomial:

$$p1 = -4.6e - 7, p2 = 1.9e - 4$$

$$N = speed$$

$$\sigma_{\text{casing}}(N) = a * \exp(b * N) + c * \exp(d * N)$$

$$K_{casing}(N) = p1 * N + p2$$



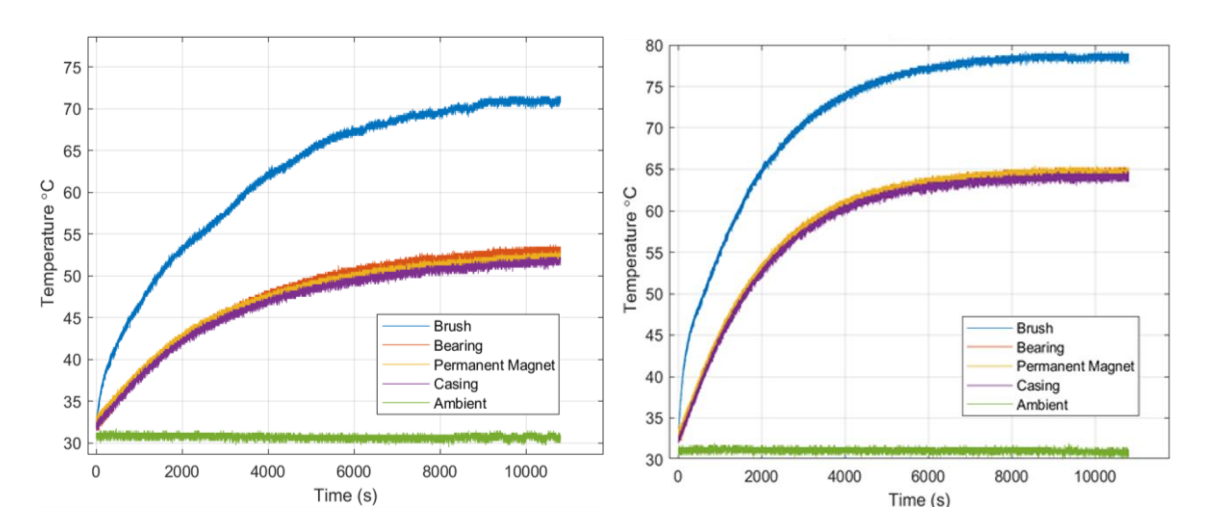
اونيؤرسيتي مليسيا فهغُ السلطان عبدالله UNIVERSITI MALAYSIA PAHANG AL-SULTAN ABDULLAH

Appendix G: Pole Function Code.

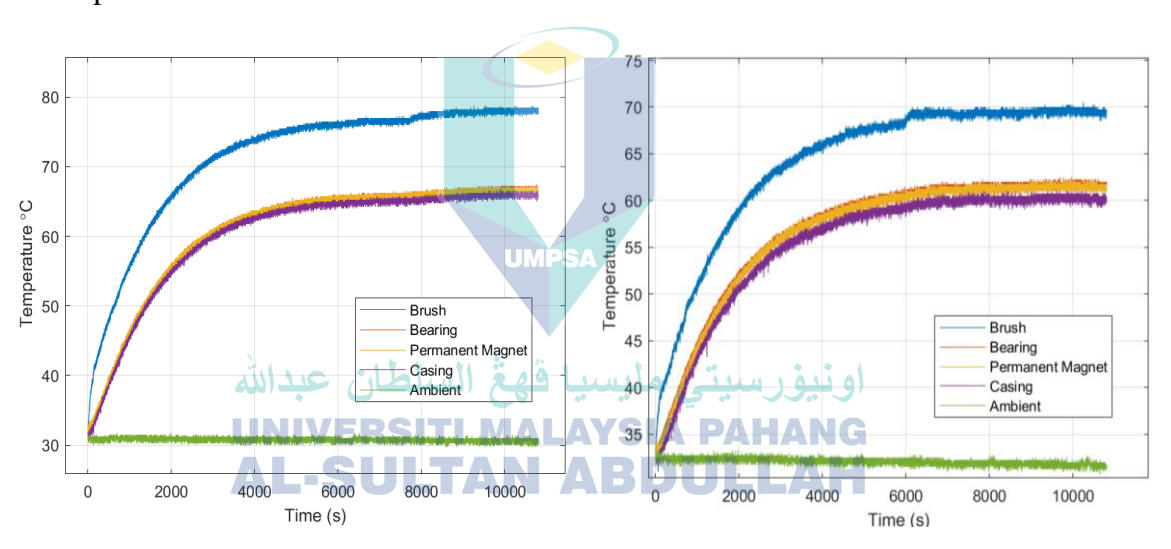
```
function[br num,br den0,br den1,br den2,be num,be den,pm num,pm den,cs num,cs
den]= speed(vals)
% Brush
%Brush real number
%Pole 1 data from exponential 2
br_a1 = 0.0005619;
br_b1 = 0.01276;
br_c1 = -0.001848;
br_d1 = 0.00903;
%Pole 2 data from exponential 2
br a2 = 0.0006881;
br b2 = 0.01372;
br_c2 =-0.002001;
br_d2 = 0.009904;
%Pole 3 data from polynomial 2
br a3 = 1.289e-08;
br b3 =-4.812e-06;
br c3 = -0.0001109;
%Brush i complex number
%Pole 1 data from polynomial 2 LAR
br_a1i =-1.969e-07;
br b1i = 4.718e-05;
br c1i = 0.0007725;
%Pole 2 data from polynomial 2 LAR
br_a2i = 1.969e-07;
br_b2i = -4.718e - 05;
br_c2i =-0.0007725;
%Gain data from polynomial 2 LAR
br p1 = -2.586e - 13;
br_p2 = 6.931e-11;
اونيور سيتي مليسيا فهع السلطان عدز br_p3 =-1.912e-10;
%Gain function from Polynomial
k = br p1*vals^2 + br p2*vals + br p3; %gain brush poly 2
%Pole function from Exponential and Polynomial for real number
den1 = br_a1*exp(br_b1*vals)+br_c1*exp(br_d1*vals); %curve fitter
den2 = br_a2*exp(br_b2*vals)+br_c2*exp(br_d2*vals); %real number
den3 = br_a3*vals^2+br_b3*vals+br_c3;%real number poly 2
%Pole function from Polynomial 2 for complex number
den1i = br_a1i*vals^2+br_b1i*vals+br_c1i;%complex number poly 2
den2i = br_a2i*vals^2+br_b2i*vals+br_c2i;%complex number poly 2
den3i = 0;
z = 0; %zeros
%Sum of pole between real and complex number
p = [den1+den1i*i,den2+den2i*i,den3+den3i*i]; % combination poles
%Convert gain and poles to transfer function
[num,den] = zp2tf(z,p,k);
%New Gain Output
br_num = num(1,3); %numerator
%New Pole Output
br_den0 = den(1,4); %denominator s^0
br_den1 = den(1,3); %denominator s^1
br_den2 = den(1,2); %denominator s^2
```

```
%% Bearing
%Pole data from exponential function
be_a =-0.0007722;
be_b =-0.001092;
be_c = 0.0006995;
be_d =-0.01156;
%Gain data from polynomial function
be p1 =-4.721e-07;
be_p2 = 0.0001946;
%New Gain Output
be_num = be_p1*vals+be_p2;
%New Pole Output
be_den = be_a*exp(be_b*vals)+be_c*exp(be_d*vals);
%% Permanent Magnet
%Pole data from exponential function
pm_a = -0.0008783;
pm_b = -0.001394;
pm_c = 0.0007423;
pm d = -0.009215;
%Gain data from polynomial function
pm_p1 =-4.685e-07;
pm_p2 = 0.0001932;
%New Gain Output
pm_num = pm_p1*vals+pm_p2;
%New Pole Output
pm_den = pm_a*exp(pm_b*vals)+pm_c*exp(pm_d*vals);
%% Casing
%Pole data from exponential function
cs_a = -0.0009327;
cs_b = -0.001456;
cs_c = 0.0007804;
cs_d = -0.008379;
%Gain data from polynomial function
cs_p1 =-4.598e-07;
cs_p2 = 0.0001896;
%New Gain Output NIVERSITI MALAYSIA PAHANG
cs_num = cs_p1*vals+cs_p2; TAN ABDULLAH
%New Pole Output
cs_den = cs_a*exp(cs_b*vals)+cs_c*exp(cs_d*vals);
```

Appendix H: Temperature Response Data.



Temperature response data gathered at left: 20% and right: 40% of the nominal speed of 2650rpm.



Temperature response data gathered at left: 80% and right: 100% of the nominal speed of 2650rpm.

Appendix I: Identified Transfer Function.

Identified transfer function for bearing.

No. of Poles	Speed (%)	Transfer Function	MSE error
1 0168	(70)	1.404	C1 1 U1
	20	1.494e-4	0.1271
		s + 3.315e-4	*****
	40	<u>1.693<i>e</i>-4</u>	0.1185
		s + 5.086e-4	
1	60	1.279 <i>e</i> – 4	0.2252
-		s + 4.985e-4	
	80 100	1.028 <i>e</i> -4	0.1599 0.1198
		s + 5.841e-4	
		<u>6.227<i>e</i>-5</u>	
	100	s + 5.284e - 4	0.1170
	20	8.146 <i>e</i> -7	4.861
		$s^2 + 2.468e - 2s + 1.324e - 7$	
	40	2.077 <i>e</i> -5	0.1275
	10	$s^2 + 0.1253 s + 6.245e - 5$	0.1273
2	60	6.931e-6	0.2248
2	00	$s^2 + 5.462e - 2s + 2.701e - 5$	0.2240
	80	2.502 <i>e</i> – 6	0.1537
	80	$s^2 + 2.476e - 2s + 1.423e - 5$	
	100	3.006 <i>e</i> -6	0.1195
	100	$s^2 + 4.873e - 2s + 2.551e - 5$	0.1193
	20	UMP\$4,584e-11	19.06
	20	$s^3 + 2.856e - 3 s^2 + 2.585e - 6 s + 4.787e - 18$	
	40	3.575 <i>e</i> -10	0.1140
	40	$s^3 + 2.435e - 2 s^2 + 1.417e - 5 s + 1.086e - 9$	0.1148
2	60	4.878e-9	0.2024
3		$s^3 + 9.851e - 2 s^2 + 7.856e - 5 s + 1.945e - 8$	
	0.0	2.458e-10	0.3212
	80	$s^3 + 2.295e - 2 s^2 + 1.439e - 5 s + 1.378e - 9$	
	400	3.267 <i>e</i> – 5	0.1101
	100	$\overline{s^3 + 14.75 s^2 + 0.5317 s + 2.773e - 4}$	0.1194
		1.039 <i>e</i> -12	9.851
	20	$s^4 + 1.212e - 2 s^3 + 4.786e - 5 s^2 + 1.076e - 7 s + 1.259e - 20$	
	40	1.144e-9	
		$s^4 + 6.602e - 2 s^3 + 6.406e - 4 s^2 + 7.035e - 6 s + 3.438e - 9$	0.1165
	60	2.975 <i>e</i> -11	0.2062
4		$s^4 + 4.506e - 2 s^3 + 6.952e - 4 s^2 + 5.139e - 7 s + 1.191e - 10$	
	80		0.1488
		3.338e-11	
		$s^4 + 1.291e - 2 s^3 + 1.01e - 4 s^2 + 3.738e - 7 s + 1.9e - 10$	
	100	5.133e-13	0.1548
		$s^4 + 1.203e - 2 s^3 + 4.973e - 5 s^2 + 3.445e - 8 s + 4.182e - 12$	

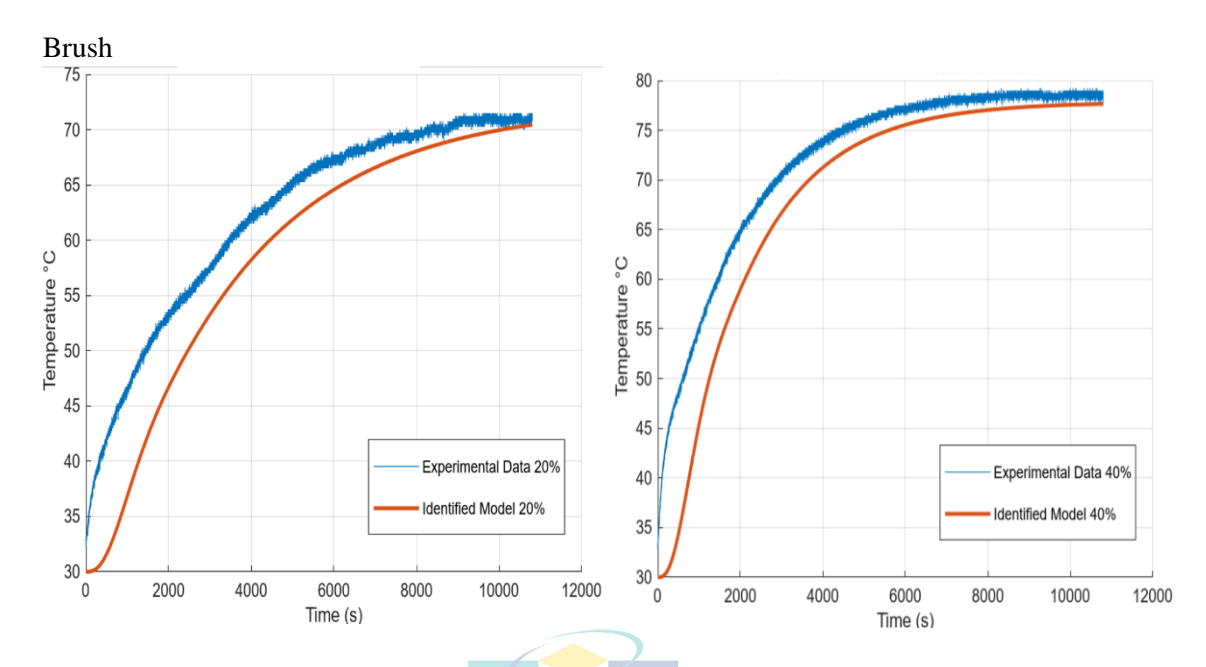
Identified transfer function for permanent magnet.

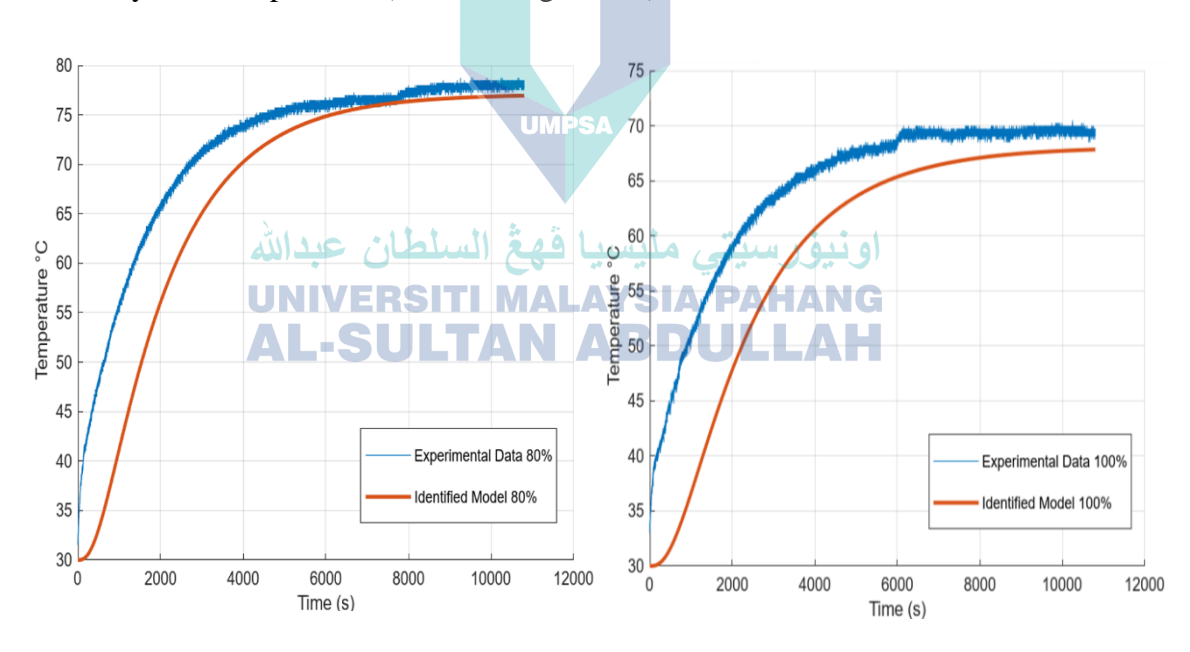
No. of	Speed (%)	Transfer Function	MSE
Poles			error
	20	1.471 <i>e</i> -4	0.1196
	20	s + 3.402e - 4	0.1186
	40	1.695 <i>e</i> -4	0.1145
		s + 5.08e - 4	
1	60	<u>1.274<i>e</i>-4</u>	0.2324
-		s + 4.937e - 4	
	80 100	$\frac{1.024e-4}{2.000000000000000000000000000000000000$	0.1658 0.1214
		s + 5.818e-4	
		6.118e-5	
		s + 5.218e-4 4.46e-7	4.228
	20	$\frac{1.40e^{-7}}{s^2 + 1.513e - 2s + 1.631e - 11}$	
		3.468e-6	
	40	$\frac{1}{s^2 + 4.041e - 2s + 9.051e - 6}$	5.139
2		1.922 <i>e</i> -5	0.2493
2	60	$\overline{s^2 + 0.1555 s + 7.425e - 5}$	
	80	3.97 <i>e</i> -6	0.1564
	80	$s^2 + \frac{3.908e}{2} = 2 s + 2.257e - 5$	
	100	1.763 <i>e</i> -6	0.1158
	100	$s^2 + 2.914e - 2s + 1.504e - 5$	
	20	1.003 <i>e</i> -8	0.118
		$s^3 + 1.237e - 2 s^2 + 7.16e - 5 s + 2.322e - 8$	0.110
	40	2.84e-10	0.1077
		$s^3 + 1.61e - 2s^2 + 9.65e - 6s + 8.572e - 10$	
3	60	$\frac{1.952e - 10}{2.3 + 1.506 + 2.2 + 0.202 + 0.471 + 10}$	0.1724
		$s^3 + 1.586e - 2s^2 + 8.392e - 6s + 8.171e - 10$ 1.392e - 10	
	80	$\frac{1.372e^{-10}}{s^3 + 1.828e - 2 s^2 + 1.144e - 5 s + 7.565e - 10}$	0.2309
		UNIVERSITI MAL 1.953e-10 PAHANG	
	100	$s^3 + 3.506e - 2 s^2 + 1.943e - 5 s + 1.651e - 9$	0.2523
	20	2.484e-11	0.1178
	20	$s^4 + 2.381e - 2 s^3 + 5.946e - 4 s^2 + 3.772e - 7 s + 5.678e - 11$	
	40	5.411e-10	0.105
	40	$s^4 + 2.497e - 2 s^3 + 4.939e - 4 s^2 + 3.376e - 6 s + 1.625e - 9$	0.105
4	60	9.055 <i>e</i> -10	0.2283
4		$s^4 + 7.098e - 2 s^3 + 8.196e - 4 s^2 + 7.43e - 6 s + 3.513e - 9$	
	80	1.997e-11	0.1387
		$s^4 + 1.237e - 2 s^3 + 8.102e - 5 s^2 + 2.333e - 7 s + 1.137e - 10$	- · ·
	100	4.028e-13	0.1506
		$s^4 + 1.175e - 2 s^3 + 4.638e - 5 s^2 + 3.066e - 8 s + 3.28e - 12$	

Identified transfer function for casing.

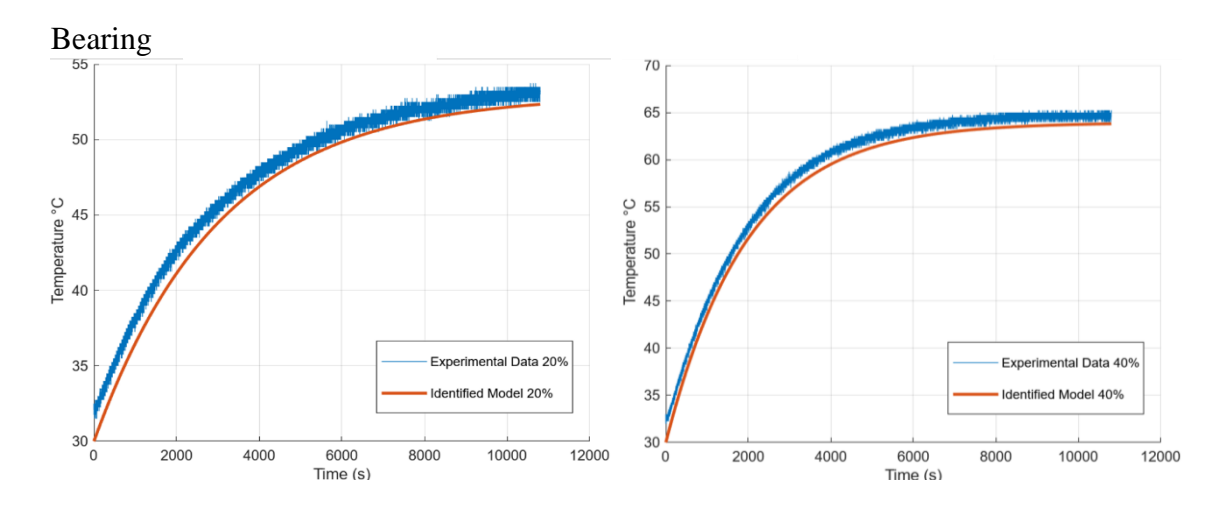
No. of	Speed	Transfer Function	MSE
Poles	(%)		error
	20	1.437 <i>e</i> -4	0.126
	20	s + 3.416e - 4	0.120
	40	<u>1.667<i>e</i>-4</u>	0.1212
		s + 5.1e-4	
1	60	1.256e-4	0.2455
		s + 4.949e - 4	
	80	$\frac{1.012e-4}{1.012e-4}$	0.1644
		s + 5.872e - 4	
	100	5.921 <i>e</i> -5	0.1395
		s + 5.269e - 4	
	20	6.84e-7	4.483
		$s^2 + 2.38e - 2s + 6.748e - 9$ 1.525e - 5	
	40		1.093
		$s^2 + 0.119 s + 4.477e - 5$ 3.067e - 6	
2	60	$\frac{3.007e-0}{s^2 + 2.479e-2 s + 1.209e-5}$	0.2414
		$3^{2} + 2.479e - 28 + 1.209e - 3$ $-1.212e - 6$	
	80	$s^2 + \frac{1.236e - 2s + 7.043e - 6}{}$	0.1459
	100	6.07e-7	0.1332
		$\frac{1}{s^2 + 1.067e - 2s + 5.407e - 6}$	
		2.263 <i>e</i> -9	
	20	$s^3 + 2.896e - 3 s^2 + 1.663e - 5 s + 5.38e - 9$	0.1243
		2.235 <i>e</i> -10	
	40	$\overline{s^3 + 1.828e - 2 s^2 + 1.045e - 5 s + 6.906e - 10}$	0.1153
		4.839 <i>e</i> -11	0.1017
3	60	$\overline{s^3 + 9.107e - 3 s^2 + 4.464e - 6 s + 2.181e - 10}$	0.1915
	0.0	2.014e-10	0.5461
	80	$s^3 + 2.369e - 2 s^2 + 1.436e - 5 s + 1.102e - 9$	0.5461
	100	UNIVERSITI MAL/7.815e-9 PAHANG	0.1225
	100	$s^3 + 1.556e - 2 s^2 + 1.389e - 4 s + 6.959e - 8$	0.1325
	20	-9.121 <i>e</i> -15	11.99
	20	$s^4 + 3.74e - 3 s^3 + 1.135e - 5 s^2 + 1.498e - 8 s + 3.103e - 23$	
	40	1.267 <i>e</i> -9	0.115
	40	$s^4 + 6.488e - 2 s^3 + 7.414e - 4 s^2 + 7.857e - 6 s + 3.882e - 9$	0.115
4	60	1.697 <i>e</i> -11	0.2254
		$s^4 + 8.828e - 3 s^3 + 5.6e - 5 s^2 + 1.565e - 7 s + 6.709e - 11$	0.2234
	80	3.936e-11	0.1408
		$s^4 + 1.361e - 2 s^3 + 1.237e - 4 s^2 + 4.472e - 7 s + 2.29e - 10$	0.1400
	100	6.841 <i>e</i> -13	0.1313
	100	$s^4 + 1.781e - 2 s^3 + 8.296e - 5 s^2 + 5.195e - 8 s + 5.993e - 12$	0.1313

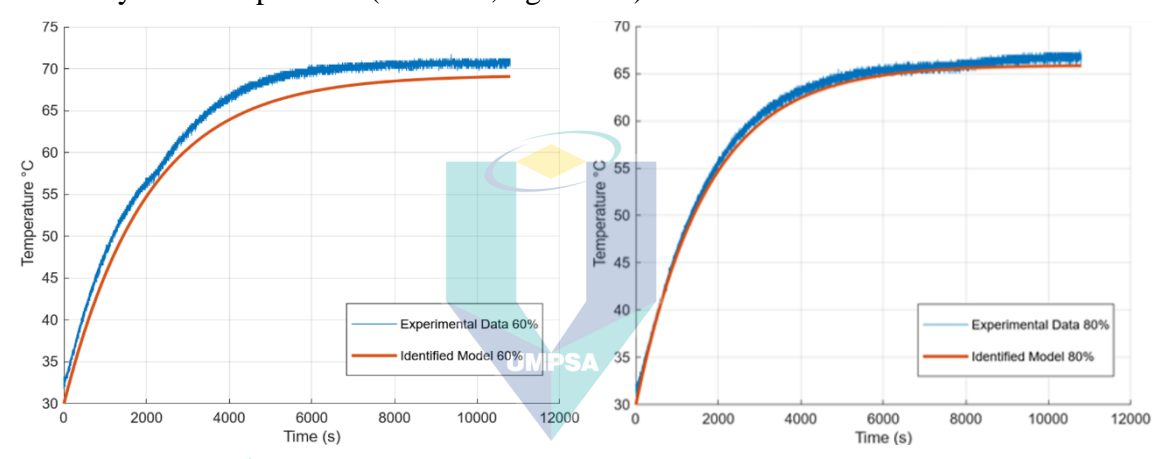
Appendix J: Validation Identified Transfer Function As Model.



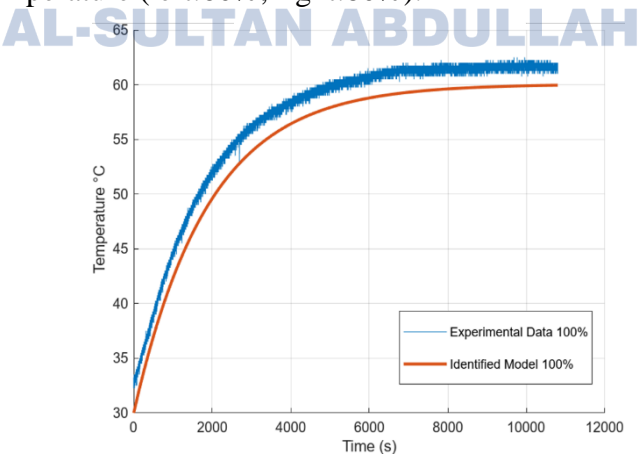


Comparison between identified transfer function vs. experimental temperature response at steady state temperature (left:80%, right:100%).

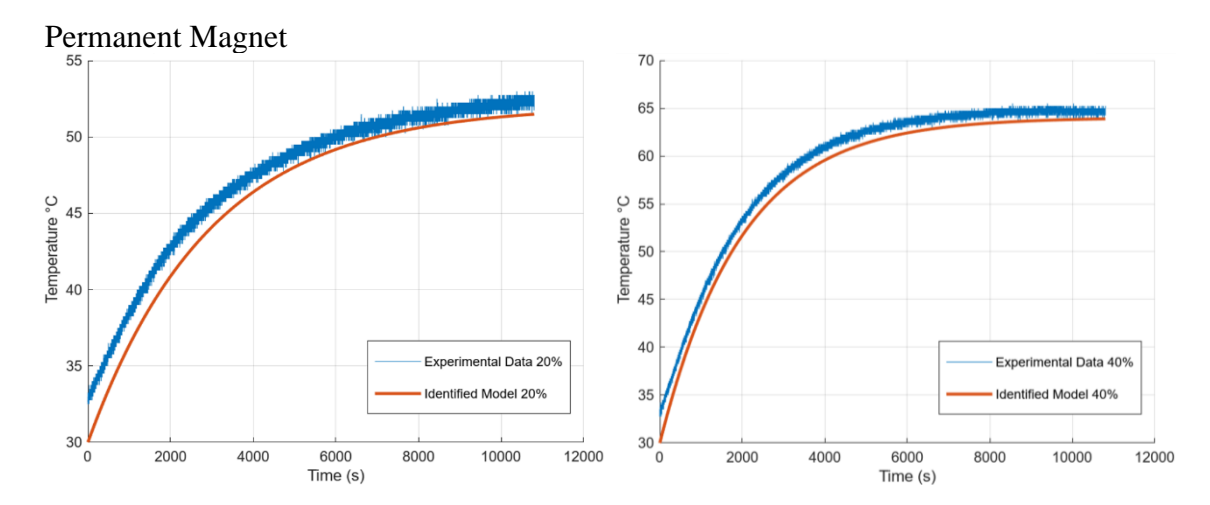


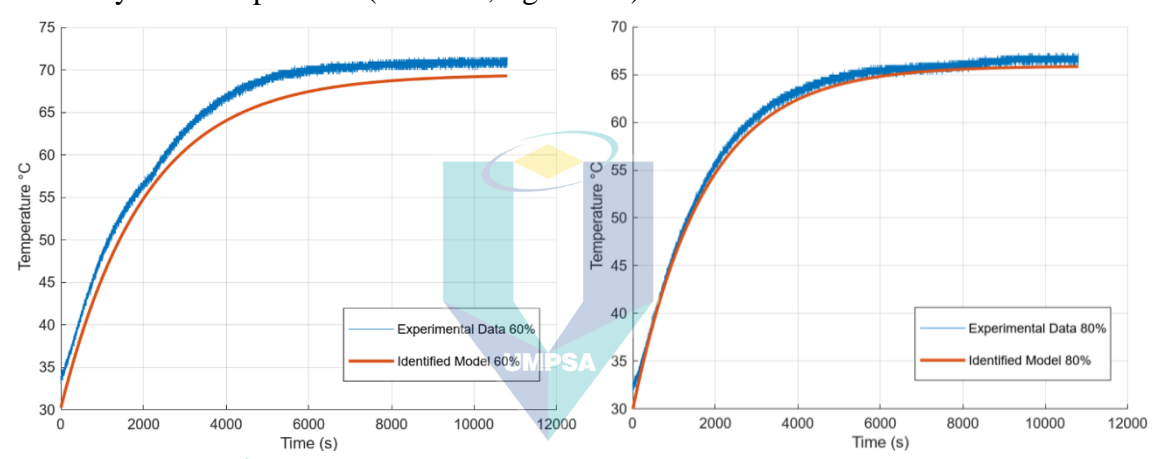


Comparison between identified transfer function vs. experimental temperature response at steady state temperature (left:60%, right:80%).

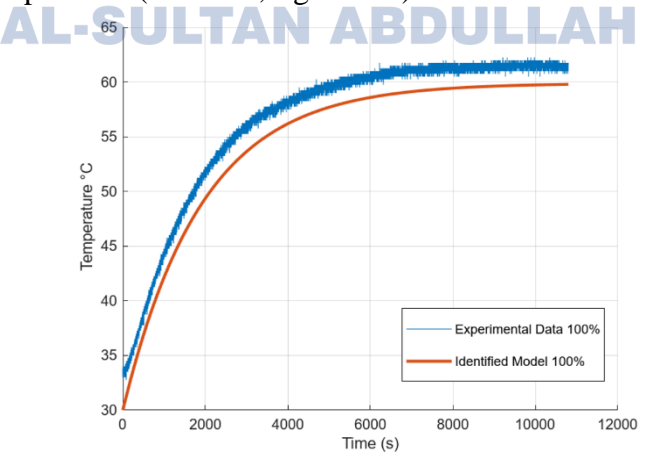


Comparison between identified transfer function vs. experimental temperature response at steady state temperature (100%).

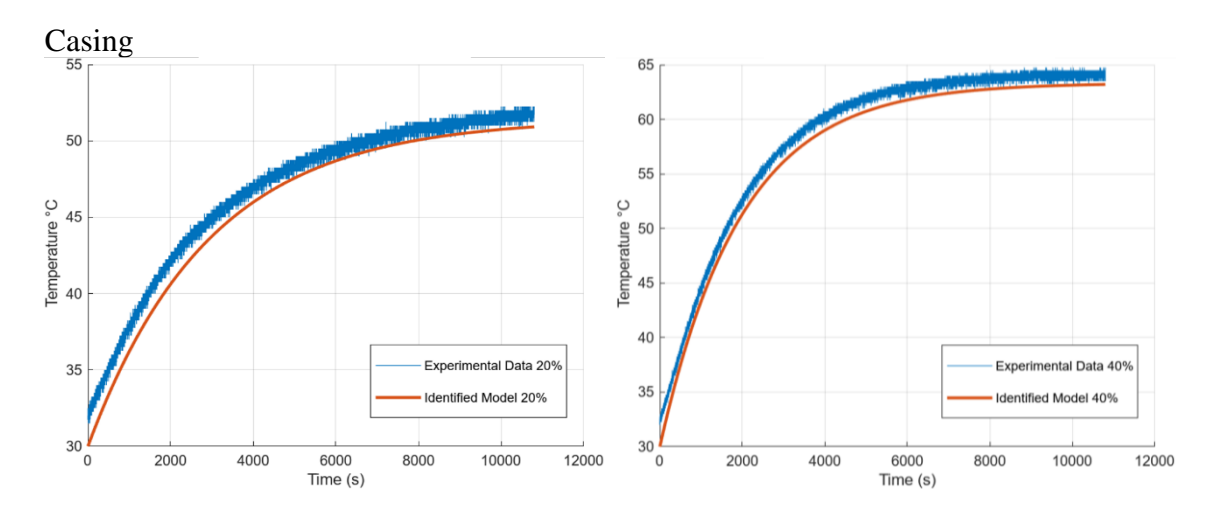


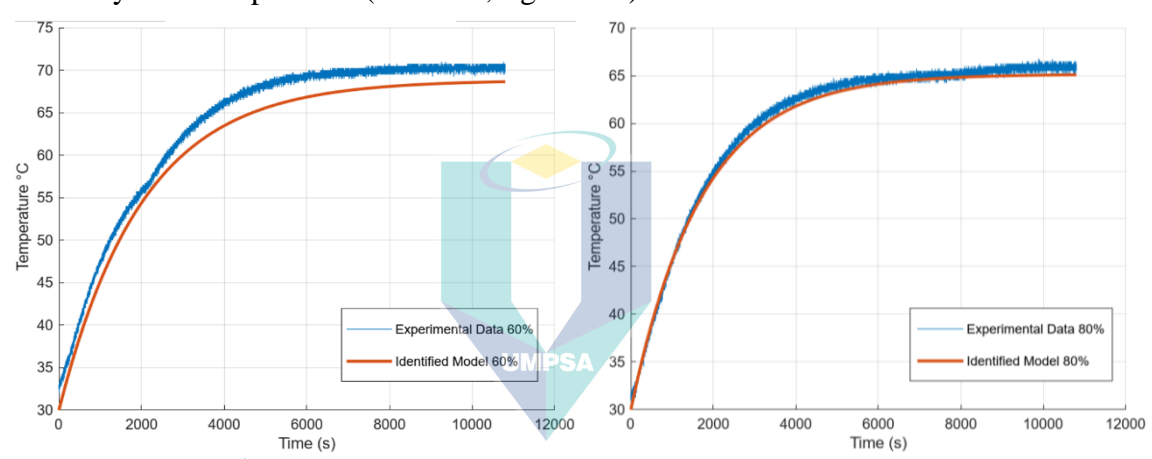


Comparison between identified transfer function vs. experimental temperature response at steady state temperature (left:60%, right:80%).

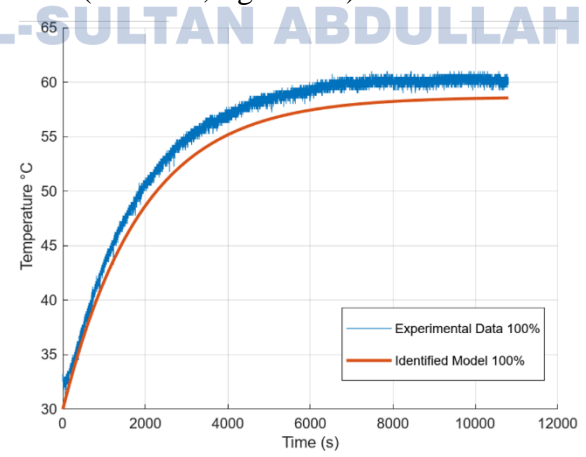


Comparison between identified transfer function vs. experimental temperature response at steady state temperature (100%).



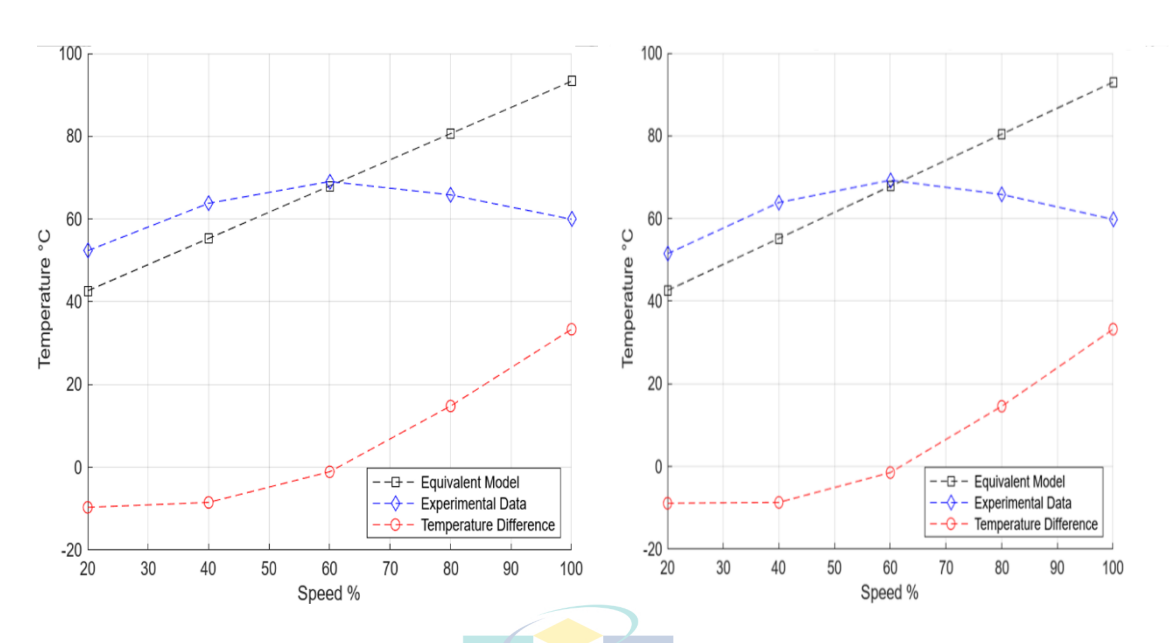


Comparison between identified transfer function vs. experimental temperature response at steady state temperature (left:60%, right:80%).

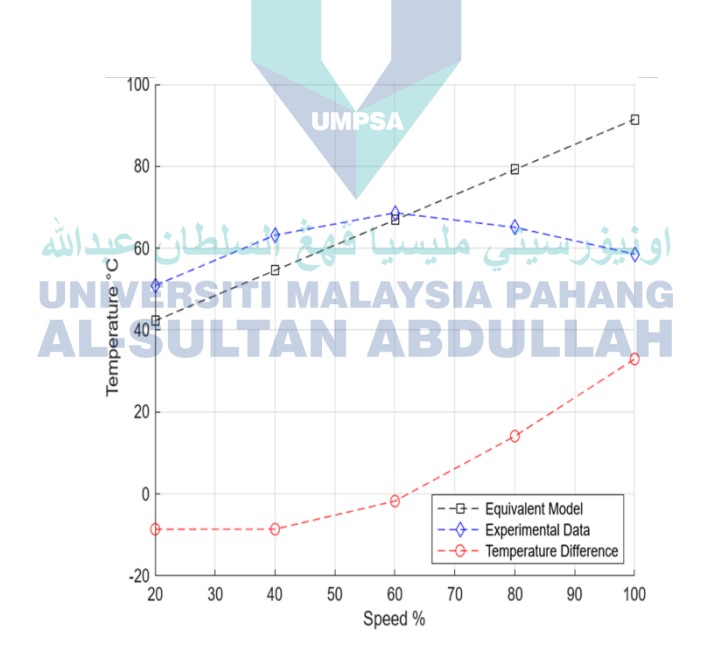


Comparison between identified transfer function vs. experimental temperature response at steady state temperature (100%).

Appendix K: Result of Steady State Temperature Response for Averaged-pole Transfer Function Model.

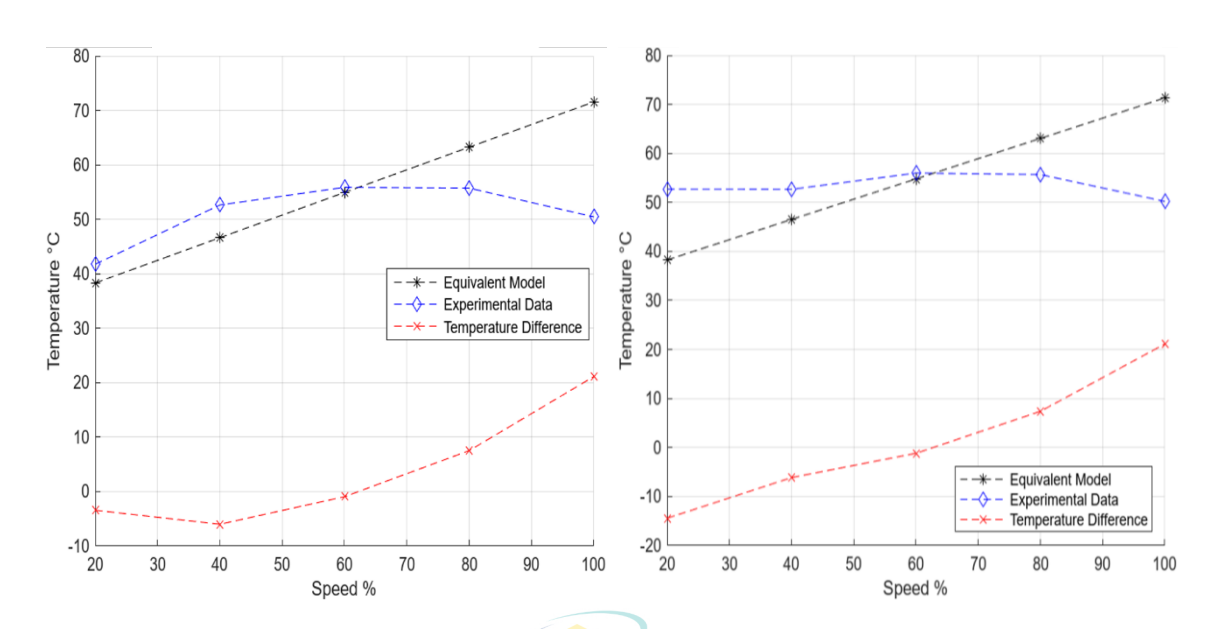


Comparison between averaged-pole transfer function vs. experimental temperature response at steady state temperature (left:bearing, right:permanent magnet).



Comparison between averaged-pole transfer function vs. experimental temperature response at steady state temperature (casing).

Appendix L: Result of Transient State Temperature Response for Averaged-pole Transfer Function Model.

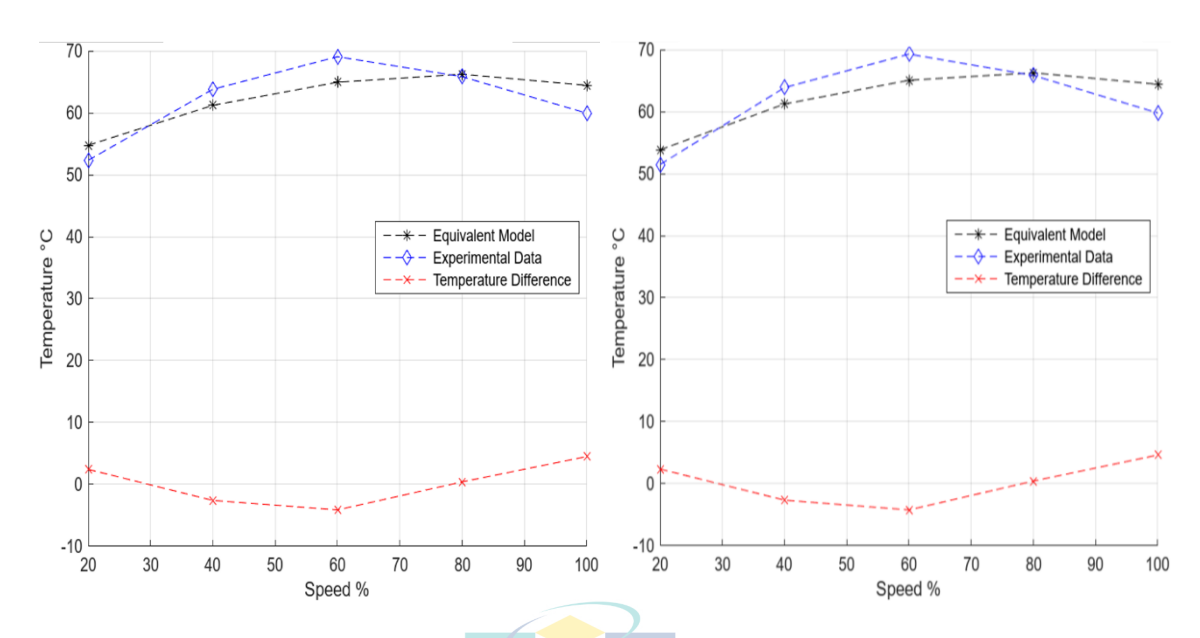


Comparison between averaged-pole transfer function vs. experimental temperature response at transient state temperature (left:bearing, right:permanent magnet).

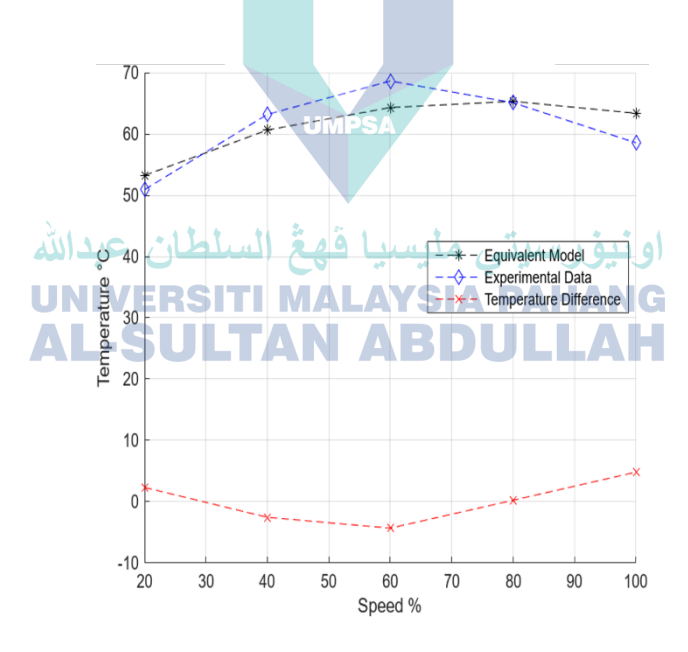


Comparison between averaged-pole transfer function vs. experimental temperature response at transient state temperature (casing).

Appendix M: Result of Steady State Temperature Response for Variable-pole Transfer Function.

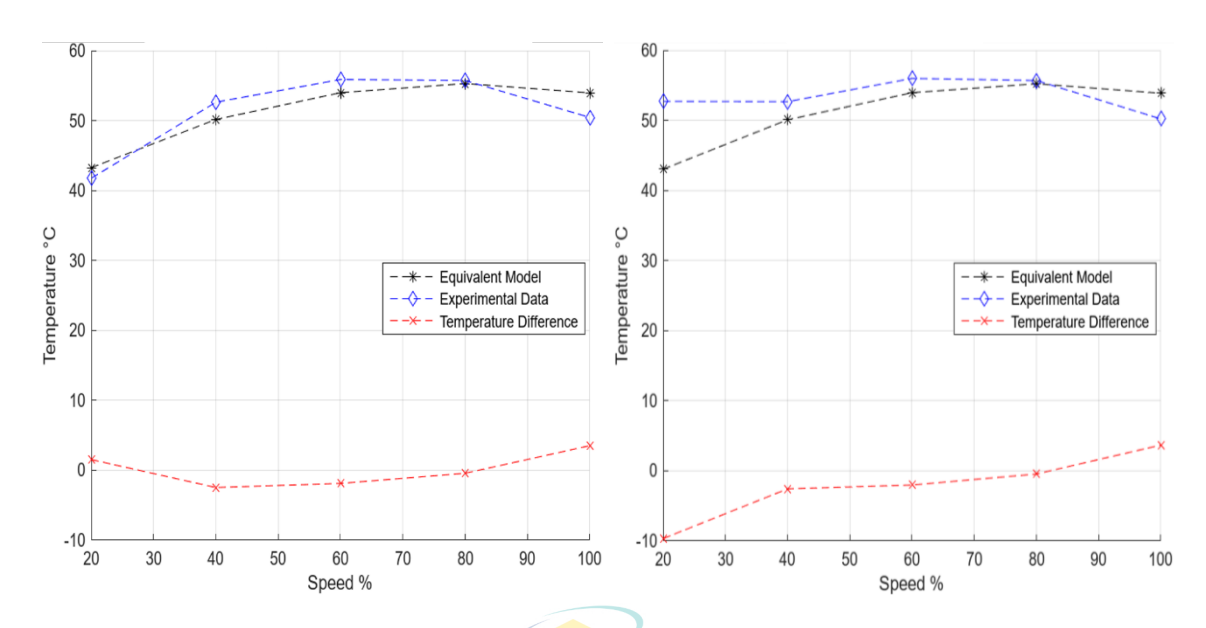


Comparison between variable-pole transfer function vs. experimental temperature response at steady state temperature (left:bearing, right:permanent magnet).

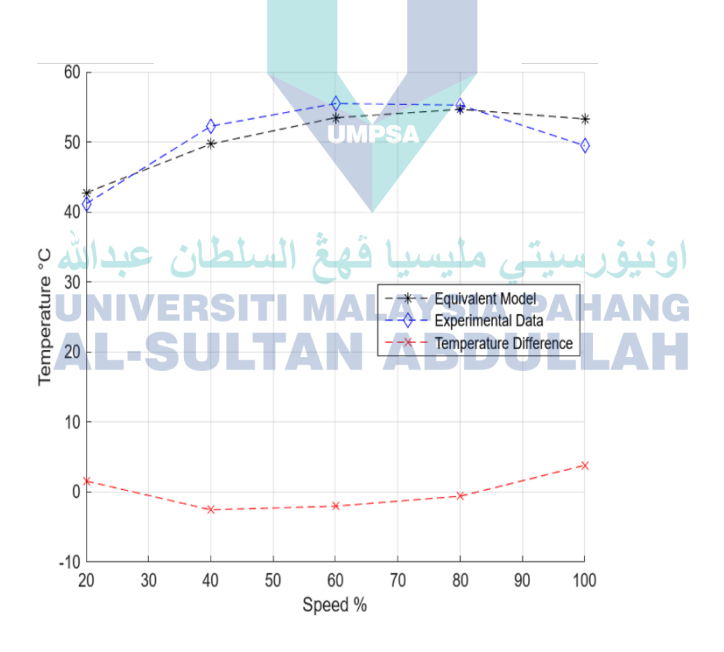


Comparison between variable-pole transfer function vs. experimental temperature response at steady state temperature (casing).

Appendix N: Result of Transient State Temperature Response for Variable-pole Transfer Function.

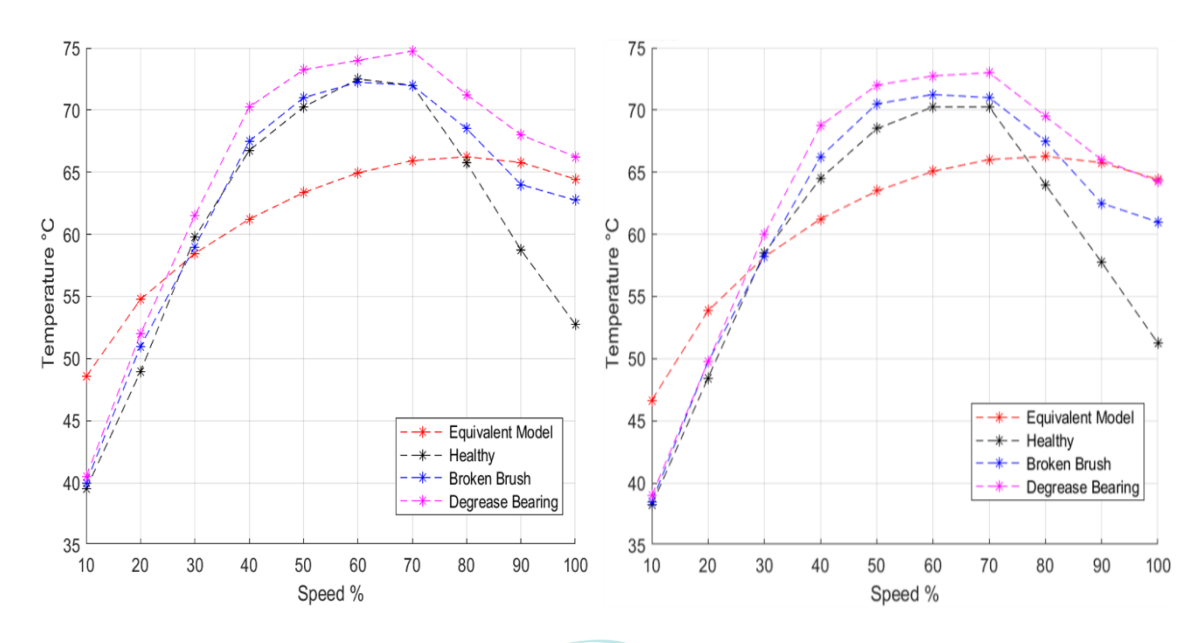


Comparison between variable-pole transfer function vs. experimental temperature response at transient state temperature (left:bearing, right:permanent magnet).

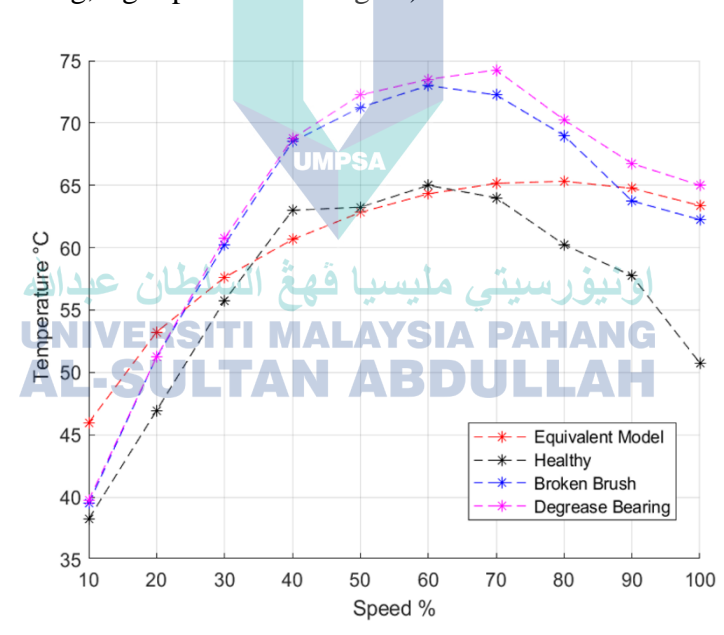


Comparison between variable-pole transfer function vs. experimental temperature response at transient state temperature (casing).

Appendix O: Result of Generalized Transfer Function in Fault Detections



Comparison between variable-pole transfer function model vs. healthy and faulty DC machines(left:bearing, right:permanent magnet).



Comparison between variable-pole transfer function model vs. healthy and faulty DC machines(casing).